運輸省港湾技術研究所

港湾技術研究所報告

REPORT OF THE PORT AND HARBOUR RESEARCH INSTITUTE

MINISTRY OF TRANSPORT

VOL. 24 NO. 2 JUNE 1985

NAGASE, YOKOSUKA, JAPAN

港湾技術研究所報告 (REPORT OF P.H.R.I.)

第24巻　第２号 (Vol. 24, No. 2) 1985年６月 (June 1985)

目　次 (CONTENTS)

REPORT OF THE PORT AND
HARBOUR RESEARCH INSTITUTE
Vol. 24, No. 2 (June 1985)

1. An Effective Stress Analysis of Liquefaction at Ishinomaki Port during the 1978 Miyagi-Ken-Oki Earthquake

Susumu IAI*
Hajime TSUCHIDA**
W. D. Liam FINN***

Synopsis

An effective stress model is a promising technique in meeting the increasing demands for higher accuracy in assessing liquefaction potential in detail. In order to study its applicability, the effective stress model developed by one of the authors is compared with field performances during a large earthquake in the present report. It is essential for carrying out the comparison that full information be compiled on the liquefaction data, the ground conditions, and the input ground motions. Ishinomaki Port during the 1978 Miyagi-ken-Oki Earthquake provided a good opportunity for obtaining such information.

In addition to such information, sand specimen were taken from Ishinomaki Port and tested in a laboratory using a simple shear apparatus. The effective stress model applied for sand specimen was studied in detail for concerning influence of vertical confining pressure on liquefaction strength.

Most of the parameters of the effective stress model were thus estimated for the simulation. Simulation of ground performances by this model gave results similar to the observed ground performances at the liquefied and the non-liquefied areas.

---

* Senior Research Engineer, Structures Division
** Director, Structures Division
*** Professor, Soil Dynamics Group, Faculty of Graduate Studies,
The University of British Columbia, CANADA

港湾技術研究所報告
第24巻　第2号（1985. 6）

1. 1978年宮城県沖地震の石巻港における液状化の有効応力解析

井合　進*・土田　肇**・W.D.L. フィン***

要　旨

有効応力モデルは，液状化予測において精度の高い詳細な予測を行うための手法として，原理的には有望である。その適用性を検討するため，著者らのうちの一人の開発した有効応力モデルと大地震時の液状化事例との対比を行った。このような比較を行うためには，液状化のこん跡，地盤条件，地盤への入力地震動に関する詳細な情報を収集整理することが必要である。1978年宮城県沖地震における石巻港は，このような情報を十分に提供するものであった。

これらの情報に加えて，石巻港から砂試料を採取し単純せん断試験を行った。砂試料に適用した場合の有効応力モデルについては，液状化強度と鉛直拘束圧力との関係について詳しく検討を行った。

このようにして，有効応力モデルのパラメタを推定しシミュレーションを行った。その結果，シミュレーション結果と実際の地盤の挙動とには，矛盾がなかった。

---

* 構造部　主任研究官（地震動解析担当）
** 構造部長
*** カナダ国　ブリティッシュ・コロンビア大学教授

Contents

1. Introduction

Since the Niigata Earthquake of 1964, many studies of liquefaction case histories have been carried out which have given geotechnical engineers the bases for estimating liquefaction potential. Several criteria for judging liquefaction potential have been proposed on the basis of these case studies as well as experimental studies in laboratories. The criteria define the field conditions which may lead to liquefaction. According to the case records, the extent of the damage to structures caused by liquefaction varies very widely as was pointed out by Tsuchida1). Therefore, more sophisticated approaches to liquefaction are necessary. There are also increasing demands for higher reliability in estimating liquefaction potential.

A promising technique is the effective stress model by Finn et al.2), which incorporates non-linear hysteretic dynamic response of the ground and generation of pore water pressures associated with this response. The model takes into account softening of soil and decrease of soil strength due to the reduction in vertical effective stress caused by increase in pore water pressure. This is the reason why the model is called an effective stress model. This model has the potential to simulate detailed features of liquefaction phenomena, and it provides a good approach to the task of estimating the degree of liquefaction, its duration, and its spatial distribution. Such a model is considered to be a basic tool in meeting the increasing demands for a new approach to liquefaction problems. However, few comparisons of the model with field performance during large earthquakes have been attempted so far, partly because input base rock motions were not recorded for most of the cases.

During the 1978 Miyagi-Ken-Oki Earthquake, some areas of Ishinomaki Port liquefied. Bore hole data were obtained for the liquefied areas and some of the non-liquefied areas. Accelerations were also measured on a rock outcrop nearby. These data provided an opportunity to compare the model with the field performance of the ground. The comparison was done for not only liquefied areas but also non-liquefied areas.

Part of the study was presented at the Sixth Japan Earthquake Engineering Symposium in 19823). A description of the entire study is presented in this report.

2. Earthquake and Ground Motions

The 1978 Miyaki-Ken-Oki Earthquake took place at 17:14 on June 12, 1978. Its magnitude was 7.4. The location of epicentral region is shown at the upper left corner in Fig. 1. Epicenter of the earthquake is shown by a x-mark. The depth of the hypocenter was 40 km. An arrow in the fault plane shows the direction of slip. The slip within the fault plane was estimated to be 1.7 meters.

Around this region, there were two accelerographs installed on rock outcrops. One was at Ofunato City which is shown at the upper left corner in Fig. 1. The epicentral distance of this accelerograph site is 103 km. The maximum horizontal component acceleration was 170 Gals in E41S direction4). The other accelerograph was located in Ishinomaki City. The instrument site is shown in Fig. 1. The epicentral distance was 80 km, but the distance from the instrument site to the edge of the epicentral region was 25 km. The maximum horizontal component

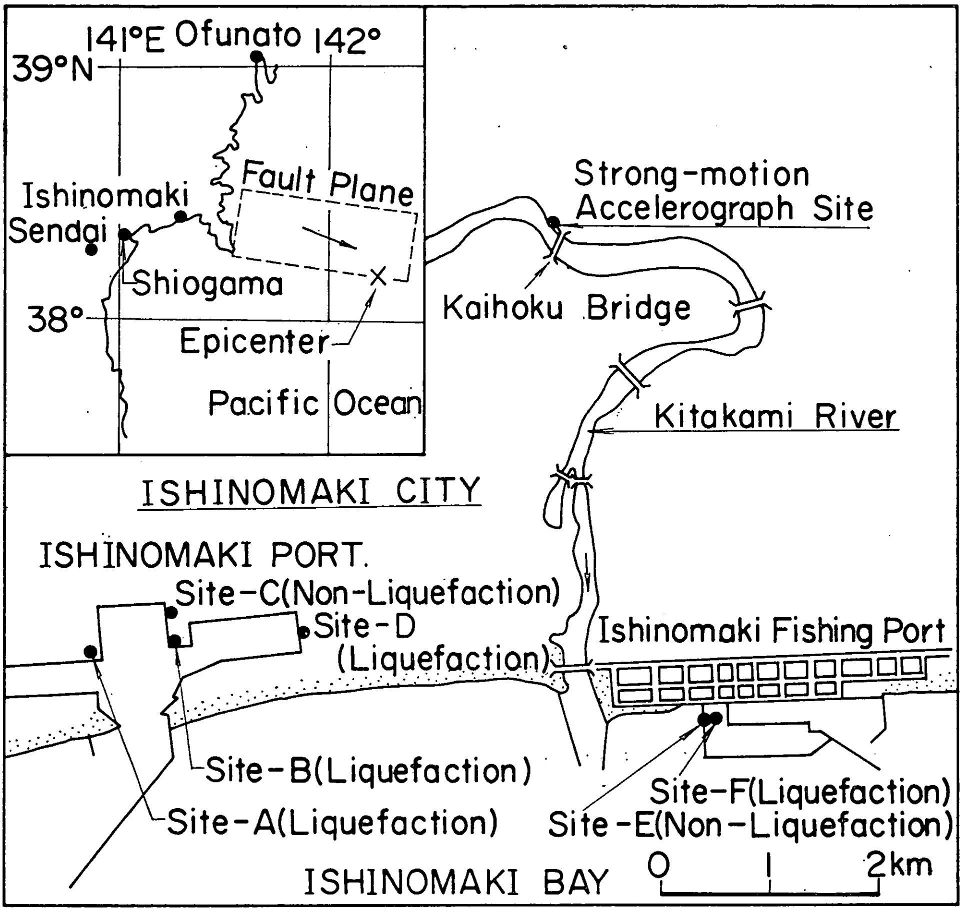

Fig. 1 Locations of the Earthquake and the Sites under Study

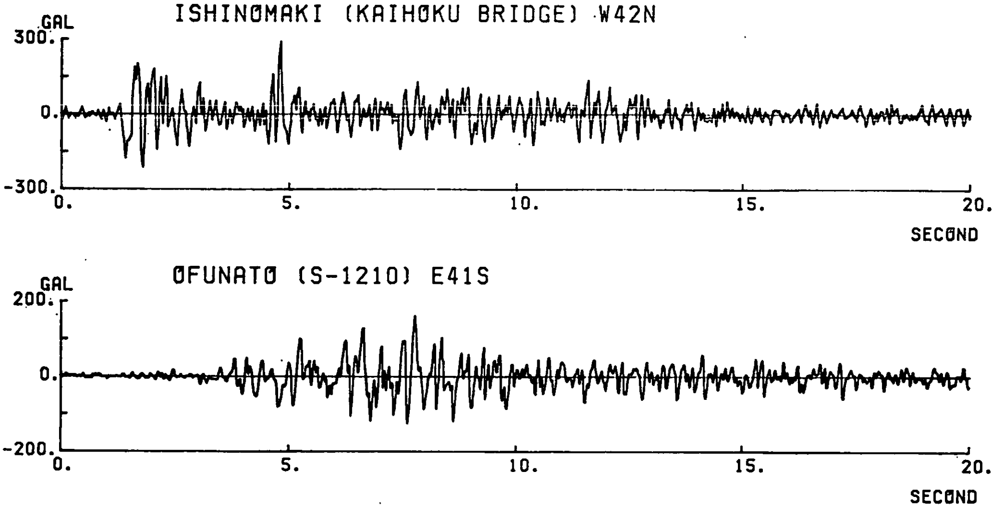

Fig. 2 Time Histories of Ground Acceleration on Rock Outcrop at Ofunato and Ishinomaki

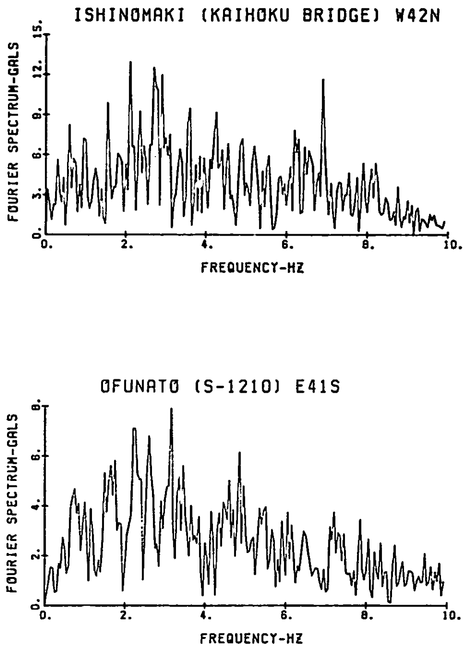

Fig. 3 Fourier Spectra of Rock Outcrop Accelerations at Ofunato and Ishinomaki

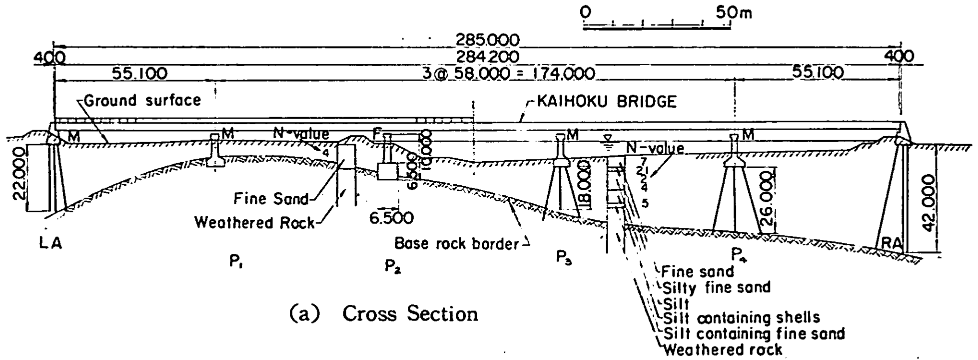

(a) Cross Section

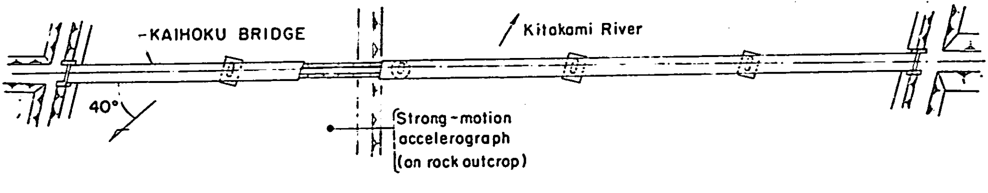

(b) Plan

Fig. 4 Site Conditions of the Strong-Motion Accelerograph, After IWASAKI et al[6].

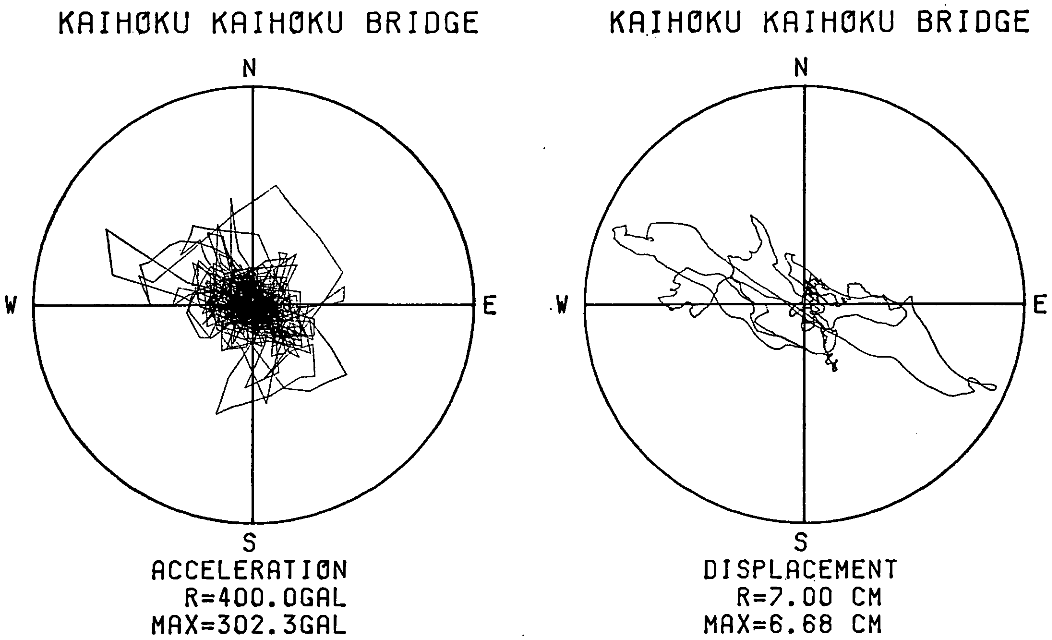

Fig. 5 Loci of Rock Outcrop Motion at Ishinomaki

acceleration was 293 Gals in W42N direction[5]. Both accelerographs are of the SMAC-B2 type. Time histories of both records are shown in Fig. 2. Fourier spectra for these time histories are shown in Fig. 3.

The strong-motion earthquake records at Ofunato and Ishinomaki have slightly different frequency characteristics. Simulated ground responses depend on the acceleration record which is used as the input motion. In this study, the record at Ishinomaki was used as the input motion because it was recorded in the vicinity of the sites under the study. The distance between the accelerograph site and the sites under study is within 5 km.

Site conditions of the strong-motion accelerograph at Ishinomaki are shown in Fig. 4. These conditions were presented in reference[6] which clearly shows that the strong-motion accelerograph is installed on a rock outcrop. Figure 4 also shows that the accelerograph is installed on the top of hill like formation of the base rock.

Figure 5 shows the loci of horizontal ground motions recorded by the strong-motion accelerograph at Ishinomaki. The locus of acceleration does not show any particular direction in which the ground motion is predominant, but the locus of displacement clearly shows that the displacement is predominant in WWN to EES direction. This predominant direction is harmonious with the fault slip direction[7].

3. The Sites for Examinations and the Liquefaction Data

3.1 Outline of the Sites for Examinations

Six sites in Ishinomaki Port were selected for the present study. They are

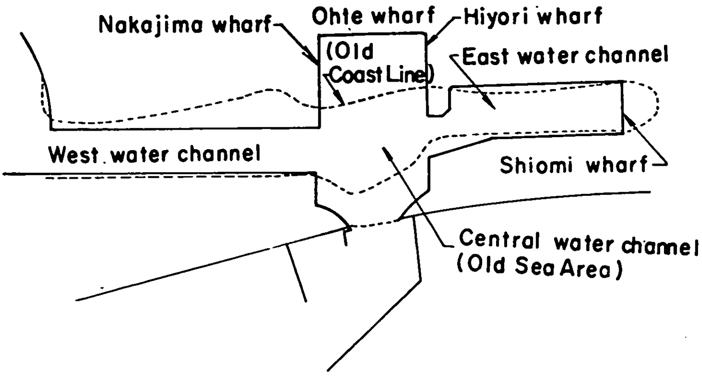

Fig. 6 Comparison of Old Coast Lines (borken line) and Present Face Line of Wharves (solid lines) at Ishinomaki Port

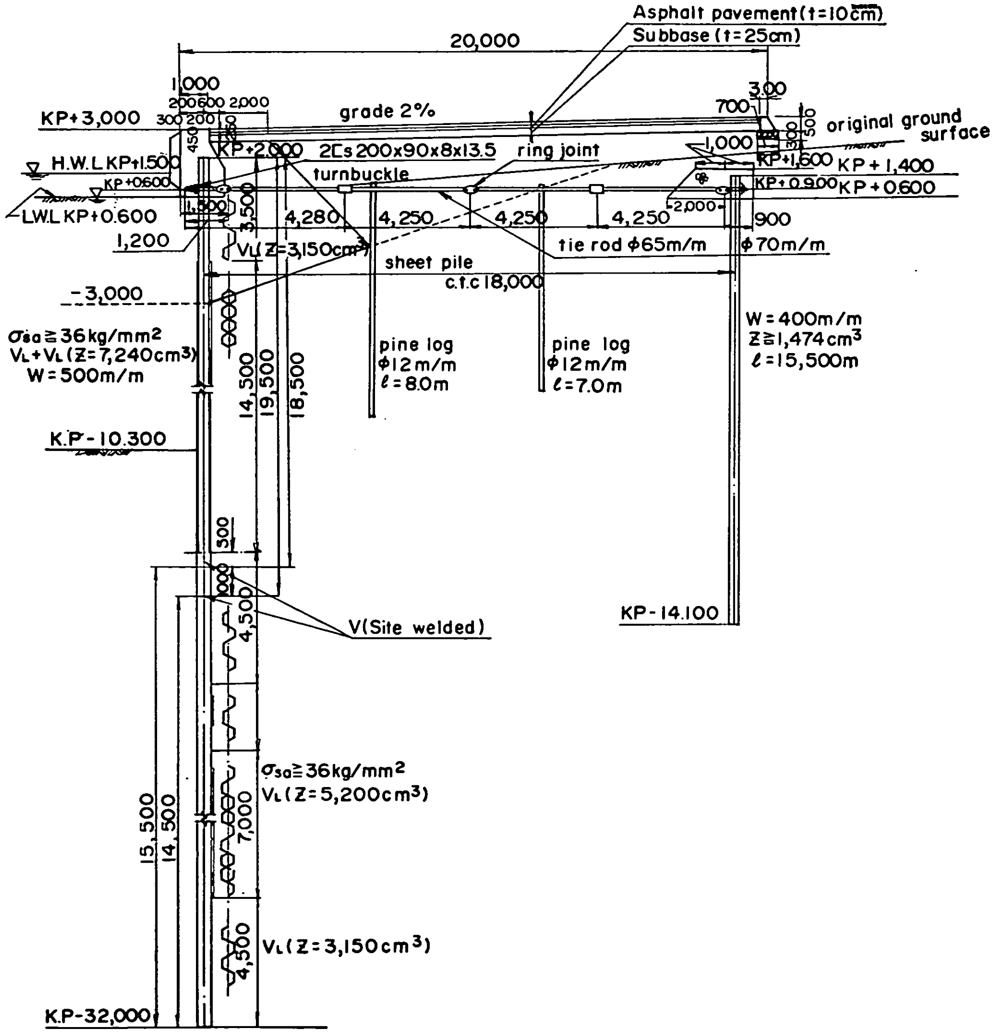

Fig. 7 Cross Section of Nakajima (—10m) Wharf (Unit in meter)

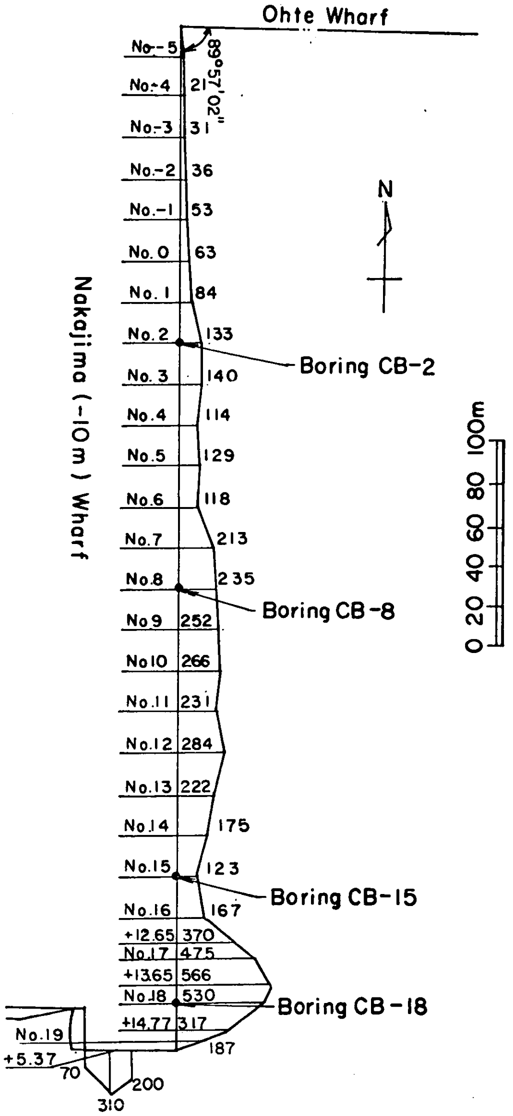

Fig. 8 Residual Horizontal Displacements of Face Line of Nakajima (−10m) Wharf (Unit in mm for the residual displacements)

shown as Sites A to F in Fig. 1. Sites A to F are within a short distance from the accelerograph site and, therefore, the input motions to these sites are considered to have been the same. However the liquefaction at these sites were not the same; Sites A, B, D, and F liquefied but Sites C and E did not.

All the sites have a layer of artificially filled sand with a few meter thickness at top of the original ground. The exact thickness of the filled sand was not recorded. The fill material was dredged from the sea bottom during construction of navigation channels in the port.

Figure 6 shows old coastlines and present face lines of wharves at Ishinomaki

Measured on May.15,16,1978

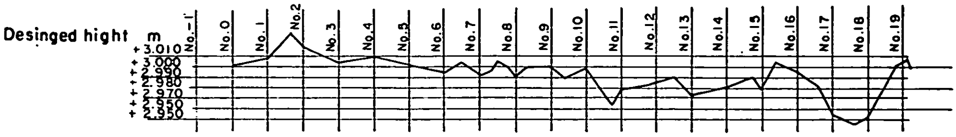

(a) At the Face Line

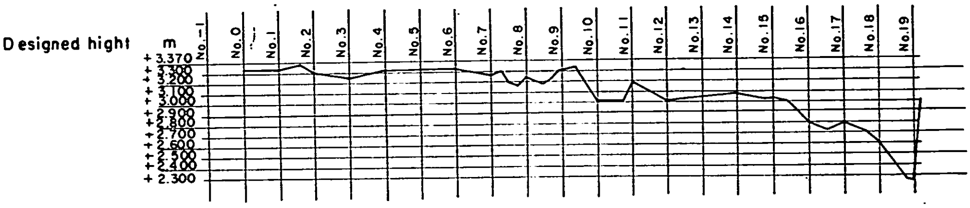

(b) At a Line 20 meters Distant from the Face Line

Fig. 9 Settlements of Nakajima (−10m) Wharf

Port where Sites A to D are located[8]. As will be explained later, liquefaction took place mainly at the area which was originally under sea water. Sites E and F are located on Ishinomaki Fishery Port. They were originally the same reclaimed ground, but Site E was later improved by the technique of sand compaction piles.

3.2 Nakajima (−10 m) Wharf (Site A)

(1) Liquefaction Data and Associated Damages to the Structures[8]

Figure 7 shows a cross section of Nakajima (−10 m) Wharf. The wharf was constructed from 1970 to 1971. The wharf is made of sheet piles. The anchorage of the front wall is also made of sheet piles. The seismic coefficient of 0.1 was used in designing the wharf.

Figure 8 shows residual horizontal displacements of the face line of the wharf. The maximum residual displacement is 57 cm at the south end of the wharf. The second-largest residual displacement of 28 cm is recorded at the middle part of the wharf around the section No. 12. Displacement is linearly increasing from the north end to south direction for the most part except for the south end. Figure 9 shows ground settlements of the wharf; Fig. 9 (a) along the face line and Fig. 9 (b) along the line 20 meters distant from the face line. The line is located one meter behind the anchorage. The maximum settlement at the face line is 5 cm and one at the line behind the anchorage is 100 cm. Both of the maximum settlements take place at the south end of the wharf. A typical section of residual deformation is shown in Fig. 10. The average settlement of the quay surface ranges from 30 cm to 50 cm. Photo 1 shows deformation of the quay surface above the anchorage.

According to the reports by the construction office of the Ishinomaki Port, sand boils were observed during the earthquake at the quay surface and they continued about two hours. The maximum height of the sand boils was about 30 cm. The diameters of the sand boils measured after the earthquake were about 5 cm.

Thus, significant liquefaction took place at least at the south end of Nakajima

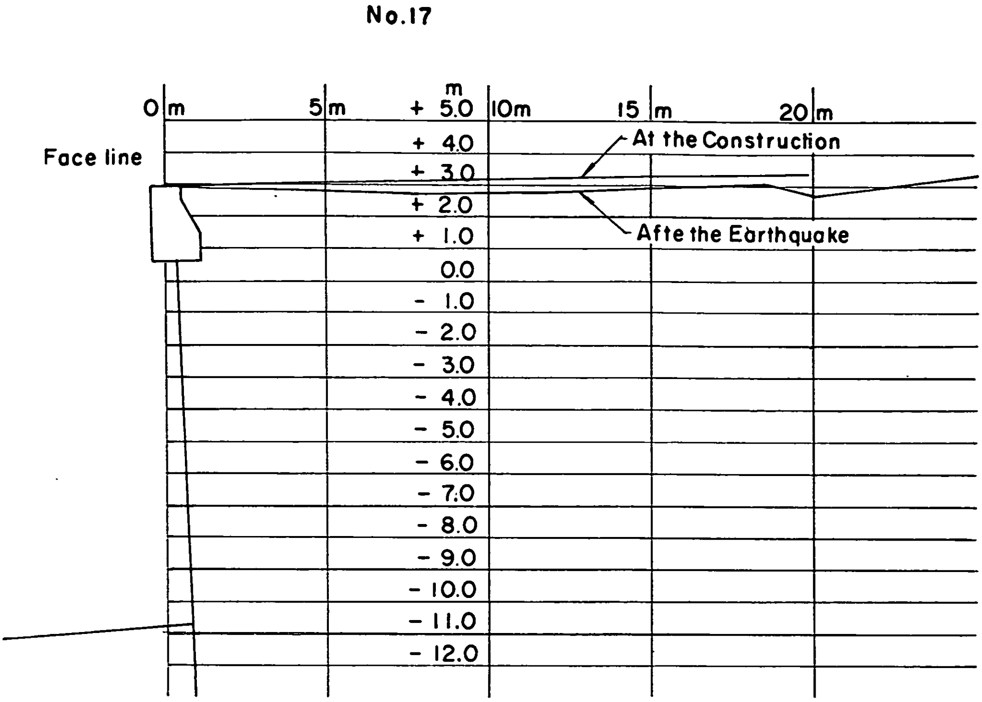

Fig. 10 Typical Section of Residual Deformation at Nakajima (—10m) Wharf (at No. 17 Locaction on **Fig. 8**)

Photo 1 Damages at the quay surface above the anchorage at Nakajima (—10m) Wharf

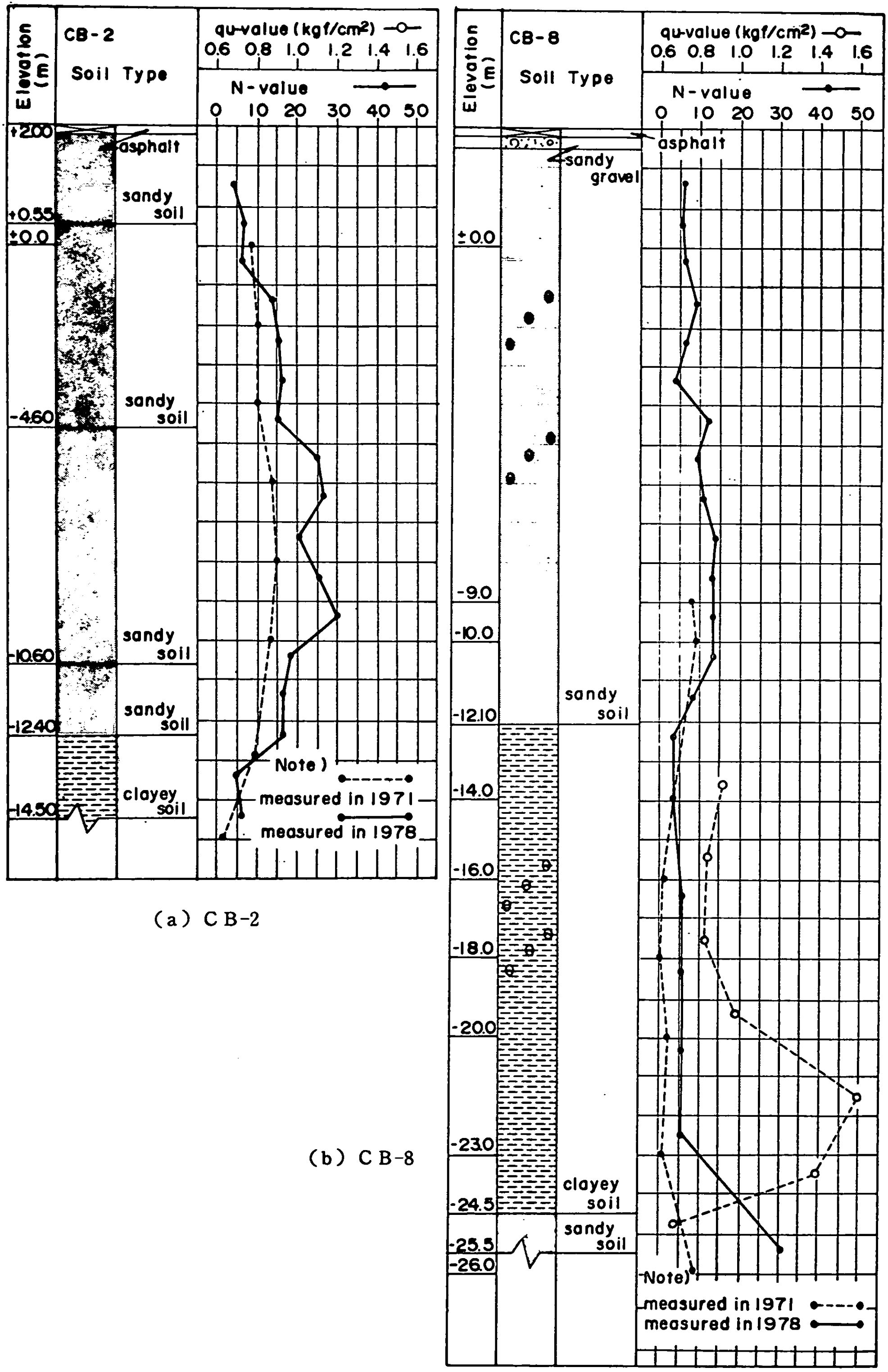

(a) CB-2

(b) CB-8

Fig. 11 Boring Logs of Nakajima (−10m) Wharf (Number Indicates the Location in **Fig. 8**)

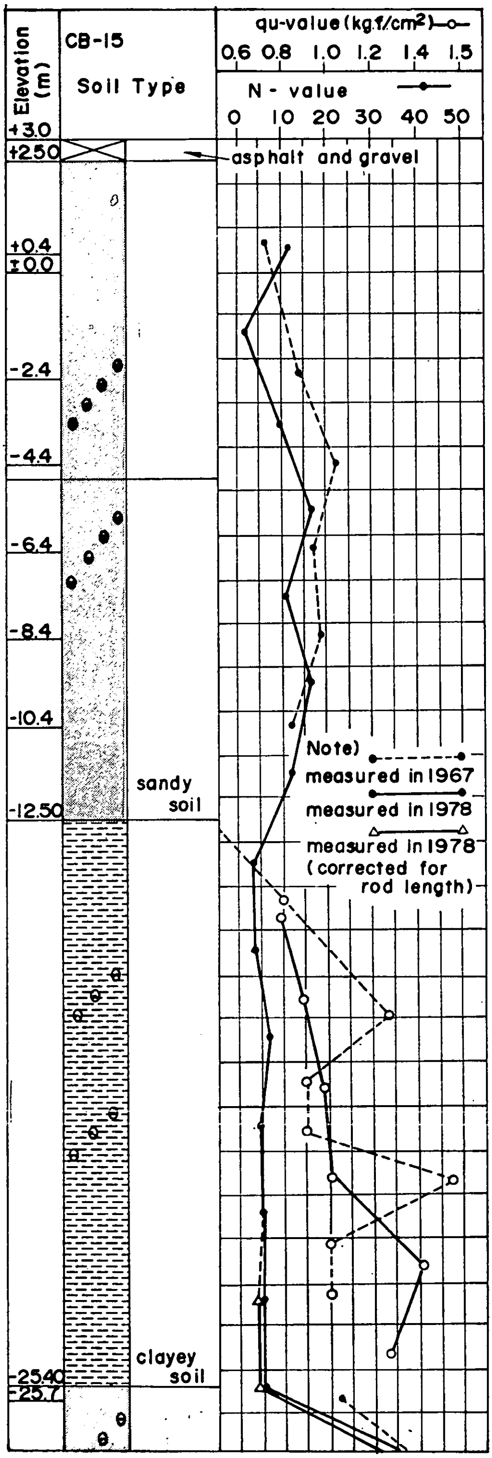
Elevation (m)
CB-15
Soil Type
qu-value (kgf/cm²)
0.6 0.8 1.0 1.2 1.4 1.5
N - value
0 10 20 30 40 50
+3.0
+2.50
+0.4
±0.0
-2.4
-4.4
-6.4
-8.4
-10.4
-12.50
-25.40
-25.7
asphalt and gravel
sandy soil
clayey soil
Note)
measured in 1967
measured in 1978
measured in 1978 (corrected for rod length)

(c) CB-15

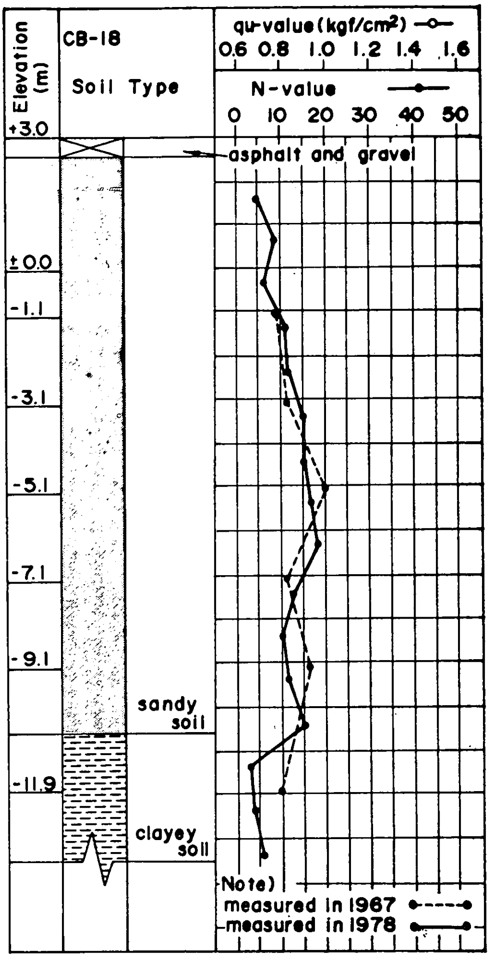
Elevation (m)
CB-18
Soil Type
qu-value (kgf/cm²)
0.6 0.8 1.0 1.2 1.4 1.6
N-value
0 10 20 30 40 50
+3.0
±0.0
-1.1
-3.1
-5.1
-7.1
-9.1
-11.9
asphalt and gravel
sandy soil
clayey soil
Note)
measured in 1967
measured in 1978

(d) CB-18

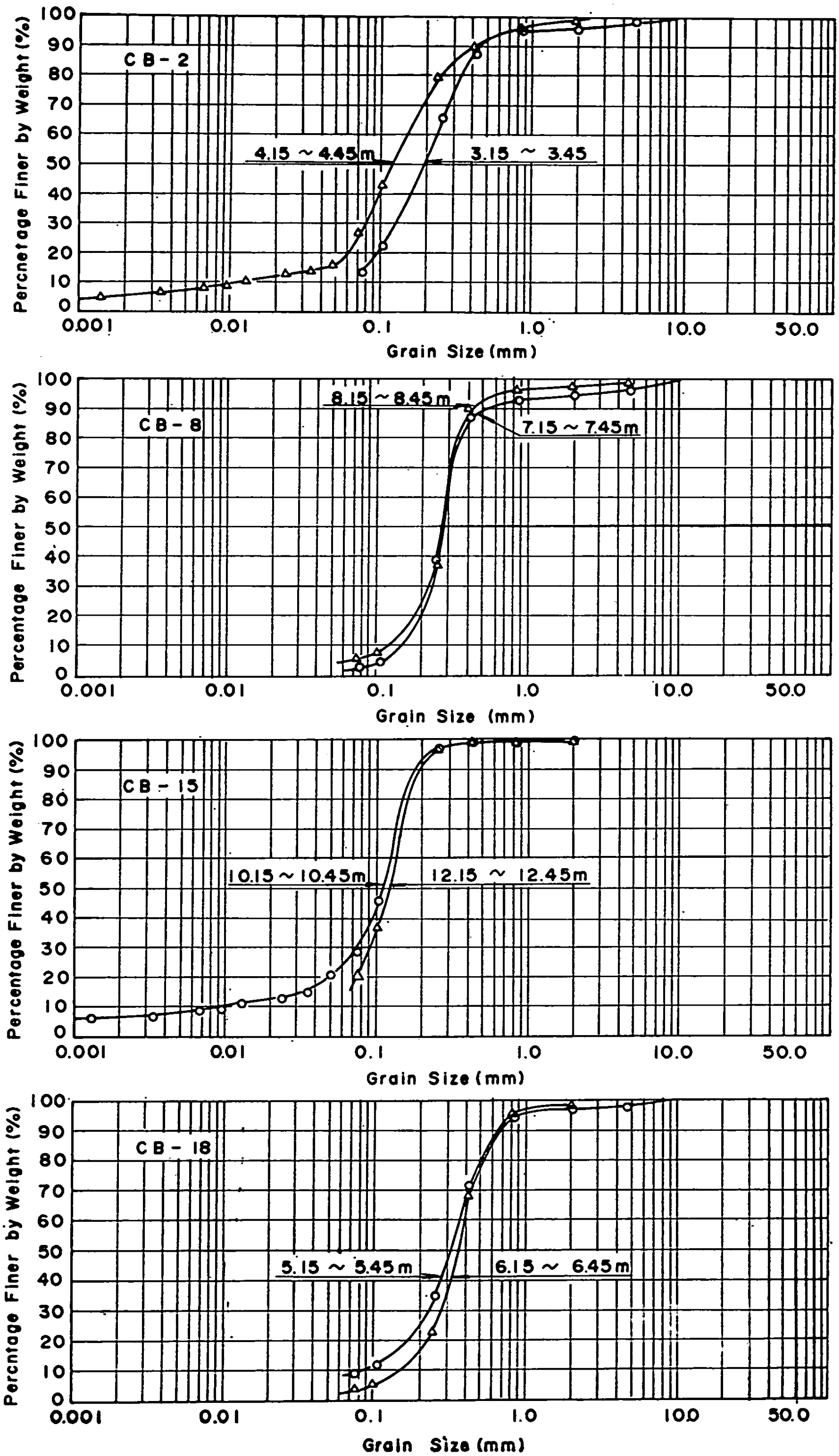

Fig. 12 Grain Size Accumulation Curves for Soils at Niakajima (—10m) Wharf

(−10 m) Wharf. Hereafter, Nakajima (−10 m) Wharf is designated as Site A.

(2) Soil Conditions[8)]

Figure 11 shows boring logs at Site A. The log labels such as CB-2 correspond to the locations indicated in Fig. 8. The data indicated by the broken lines and the solid lines were measured before and after the earthquake, respectively. The N-values of standard penetration test shown on these boring logs are almost the same along the full length of the wharf, while the degree of deformation of the wharf is significant only at the south end. If we look into these data in detail, we can find that the N-values are somewhat greater at CB-18 than at CB-8. The degree of deformation of the wharf is contradictory to the conventional concept that liquefaction strength and shear strength is great when the N-value is large. The contradiction indicates some difficulties to estimate liquefaction potential and related parameters of liquefaction model from the N-value of standard penetration test.

Figure 12 shows the grain size accumulation curves for sandy soils at Site A. The average grain size ranges from 0.1 to 0.3 mm and the fines content ranges from less than 5% to 30%.

For the present study, the boring log of CB-15 was considered representative of site conditions for estimating parameters of the liquefaction model. It is the only boring log which includes the data on the base rock formation at Site A.

3.3 Hiyori Wharf (Site B and Site C)

(1) Liquefaction Data and Associated Damages to the Structures[8)]

Hiyori Wharf was constructed around 1968 and comprises two segments. One

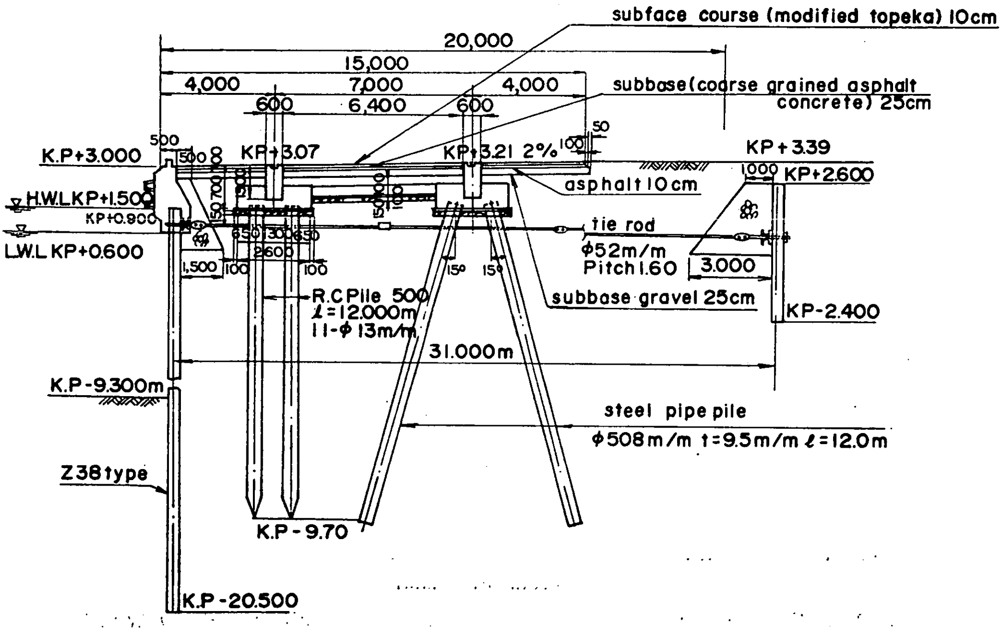

Fig. 13 Cross Section of Hiyori (−9m) Wharf (Unit in meter)

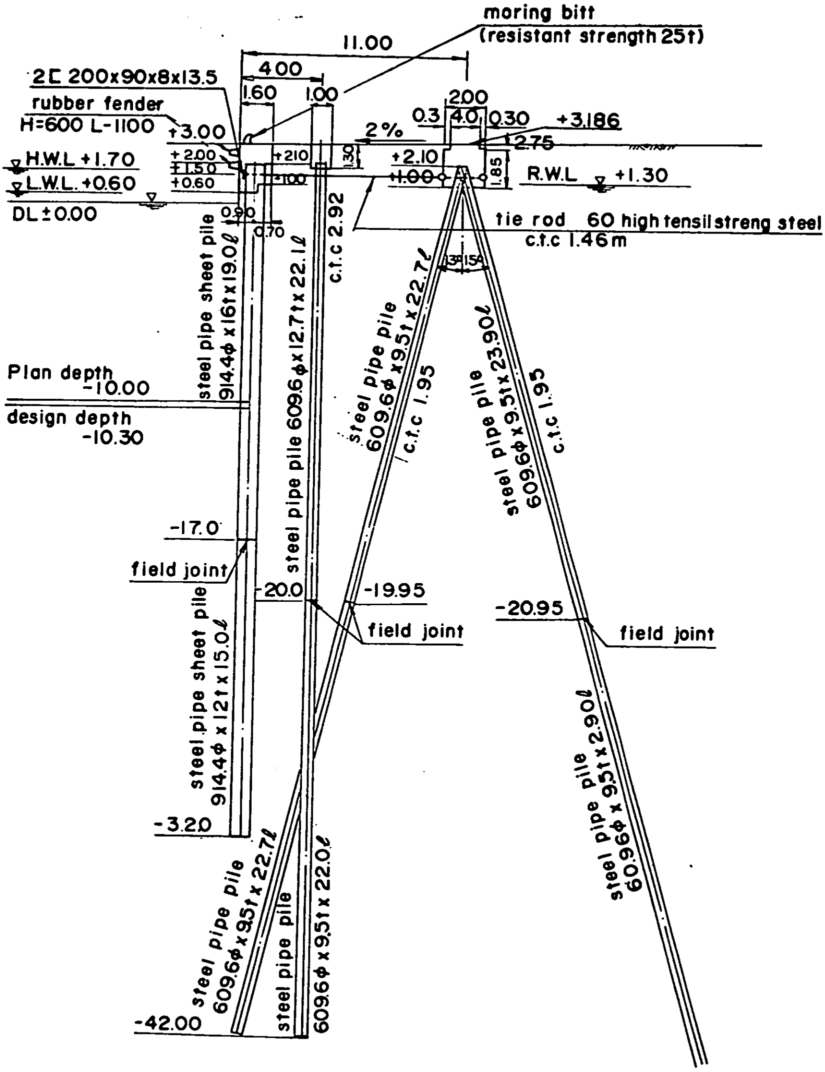

Fig. 14 Cross Section of Hiyori (−10m) Wharf (Unit in meter)

is Hiyori (−9 m) Wharf and the other is Hiyori (−10 m) Wharf. The former is located on the south side and the latter on the north side. Cross sections of these wharves are shown on Figs. 13 and 14. Hiyori (−9 m) Wharf is made of the sheet piles with the sheet pile anchorage. Hiyori (−10 m) Wharf is made of the steel pipe piling bulkhead with the coupled pile anchorage. A seismic coefficient of 0.1 was used in designing these wharves.

The residual horizontal displacement of the face line of the wharf is shown in Fig. 15. The maximum displacement is 57 cm at the south end. Significant displacements took place only at Hiyori (−9 m) Wharf. Figure 16 shows settlements along the face line of the wharf. The maximum settlement is 15 cm. The amount of settlement at Hiyori (−9 m) Wharf is greater than that at Nakajima (−10 m) Wharf. Figure 17 shows typical deformations of sheet pile bulkheads at

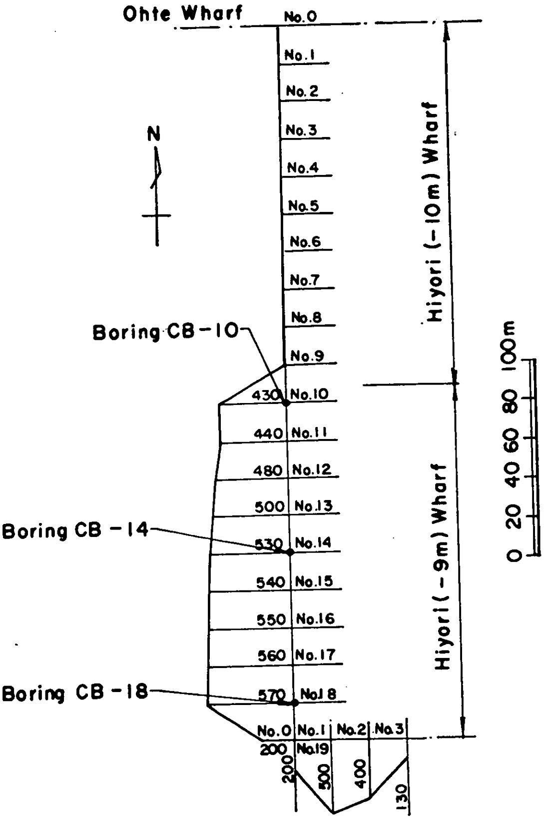

Fig. 15 Residual Horizontal Displacements at Face Line of Hiyori Wharf (Unit in mm for Displacements)

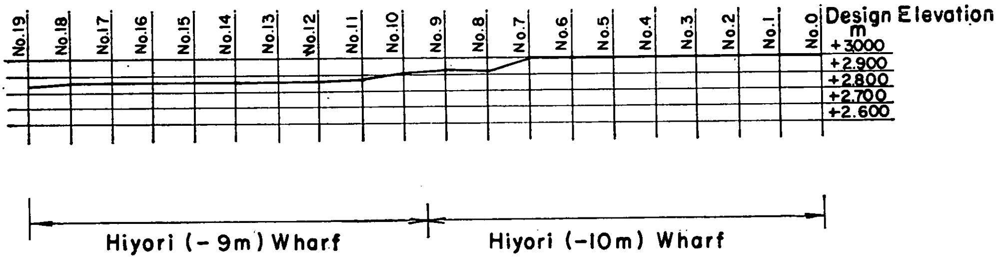

Fig. 16 Settlements of Hiyori Wharf

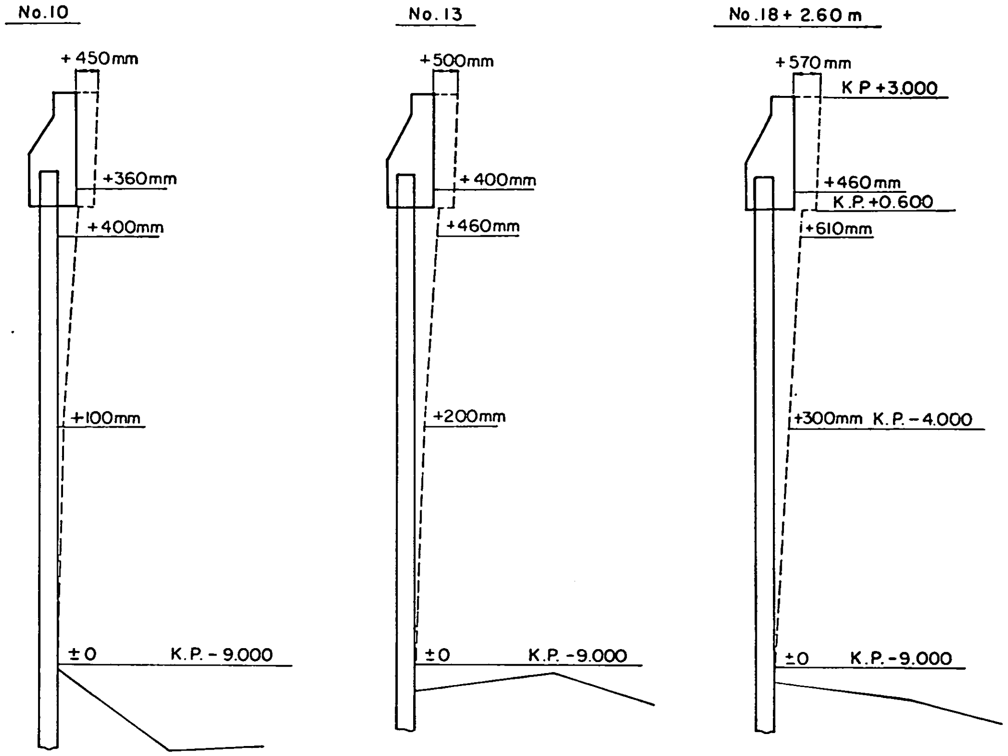

Fig. 17 Typical Cross Section of Residual Deformation at Hiyori (−9m) Wharf (Number indicates the Location on **Fig. 15**) (Unit in mm for displacements)

Hiyori (−9 m) Wharf.

Photo 2 shows cracks at the surface of the wharf and sand boils from the cracks at Hiyori (−9 m) Wharf.

The above-mentioned deformation and sand boils clearly indicate that liquefaction took place at Hiyori (−9 m) Wharf. On the other hand, there was no deformation or no sand boils took place at Hiyori (−10 m) Wharf. Therefore, it is reasonable to conclude from the engineering viewpoint that liquefaction did not take place at Hiyori (−10 m) Wharf. Hereafter, the ground area which corresponds to Hiyori (−9 m) Wharf is designated Site B and that which corresponds to Hiyori (−10 m) Wharf is designated Site C.

Photo 2 also shows a derailed unloader on the Hiyori (−10 m) Wharf. This unloader has hinged legs on the seaward side. The derailement is one of the important indications of the intensity of the ground surface motion during the earthquake, particularly because there was no seismometer on the ground surface at Ishinomaki Port during the earthquake.

(2) Soil Conditions[8)]

Figure 18 shows boring logs of Hiyori Wharf. Log labels such as CB-5 correspond to the locations indicated in Fig. 15. N-values and undrained shear strengths q_u shown by the broken lines in Fig. 18 are the data measured before

Photo 2 Sand boils and Derailement of Unloader at Hiyori (−9m) Wharf

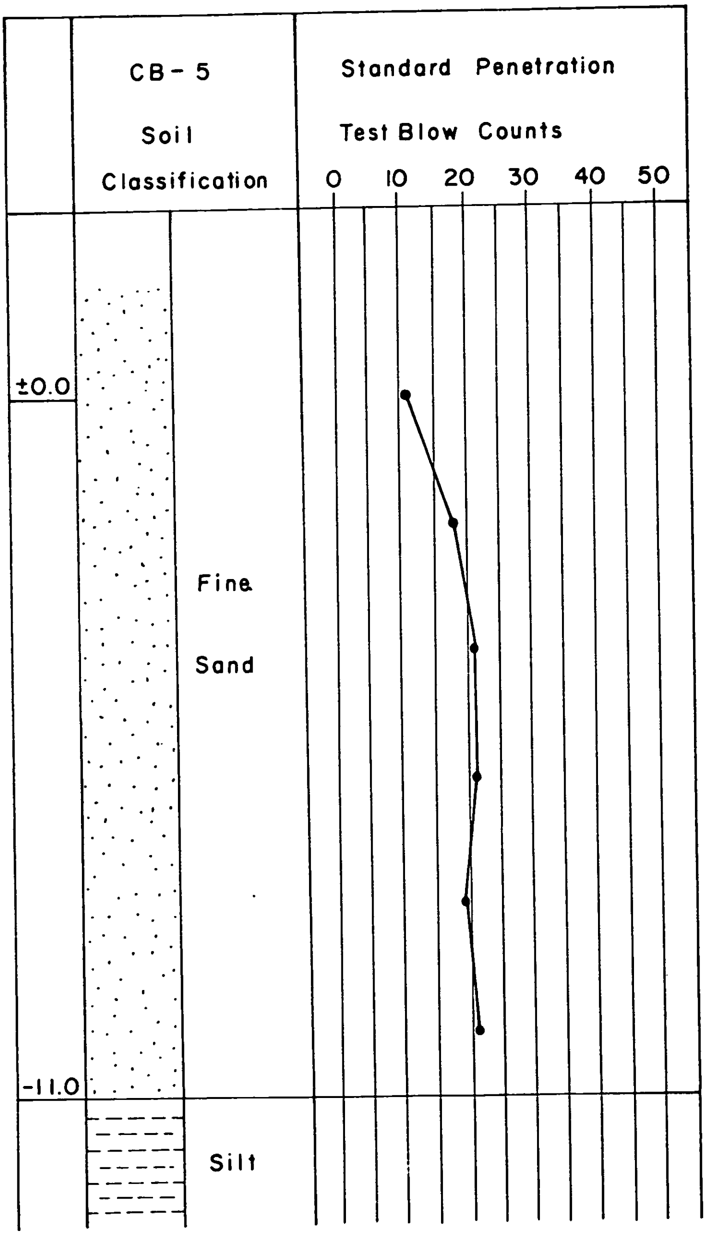

Measured in 1967

(a) CB-5

Fig. 18 Boring Logs of Hiyori Wharf (Number indicates the Location in Fig. 15)

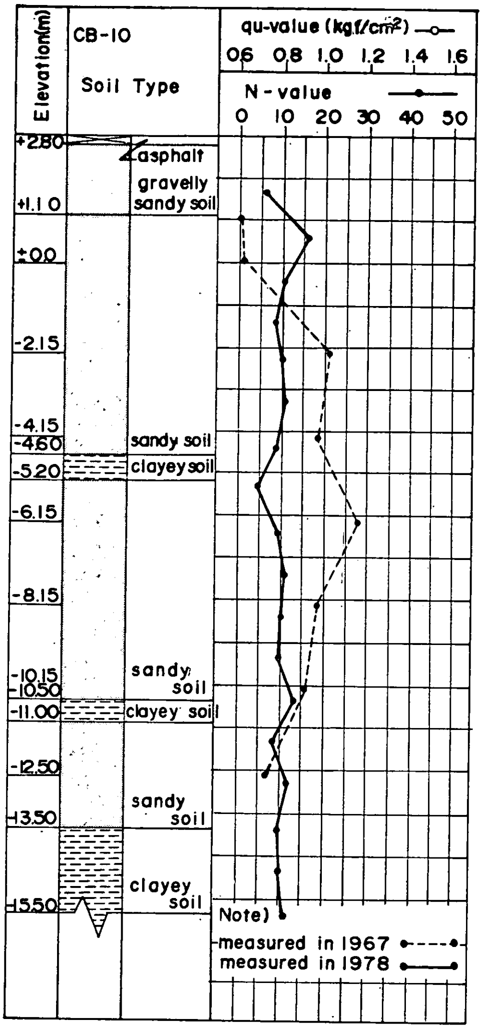
Elevation(m)
CB-10
Soil Type
qu-value (kgf/cm²) —○—
0.6 0.8 1.0 1.2 1.4 1.6
N-value —●—
0 10 20 30 40 50
+2.80
asphalt
gravelly sandy soil
+1.10
±0.0
-2.15
-4.15
-4.60
sandy soil
-5.20
clayey soil
-6.15
-8.15
-10.15
-10.50
sandy soil
-11.00
clayey soil
-12.50
-13.50
sandy soil
-15.50
clayey soil
Note)
measured in 1967 ●----●
measured in 1978 ●——●

(b) CB-10

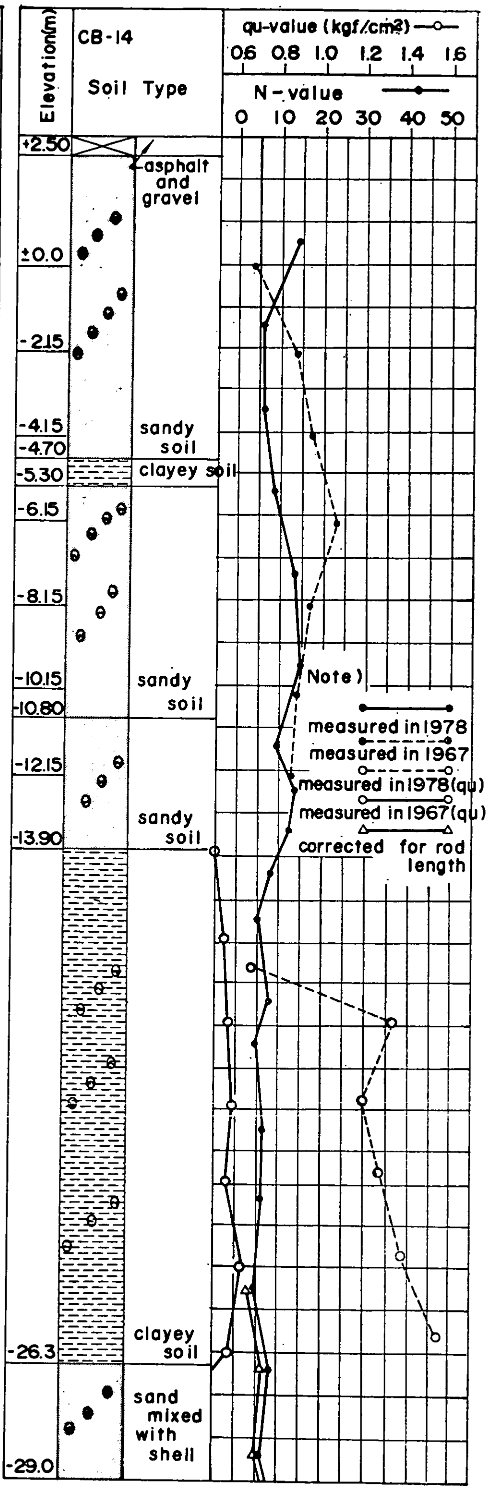
Elevation(m)
CB-14
Soil Type
qu-value (kgf/cm²) —○—
0.6 0.8 1.0 1.2 1.4 1.6
N-value —●—
0 10 20 30 40 50
+2.50
asphalt and gravel
±0.0
-2.15
-4.15
-4.70
sandy soil
-5.30
clayey soil
-6.15
-8.15
-10.15
-10.80
sandy soil
-12.15
-13.90
sandy soil
-26.3
clayey soil
-29.0
sand mixed with shell
Note)
measured in 1978
measured in 1967
measured in 1978(qu)
measured in 1967(qu)
corrected for rod length

(c) CB-14

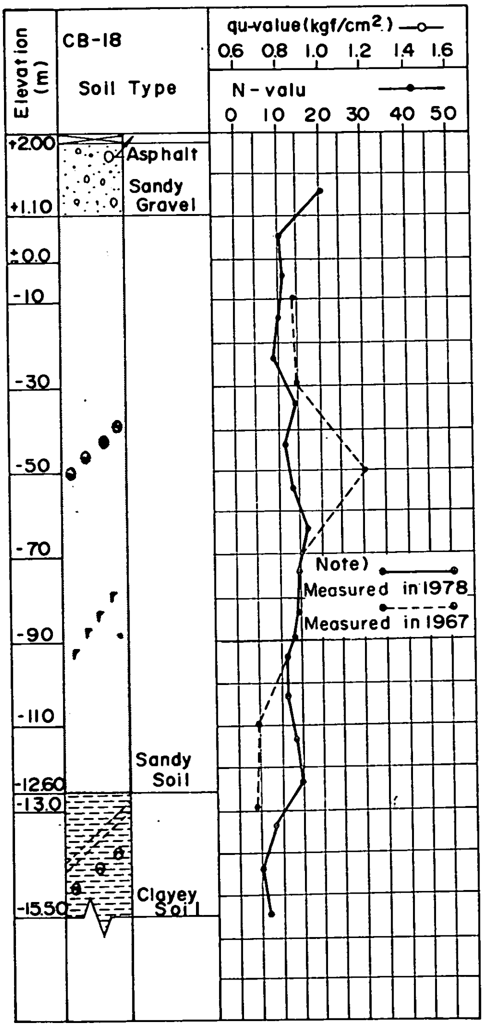
Elevation (m)
CB-18
Soil Type
qu-value(kgf/cm2)
0.6 0.8 1.0 1.2 1.4 1.6
N-valu
0 10 20 30 40 50
+2.00
+1.10
±0.0
-1.0
-3.0
-5.0
-7.0
-9.0
-11.0
-12.60
-13.0
-15.50
Asphalt
Sandy Gravel
Sandy Soil
Clayey Soil
Note)
Measured in 1978
Measured in 1967

(d) CB-18

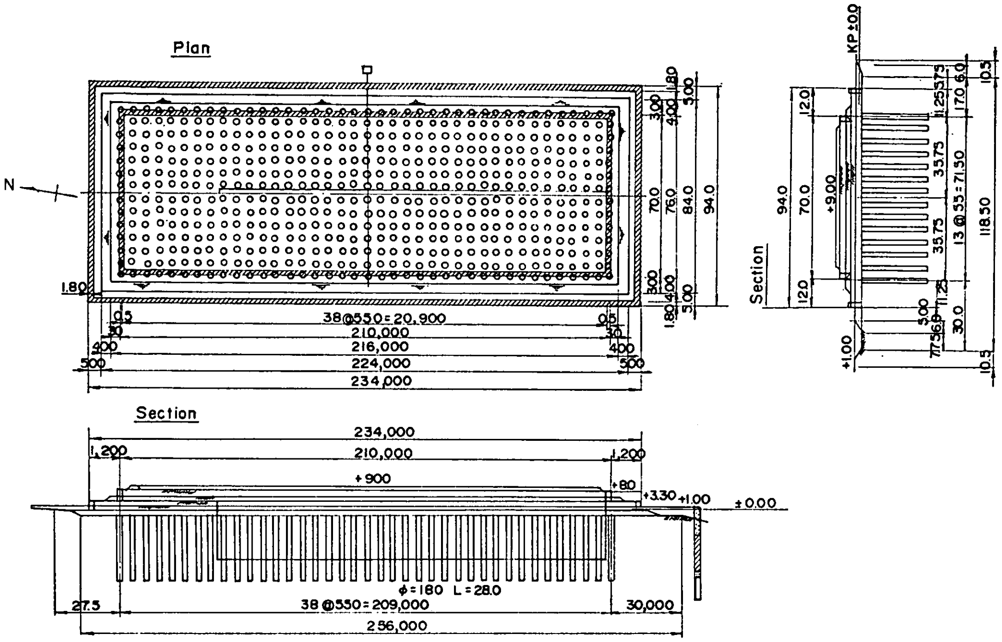

Fig. 19 Sand Piles Installed for Improvement of Clayey Layer Below the Surface Sand Layer (Unit in meter)

the earthquake and those shown by the solid lines are the data measured after the earthquake.

The original ground at Hiyori (−9 m) Wharf was not very different from that at Hiyori (−10 m) Wharf. However, Hiyori (−9 m) Wharf has undergone soil improvement by means of sand piles as shown in Fig. 19, in order to improve a clayey layer 17 meter thick below the surface sand layer. The improved area is shown in Fig. 20. Water jets were used to dig holes for the sand piles through rather stiff sand layers. As a result, the sand layer was loosened by the water jets.

The N-values and q_u-values shown by the broken lines in Fig. 18 are those measured before the water jet disturbance at Hiyori (−9 m) Wharf. There is no data obtained just before the earthquake for this wharf. As will be explained in the next section, however, there is a good reason to use data obtained after the earthquake as a substitute for the data before the earthquake.

Figure 21 shows the grain size accumulation curves for sandy soils at Hiyori Wharf. The average grain size is about 0.2 mm and the fines content ranges from 10 to 20%.

For the present study, the boring log of CB-14 was selected as representative of conditions at Hiyori (−9 m) Wharf (Site B) for estimating parameters of the liquefaction model. It is the only boring log which includes the data on the base gravel layer at the site. For Hiyori (−10 m) Wharf (Site C), the boring log of CB-5 was selected being the only log available.

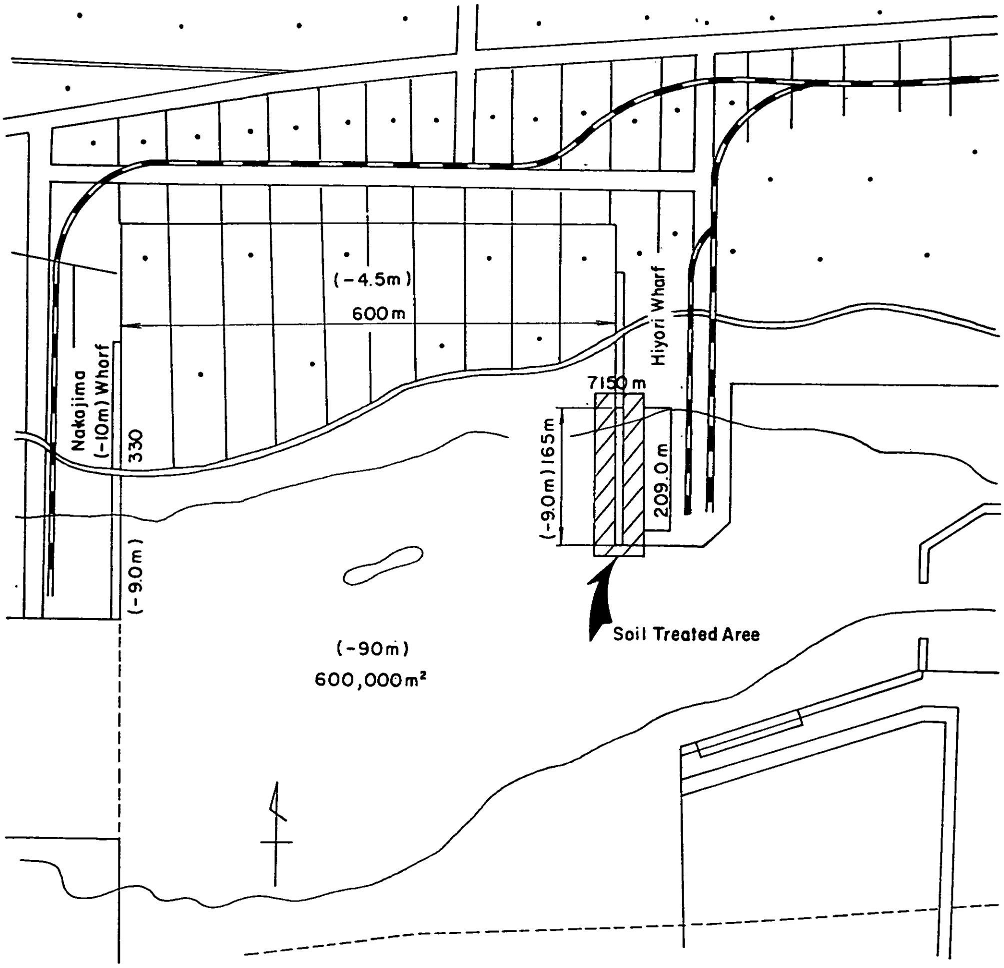

Fig. 20 Soil Treated Area

3.4 Shiomi (−4.5 m) Wharf (Site D)

(1) Liquefaction Data and Associated Damages to the Structures[5]

Figure 22 shows a cross section of Shiomi (−4.5 m) Wharf. The wharf was constructed about 1970. The wharf is made of the sheet pile bulkhead with the sheet pile anchorage. Seismic coefficient of 0.1 was used in designing the wharf.

The residual horizontal displacements of the face line of the wharf are shown in Fig. 23. The maximum displacement is 116 cm at the central part. The settlements along the face line of the wharf are shown in Fig. 24. The maximum settlement is 10 cm. Typical deformation patterns of sheet pile bulkheads are shown in Fig. 25. The numbers in Fig. 25 for each section indicate the location of the section designated in Fig. 23. For example, No. 3+10 means that the location of the section is 10 meters away from the location No. 3 toward the location No. 4. The sections of No. 3+10, No. 9, and No. 7+10 were inspected

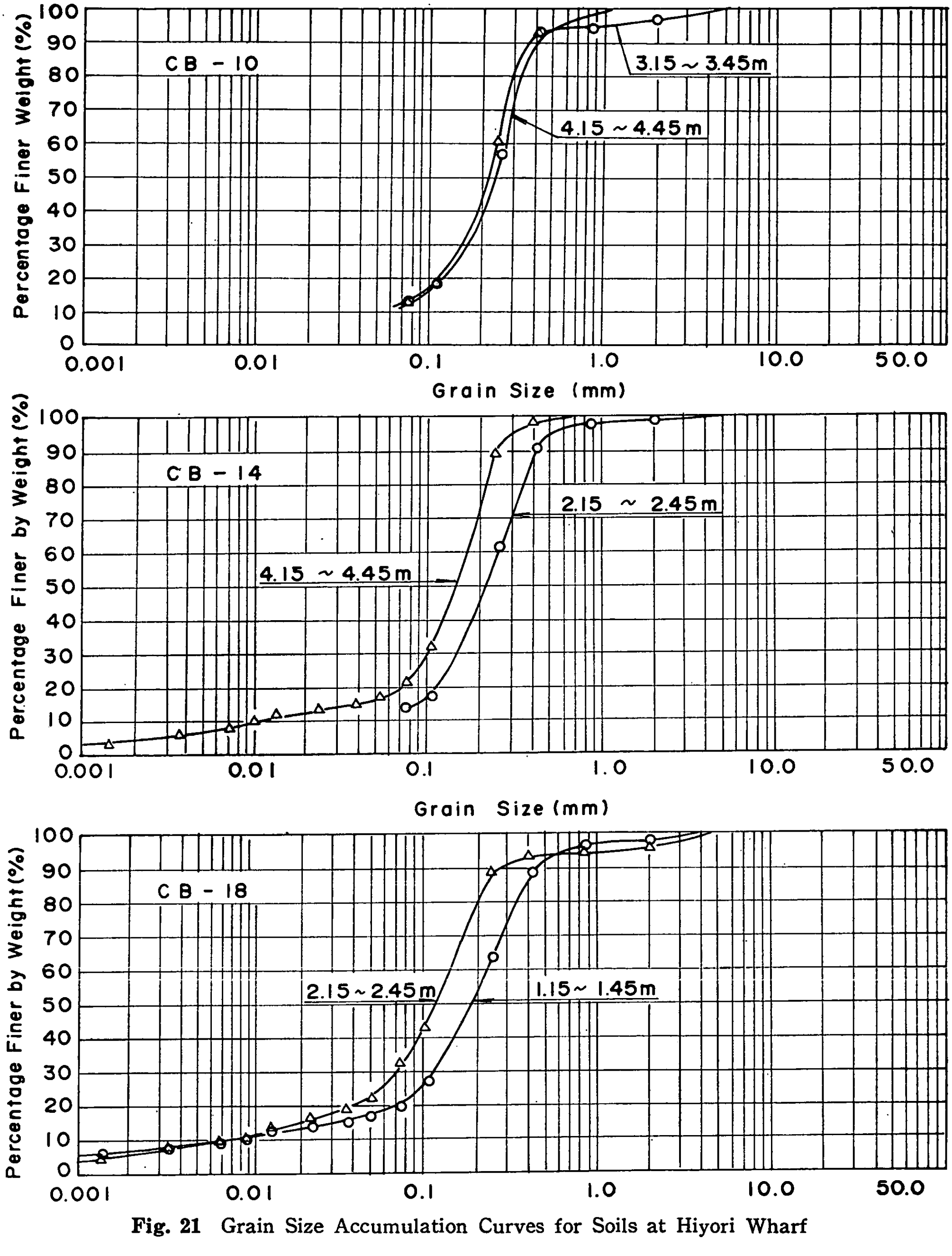

Fig. 21 Grain Size Accumulation Curves for Soils at Hiyori Wharf

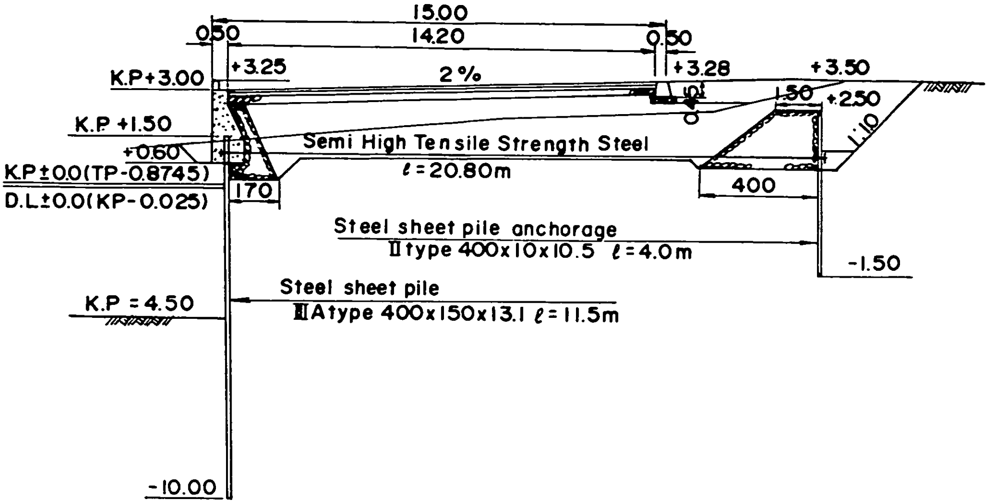

Fig. 22 Cross Section of Shiomi (—4. 5m) Wharf (Unit in meter)

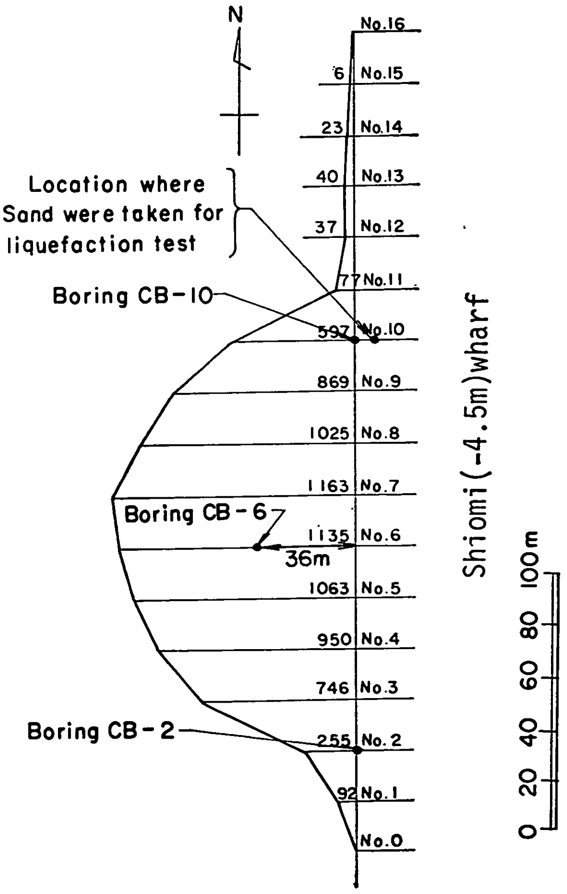

Fig. 23 Residual Horizontal Displacement of the Face Line of Shiomi (—4. 5m) Wharf (Unit in mm for Displacements)

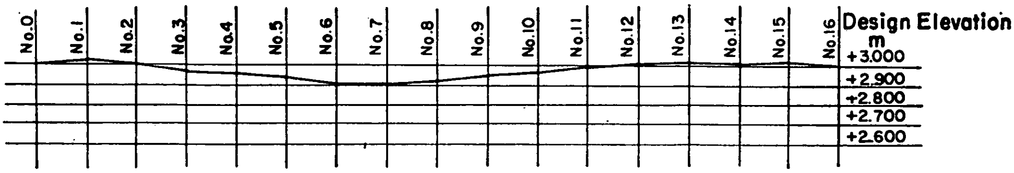

Fig. 24 Settlements of Shiomi (−4.5m) Wharf

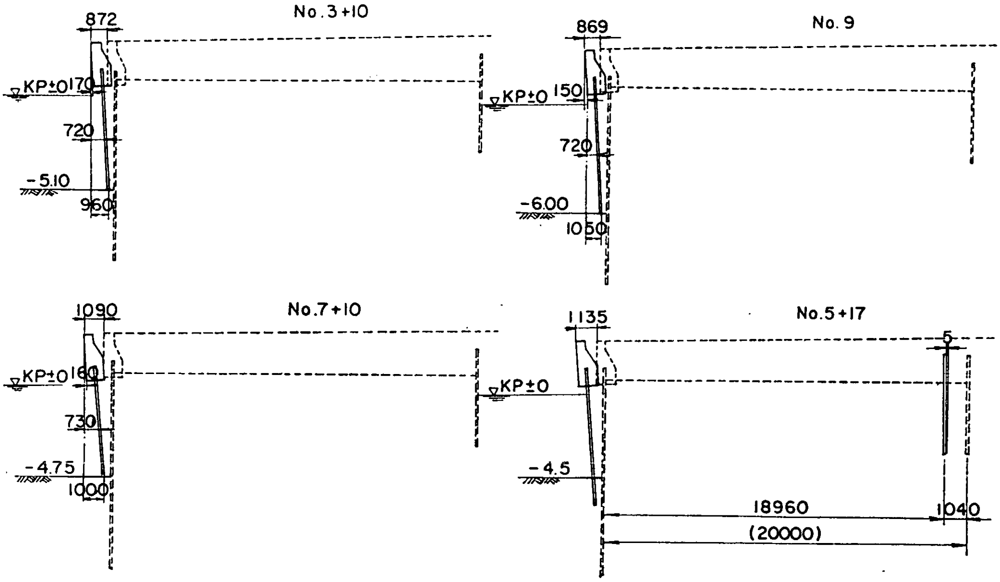

Fig. 25 Typical Deformation of Shiomi (−4.5m) Wharf (Unit in mm for displacements)

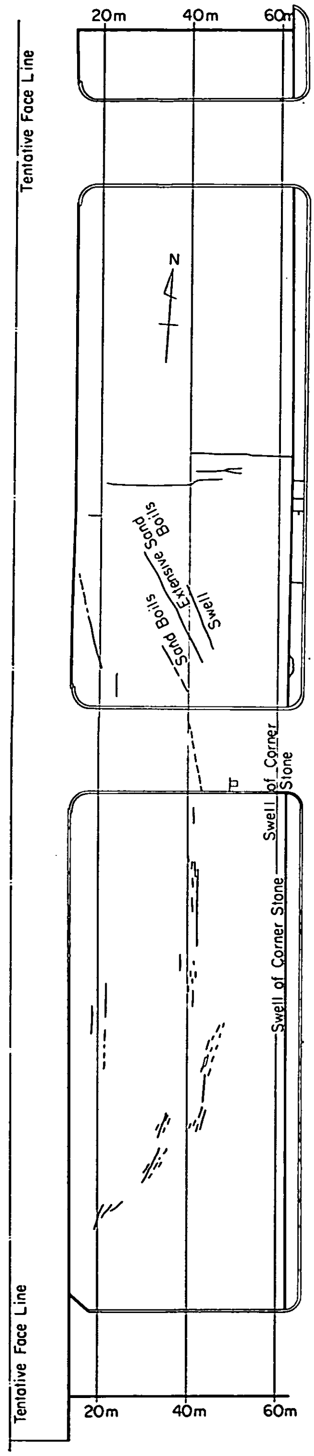

Fig. 26 Cracks at Shiomi (−4.5m) Wharf

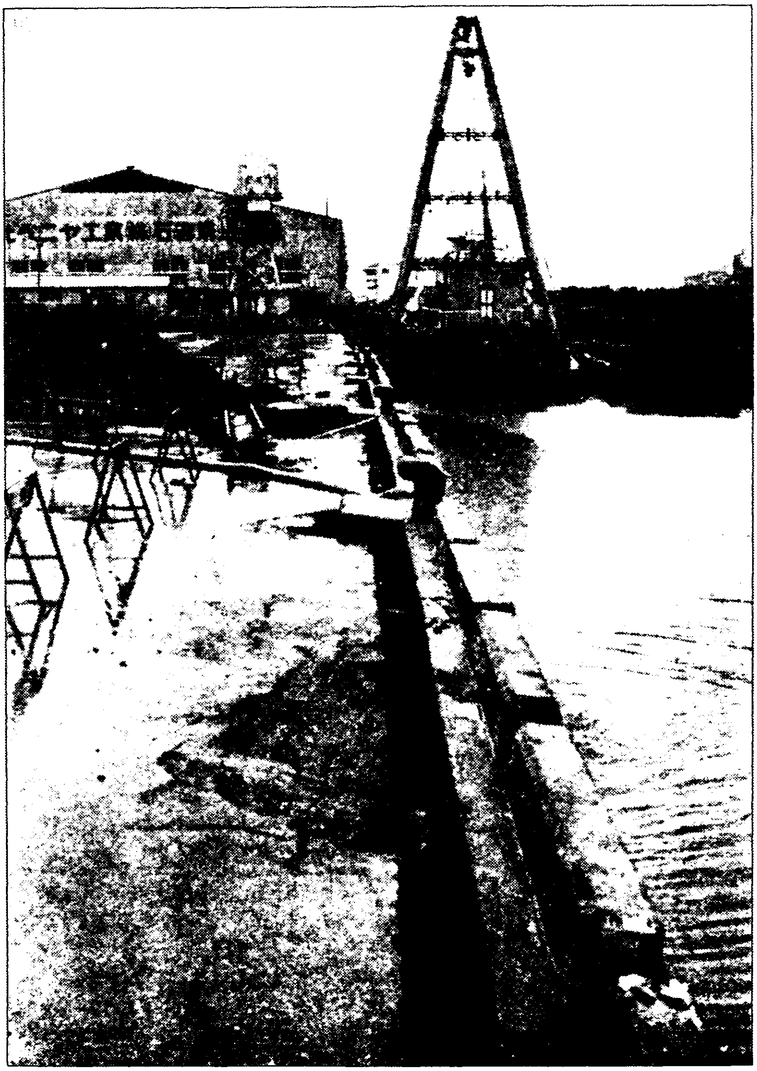

Photo 3 Cracks and Sand Boils at a Yard behind Shiomi (−4.5m) Wharf

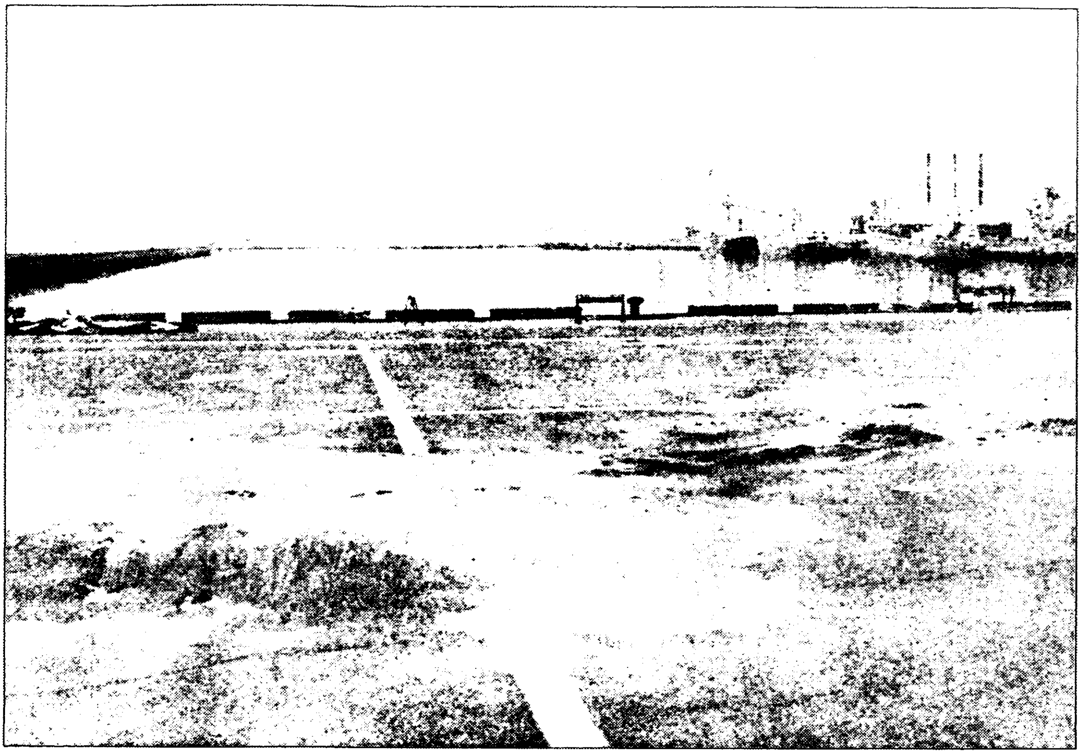

Photo 4 Sand Boils at Shiomi (−4.5m) Wharf

by divers. The section of No. 5+17 was investigated in dry condition after the ground behind the face line was dug out.

There were cracks on the surface of the ground pavements from 40 to 60 meters behind the face line as shown in Fig. 26. There were also sand boils at the cracks as shown in Photos 3 and 4.

The above-mentioned data show that liquefaction certainly took place at Shiomi (−4.5 m) Wharf. The area at Shiomi (−4.5 m) Wharf is designated Site D hereafter.

Besides these liquefaction evidences, the center line of an asphalt paved road located about 90 meters behind the face line showed a deflection toward the sea, although it was originally a straight line. This evidence and the formation of the cracks shown in Fig. 26 together with the residual deformation of the bulkhead indicate that a land slide of small extent took place in this area. It is not easy to decide, however, whether the slide is related to the liquefaction or not.

(2) Soil Conditions[8)]

Figure 27 shows boring logs at Shiomi (−4.5 m) Wharf. The number attached to each boring log such as CB-2 corresponds to the location indicated in Fig. 23. Broken lines in Fig. 23 indicate data measured before the earthquake; those shown by the solid lines were measured after the earthquake. Figure 28 shows the grain size accumulation curves of sandy soils at Shiomi (−4.5 m) Wharf. The average grain size is about 0.3 mm and the fines content is about 10%.

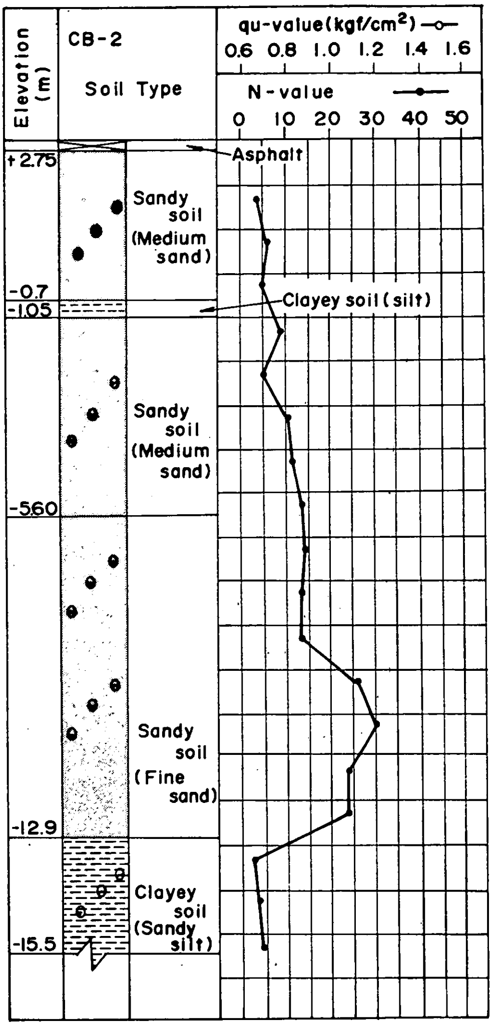

(a) CB-2

Fig. 27 Boring Logs at Shiomi (−4.5m) Wharf (Number Corresponds to the Location Indicated in **Fig. 23**)

Boring log, CB-10, which contains the data obtained before the earthquake, was selected for estimating the parameters of the liquefaction model.

Generally speaking, the N-values and q_u-values are affected by earthquake shaking. Figure 27 (c) shows, however, that the N-values measured before the earthquake are not significantly different from those measured after the earthquake in this case. Therefore, it is considered that the N-values and q_u-values measured after the earthquake might be used in analysis where data had not been measured before the earthquake. This is the basis for using data measured after the earthquake for analyses at Hiyori (−9 m) Wharf (Site B).

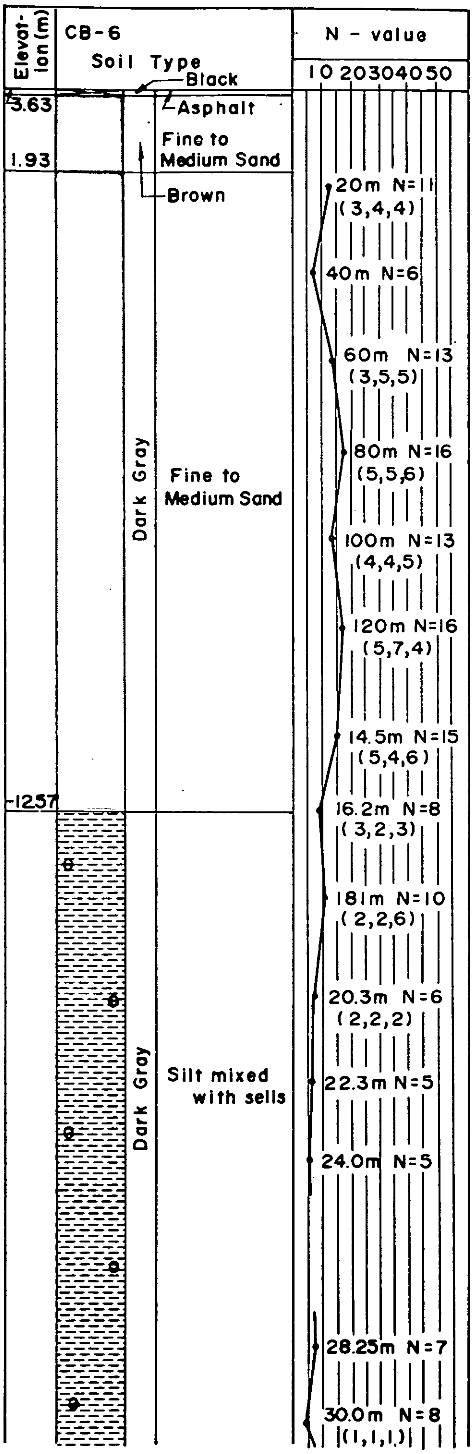
Elevat-ion (m)
CB-6
Soil Type
Black
Asphalt
3.63
1.93
Fine to Medium Sand
Brown
Dark Gray
Fine to Medium Sand
-12.57
Dark Gray
Silt mixed with sells
N - value
10 20 30 40 50
20m N=11 (3,4,4)
40m N=6
60m N=13 (3,5,5)
80m N=16 (5,5,6)
100m N=13 (4,4,5)
120m N=16 (5,7,4)
14.5m N=15 (5,4,6)
16.2m N=8 (3,2,3)
181m N=10 (2,2,6)
20.3m N=6 (2,2,2)
22.3m N=5
24.0m N=5
28.25m N=7
30.0m N=8 (1,1,1)

(b) CB-6

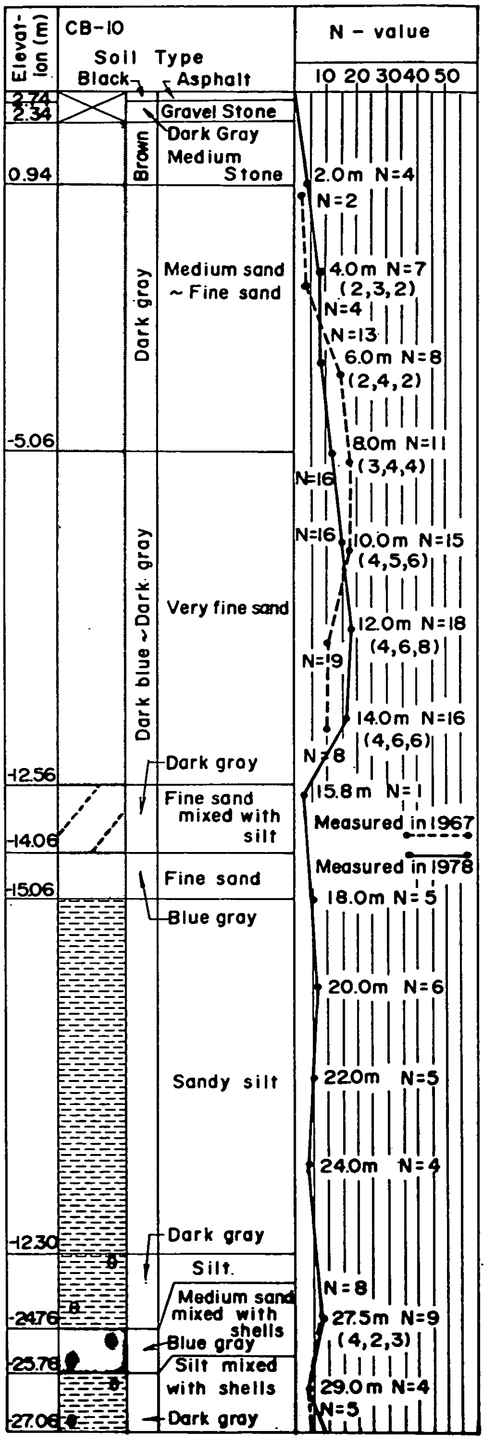
Elevat-ion (m)
CB-10
Soil Type
Black
Asphalt
2.74
2.34
Gravel Stone
Brown
Dark Gray Medium Stone
0.94
Dark gray
Medium sand ~ Fine sand
-5.06
Dark blue ~ Dark gray
Very fine sand
Dark gray
-12.56
Fine sand mixed with silt
-14.06
Fine sand
-15.06
Blue gray
Sandy silt
-12.30
Dark gray
Silt.
Medium sand mixed with shells
-24.76
Blue gray
-25.76
Silt mixed with shells
-27.06
Dark gray
N - value
10 20 30 40 50
2.0m N=4
N=2
4.0m N=7 (2,3,2)
N=4
N=13
6.0m N=8 (2,4,2)
8.0m N=11 (3,4,4)
N=16
N=16
10.0m N=15 (4,5,6)
12.0m N=18 (4,6,8)
N=19
14.0m N=16 (4,6,6)
N=8
15.8m N=1
Measured in 1967
Measured in 1978
18.0m N=5
20.0m N=6
22.0m N=5
24.0m N=4
N=8
27.5m N=9 (4,2,3)
29.0m N=4
N=5

(c) CB-10

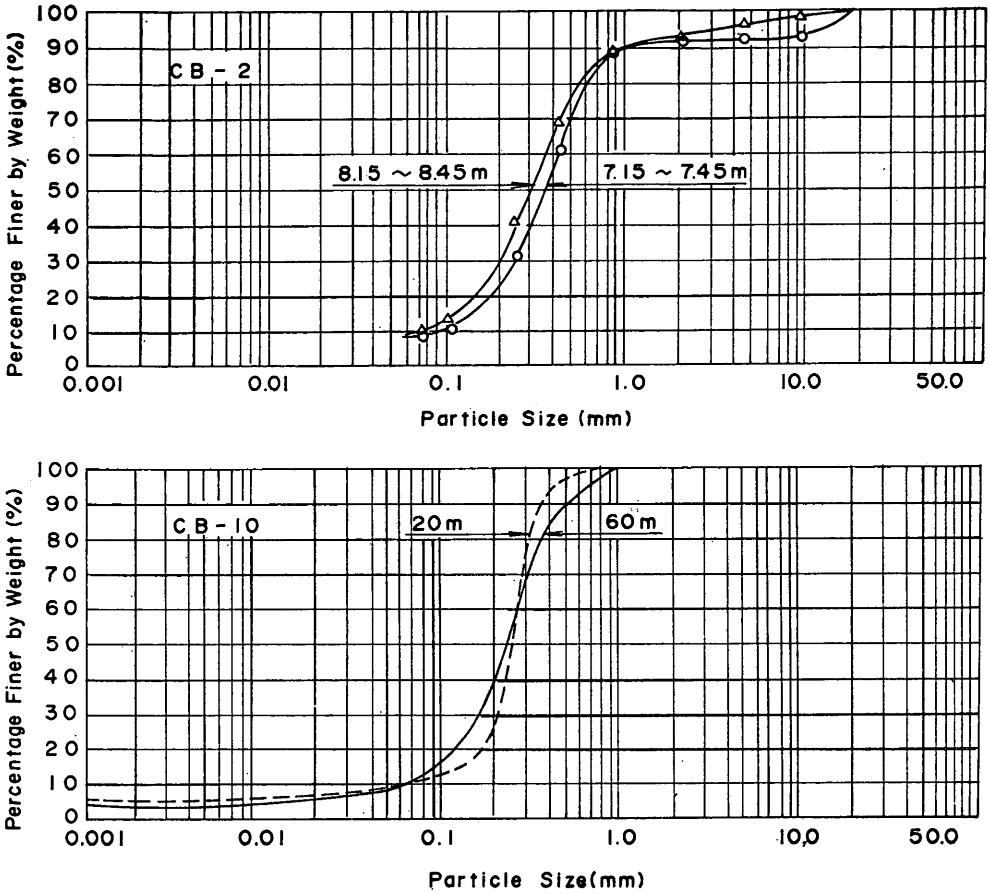

Fig. 28 Grain Size Accumulation Curves of Sands at Shiomi (−4.5m) Wharf

3.5 Oil Tank Yard and the Vicinity Area at Ishinomaki Fishery Port (Site E and Site F)

(1) Liquefaction Data8),9)

This area has previously been studied by Ishihara et al9). The location of the area is shown in Fig. 29. The area was originally a filled land with sands in the sea bed in front of the wharf close to the area under study. The ground just under oil tanks was improved by installing sand compaction piles as shown in Fig. 30. The sand piles were installed in triangular patterns with the spacing of 1.8 meters. There are three oil tanks in the yard. Dimensions of the tanks are 15.22 meters × ϕ23.24 meters, 14.20 meters × ϕ13.56 meters, and 9.20 meters × ϕ8.86 meters. The cross section of the greatest tank is shown in Fig. 30. The levels of oil contained in these tanks at the time of the earthquake were 6.67 meters, 5.62 meters, and 6.63 meters, respectively.

The oil tanks are considered to have suffered no residual deformation from the earthquake. No sand boils were observed in the compacted ground. On the other hand, sand boils were seen at many places in the area around the oil tank

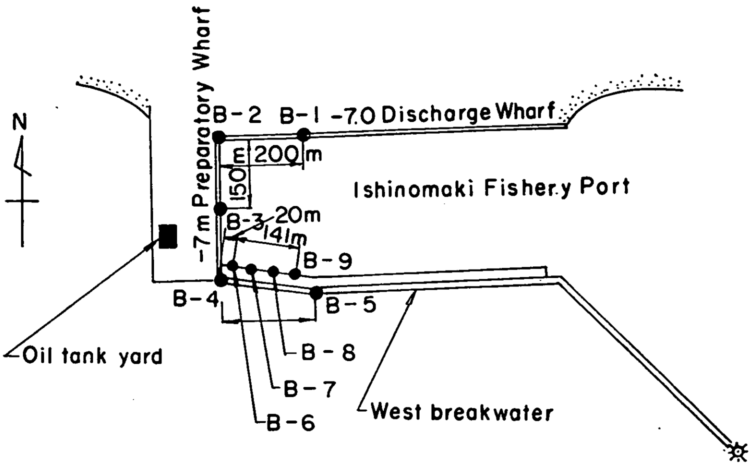

Fig. 29 Location of the Oil Tank Yard

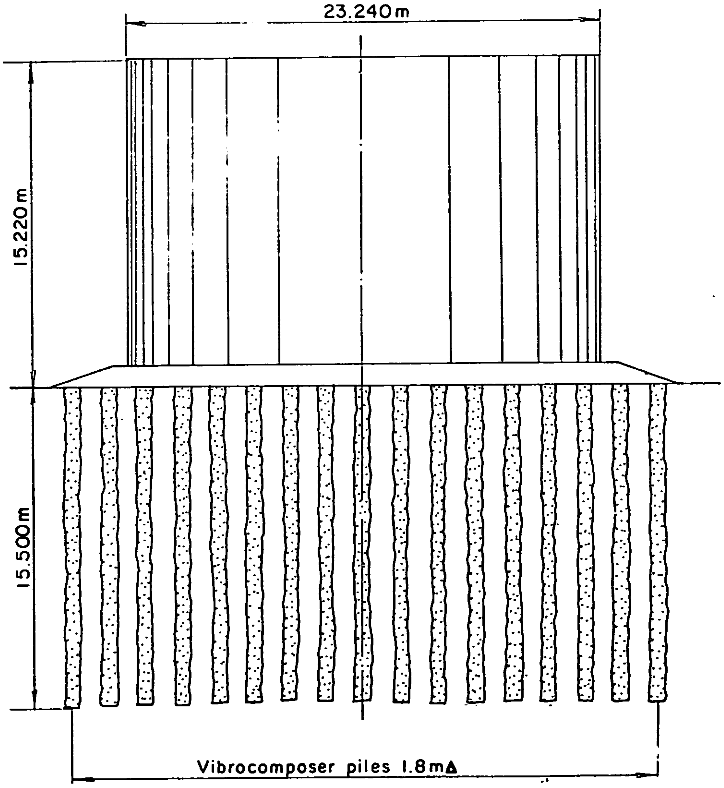

Fig. 30 Section of 6,000 kl Oil Tank and Sand Piles Installed Underneath

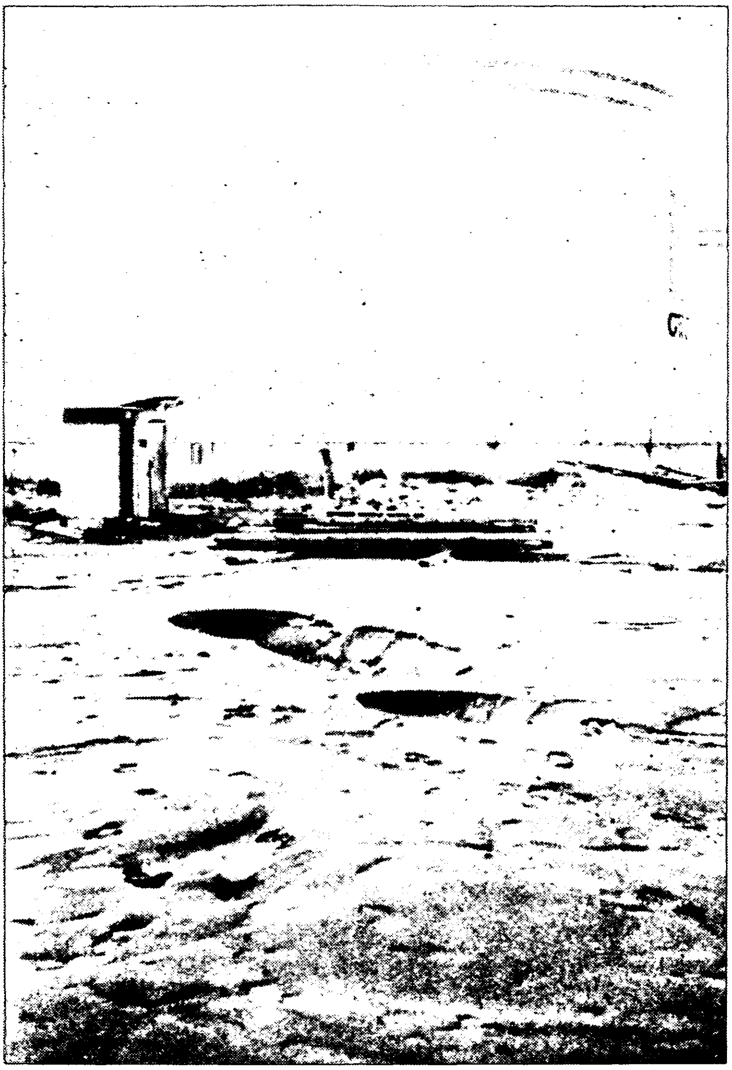

Photo 5 Sand Boils at the area around the oil tand yard at Ishinomaki Fishery Port

yard, even at the border of the yard as shown in Photos 5 and 6. No structures existed in the area around the oil tank yard. The oil tank yard which had no liquefaction is designated as Site E and the area around the yard which liquefied is designated as Site F hereafter.

(2) Soil Conditions8),9)

Figure 31 shows the soil types and N-values of the ground measured before and after soil compaction. Figures 32 and 33 show the grain size accumulation curves of the soils. The mean diameter is 0.1 to 0.2 mm and the fines content is about 10%.

Boring logs around these sites are shown in Fig. 34. The corresponding grain size accumulation curves are shown in Fig. 35. Figure 34 shows a rather great

Photo 6 Sand Boils at the border of the oil tank yard

variation in the N-values of sand layers. Figure 35 shows a tendency towards greater fines content in comparison with Figs. 32 and 33.

Boring logs shown in Fig. 31 were selected as representative of Site E and Site F for estimating the parameters of the liquefaction model for the present study.

3.6 Depth of Base Rock and Underground Water Level

(1) Depth of Base Rock at Ishinomaki Port

A soft mudstone formation is observed from the depth 58.7 meters at Site A according to the boring log. A stiff sandy gravel layer appears at the depth 43.3 meters; the N-values of the gravel layer exceed 50 at Site B. No rock formation

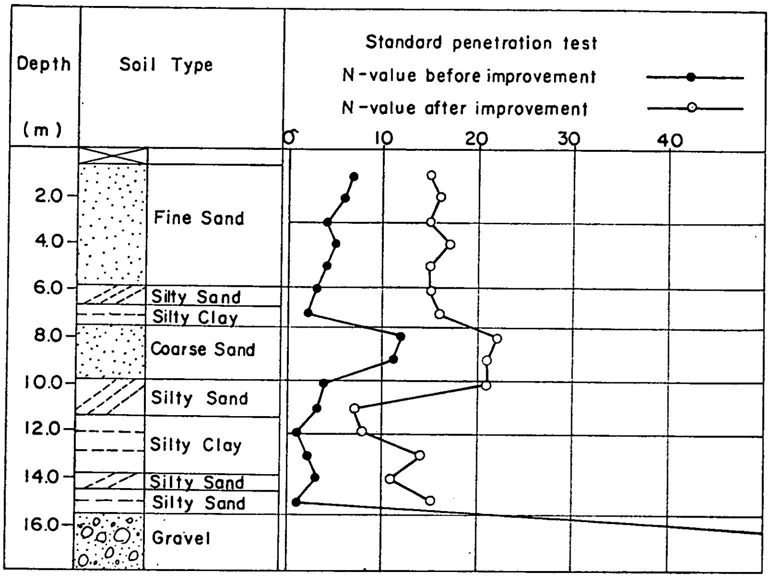

Fig. 31 Boring Logs Before and After the Compation at the Oil Tank Yard

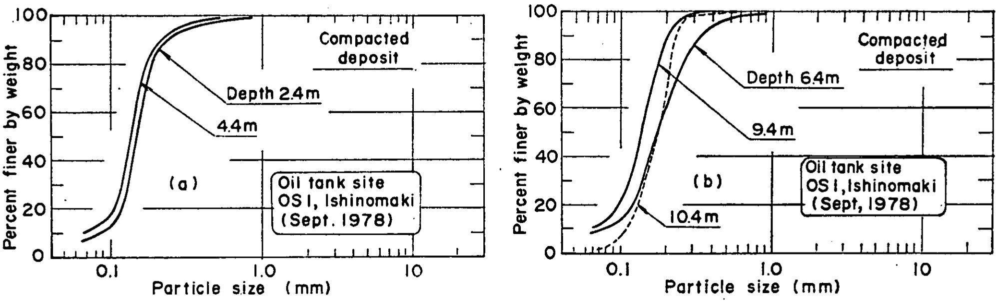

Fig. 32 Grain Size Accumulation Curve of Sands at the Compacted Site, After ISHIHARA et al[9].

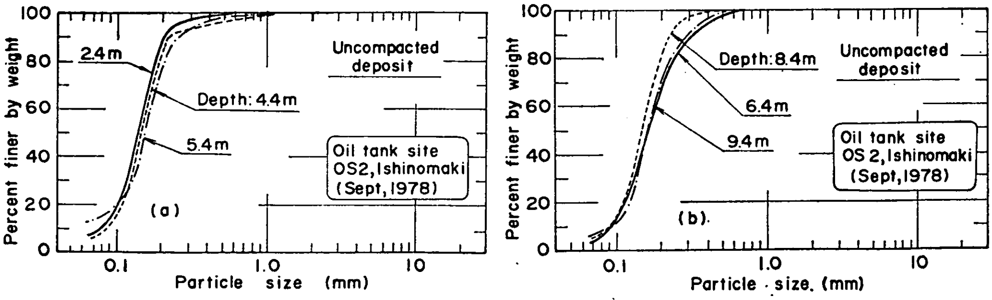

Fig. 33 Grain Size Accumulation Curve of Sands at the Uncompacted Site After ISHIHARA et al[9].

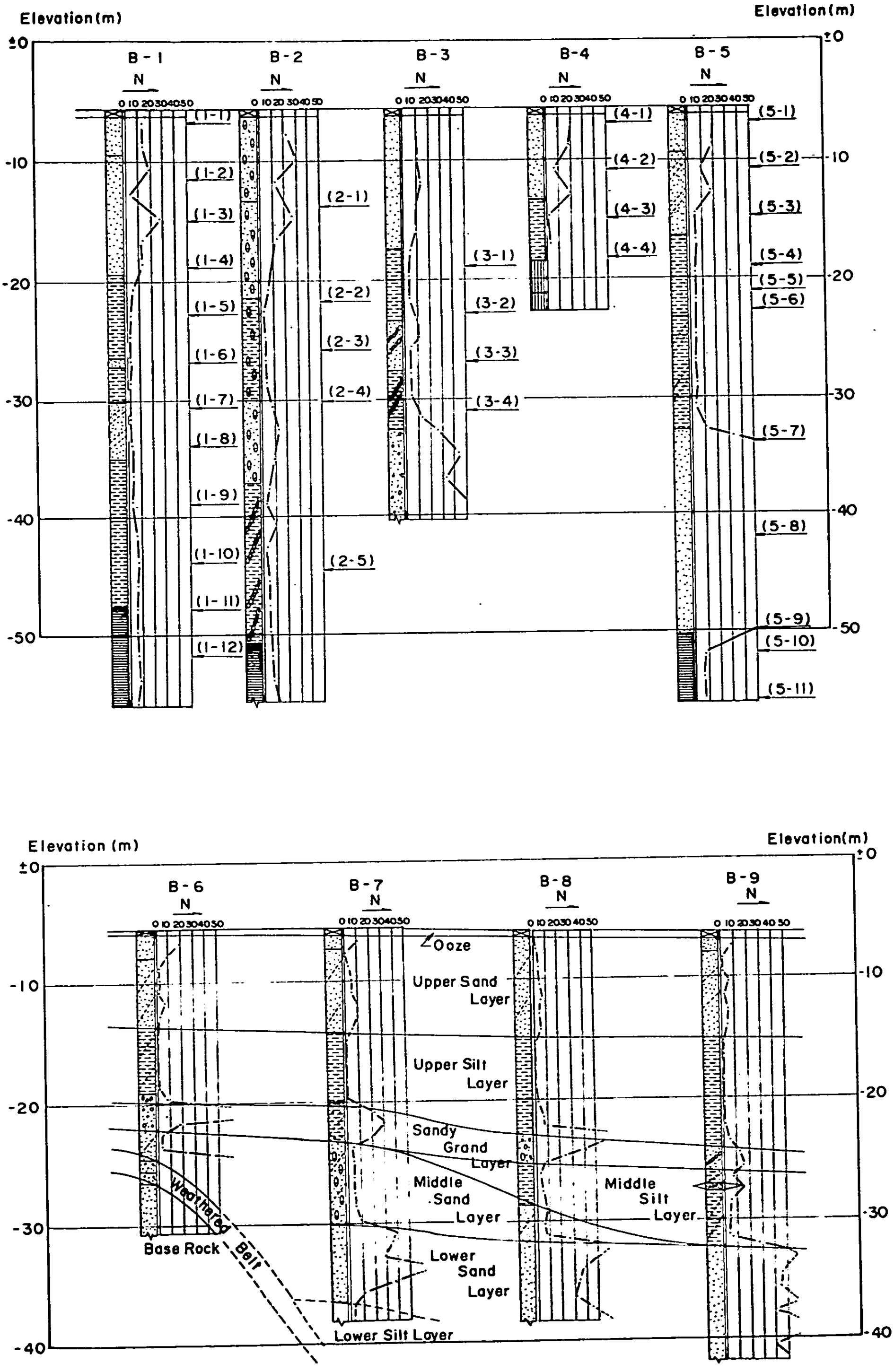

Fig. 34 Boring Logs at Ishinomaki Fishery Port (Number indicates the location in **Fig. 29**)

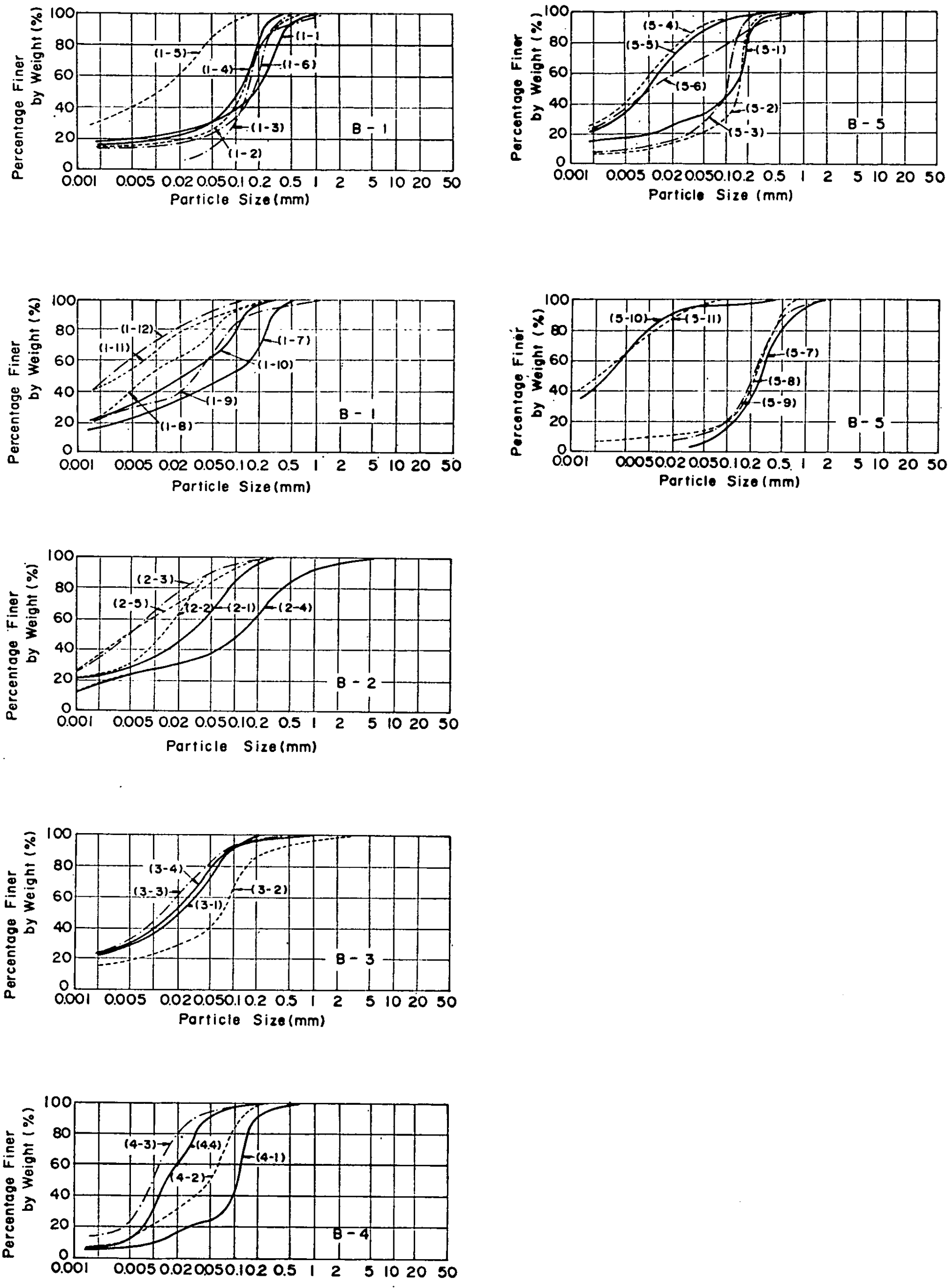

Fig. 35 Grain Size Accumulation Curves of Soils at Ishinomaki Fishery Port (Number indicates the sand layers shown in **Fig. 34**)

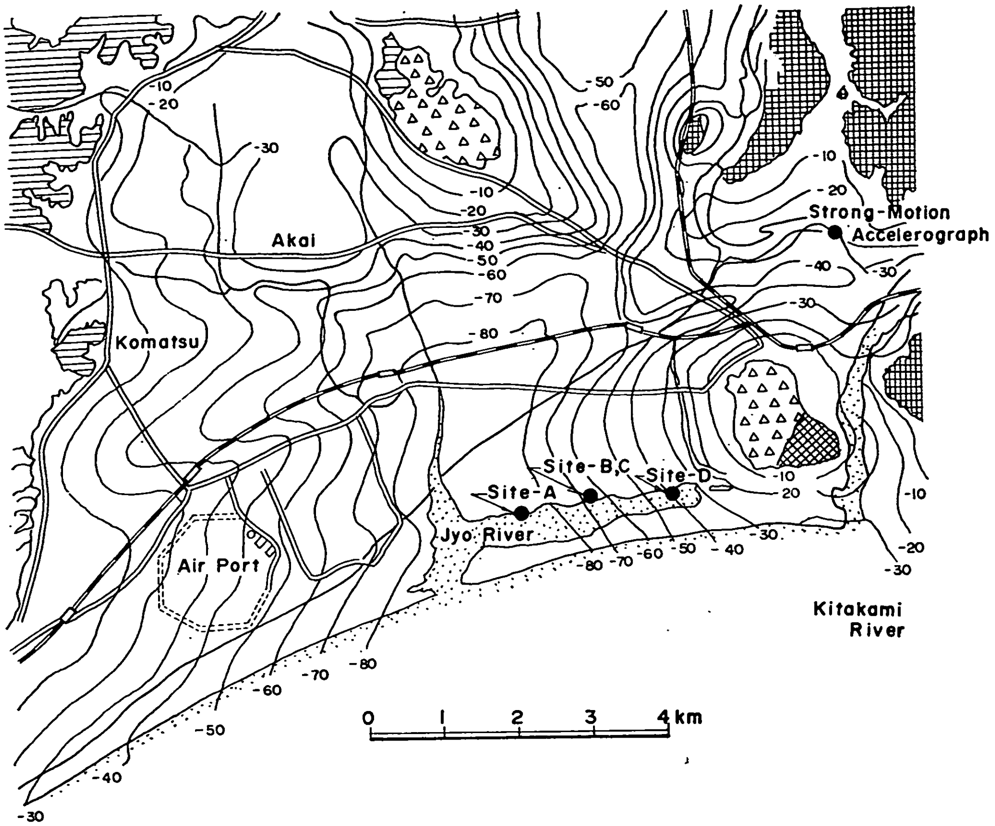

Fig. 36 Depth of Base Rock at Ishinomaki Area, After MINISTRY of CONSTRUCTION et al[10].

is found in the boring data down to the depth 45.2 meters. Base rock formation at Site C is considered the same as that at Site B, because both sites are located near each other. Rock formation is observed from the depth 38.8 meters at Site D according to the boring log. At Site E and Site F, a stiff gravel layer appears from the depth 17.4 meters. However, boring logs around this area shows great variations in the depth of base formation.

According to the reference 10), the depth of base rock formation varies as shown in Fig. 36. Base rock mainly consists of Tertiary and Mesozoic rock[10]. In general, depths of base rock formation indicated by the boring logs are harmonious with those shown in Fig. 36, but the depths at Site A and Site B greatly differ from those shown in Fig. 36. It is believed that the base rock at Sites A and B is formed at the depth indicated in Fig. 36 and a very hard deposit layer exists on top of the base rock up to the depth indicated by the boring logs.

(2) Underground Water Level at the Time of the Earthquake

Information on the underground water level is very important for the analysis of liquefaction. The underground water level was not measured at any place near the study sites at the time of the earthquake. However, a tidal gauge was in operation at the time of the earthquake. The location of the tidal gauge is shown in Fig. 37. The record is shown in Fig. 38. Tidal level and ground water level

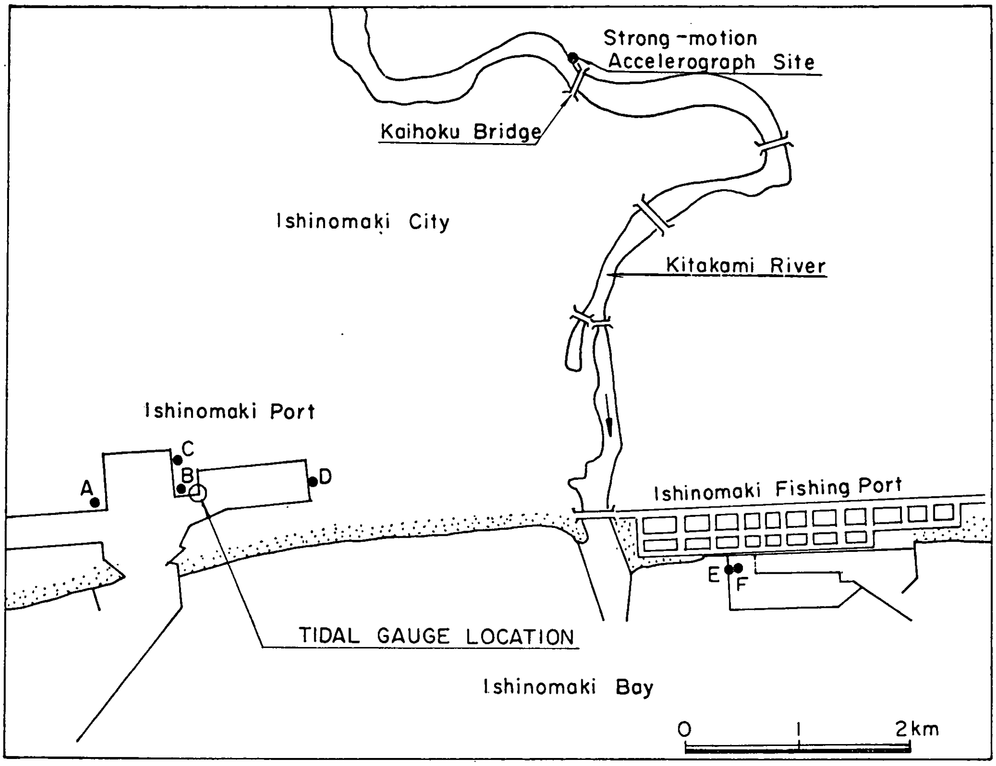

Fig. 37 Location of Tidal Gauge

are not the same. However, the tidal level at the time of the earthquake, i.e., 1.45 meters (K.P.), was used in the present analysis as an estimated level of the ground water.

3.7 Summary of the Sites under Study

Figure 39 is a compilation of the ground formation of Sites A to F, which have been selected for the present study. Most of the N-values and the q_u-values shown in Fig. 39 were measured before the earthquake. Exceptions are as follows:

(1) The q_u-values of clayey layers deeper than 40 meters at Sites A, B, and C were estimated from those of clayey layers from 15 meters to 30 meters deep by the linear extrapolation method.

(2) The N-values and q_u-values at Site B were measured after the earthquake. These values are considered representative of pre-earthquake conditions, because the N-values at Site D measured before the earthquake were not quite different from those measured after the earthquake.

The soil layers at Ishinomaki Port are classified into four types according to their grain size distribution; namely, upper sand, lower sand, silty sand, and clay as shown in Fig. 40. The upper sand layers are located from the second to the third layers from the ground surface in Fig. 39. The variation in grain size distribution curves within one type of soil is indicated by the hatched area in Fig. 40 for the upper sand layer. Soil layers of the other types have similar

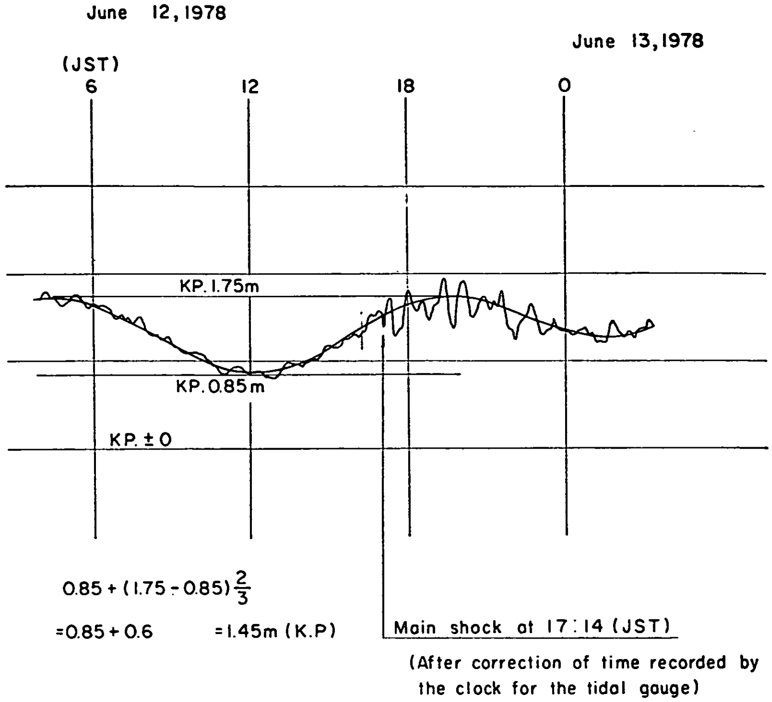

Tidal Gauge : Suiken 62 Type Self Recording Tidal Gauge
Location of Tidal Gauge : At Sea Side Corner of Hiyori Pier close to site-8
Tidal Level according to Ishinomaki Port Office : KP.+1.4m
KP = Standard Level for Port Construction = T.P. - 0.8745m

Fig. 38 Record of Tidal Level at the Time of the Earthquake

variations.

Figure 41 shows the N-values of upper sand layers more clearly[11]. From this figure, it is clear that liquefied sites, in general, have smaller N-values than non-liquefied sites.

4. Modelling Liquefaction Strength of Sands

4.1 Model for Pore Water Pressure Generation

Characteristics of the generation of pore water pressure for saturated sands, for the present study, are analyzed by the model developed in the reference 12). The basic concept of this model can be explained as follows. Volume change of saturated sands is partly recoverable (elastic) and partly irrecoverable (plastic). The saturated sands have potential plastic volume decrease due to rearrangement of sand particles when it is subjected to cyclic loadings. Under undrained condition, saturated sands have no volume change and, therefore, excess pore water pressure has to be generated in accordance with its compressibility.

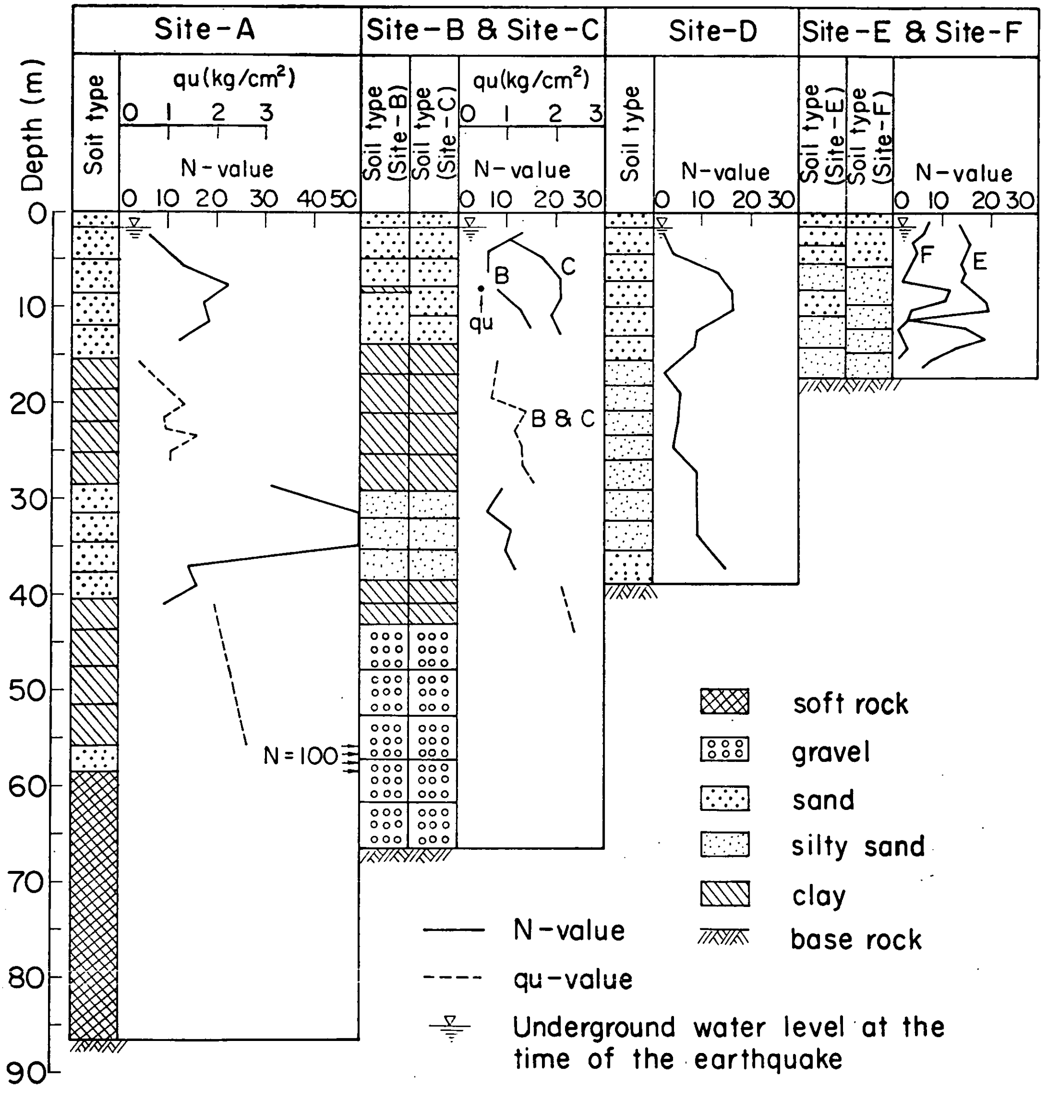

Fig. 39 Ground Formations of the Sites under Study

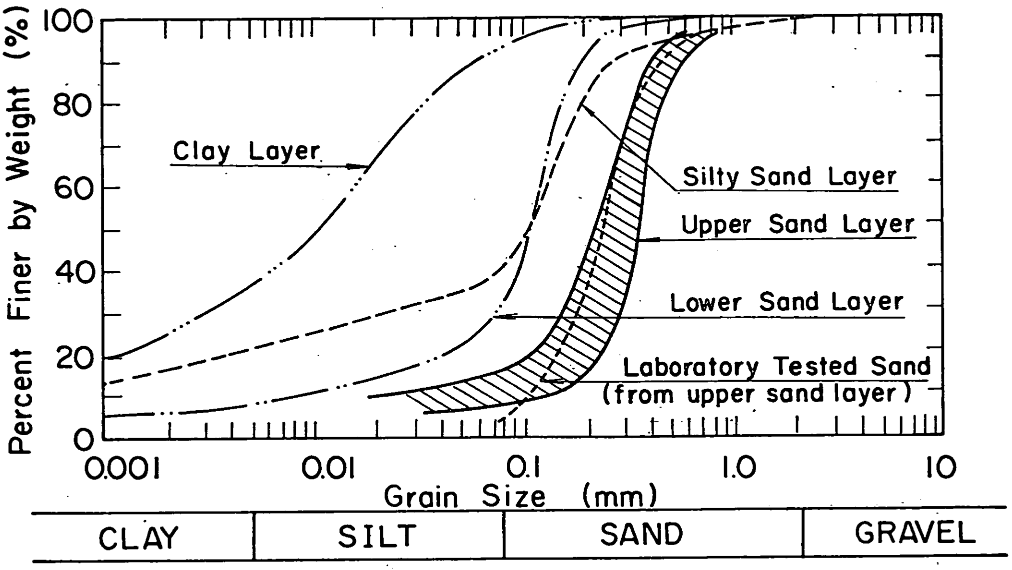

Fig. 40 Grain Size Accumulation Curves of Soils at the Sites under Study

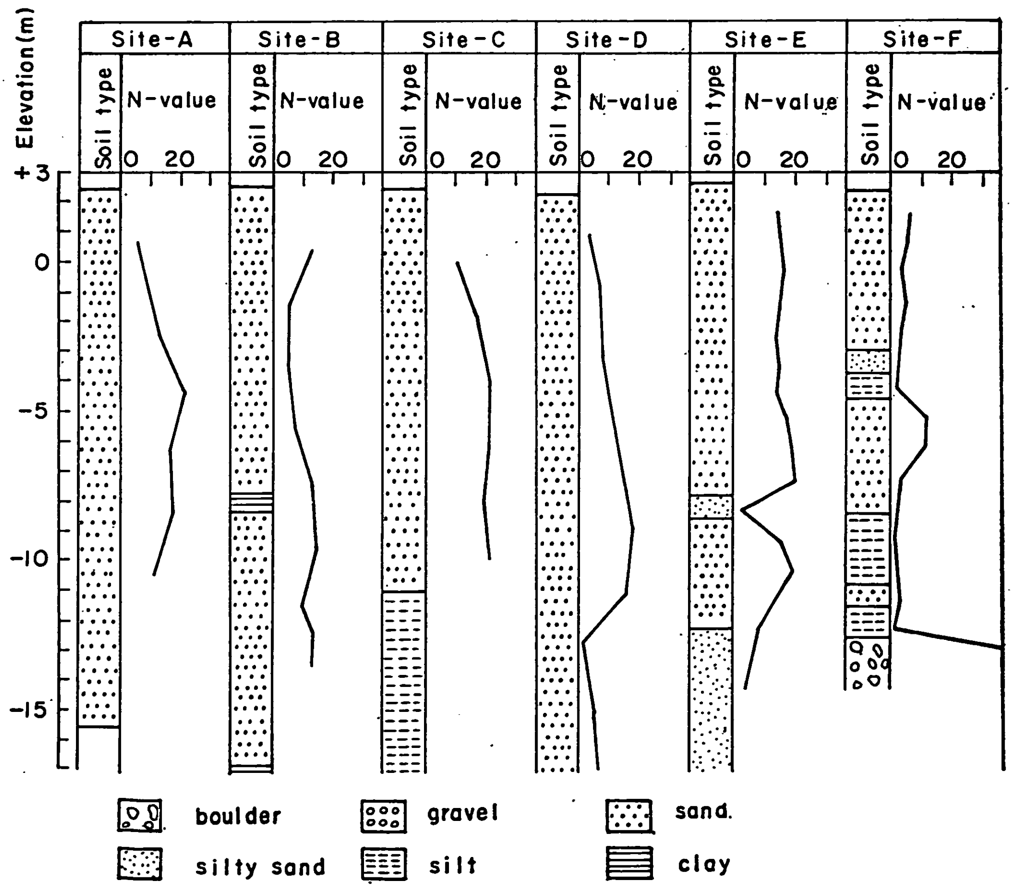

Fig. 41 Comparison of N-values at Upper Sand Layers

Formulation of this concept is, in essence, expressed by the following equation for saturated sands.

$$\Delta u=\bar{E}_r\cdot\Delta\epsilon_{vd} \tag{1}$$

where Δu: increment of excess pore water pressure for half cycle of loading
$\Delta\epsilon_{vd}$: increment of volumetric strain corresponding to the decrease in volume during half cycle of loading under drained condition
$\bar{E}_r$: rebound modulus; $E_r=-\frac{\partial\sigma_v'}{\partial\epsilon_{vd}}$, $\bar{E}_r$ is an average of E_r over half cycle. (σ_v': effective vertical stress.)

In the reference 12), $\Delta\epsilon_{vd}$ and $\bar{E}_r$ are empirically formulated as follows.

$$\Delta\epsilon_{vd}=c_1(\gamma-c_2\epsilon_{vd})+\frac{c_3\epsilon_{vd}^2}{\gamma+c_4\epsilon_{vd}} \tag{2}$$

$$\bar{E}_r=\frac{(\sigma_v')^{1-m}}{mk_2(\sigma_{v0}')^{n-m}} \tag{3}$$

where γ: shear strain amplitude for half cycle
σ_{v0}': initial vertical effective stress
σ_v': present vertical effective stress

For the present study, a better fit to the laboratory test data was achieved by using the following equation.

$$\Delta\epsilon_{vd}=V_1\gamma\ \ln\left(1+e^{-V_2\frac{\epsilon_{vd}}{\gamma}}\right) \tag{2$'$}$$

The test results and model fitting will be explained later.

Equation (1) can be integrated using Eq. (3) giving the following simple form for the excess pore water pressure, using the initial condition $u=0$ when $\epsilon_{vd}=0$.

$$\begin{cases}\dfrac{u}{\sigma_{v0}'}=1-\left(1-\dfrac{\epsilon_{vd}}{\epsilon_{vd0}}\right)^{\frac{1}{m}} & (4)\\ \text{and } \epsilon_{vd0}=k_2(\sigma_{v0}')^n & (5)\end{cases}$$

where ϵ_{vd}: volumetric strain corresponding to the decrease in volume under drained condition.

The effect of parameter m ($0<m<1$) on excess pore water pressure generation is illustrated in Fig. 42.

Equation (2)′ has the following characteristics.

(i) Suppose that sand is tested by cyclic loading in the constant strain amplitude test. The tests are carried out at several values of strain amplitudes. Then, at any specified half cycle, increment of volumetric strain $\Delta\epsilon_{vd}$ is proportional to shear strain amplitude γ, and so is the volumetric strain ϵ_{vd}.

It is easily proven by dividing both sides of equation (2)′ by γ.

(ii) Suppose again that sand is tested by the constant strain test. Then, if $V_1>0$ and $V_2>0$, increment of volumetric strain $\Delta\epsilon_{vd}$ is always decreasing down to zero as the number of cycles of loadings increases. $V_1>0$, and $V_2>0$ is the usual cases.

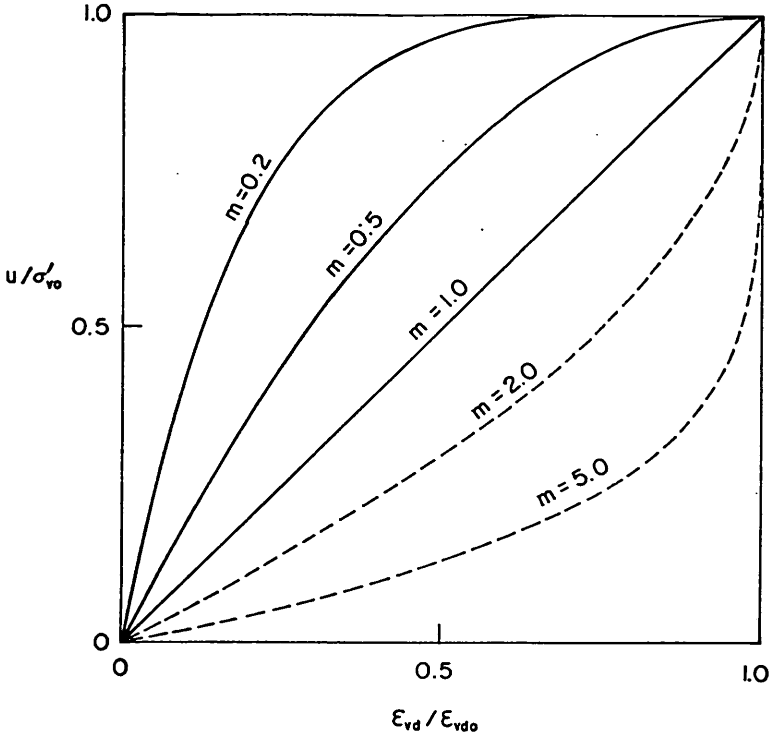

Fig. 42 Relation between Excess Pore Water Pressure u and Recoverable Volumetric Strain ϵ_{vd} in Normalized form

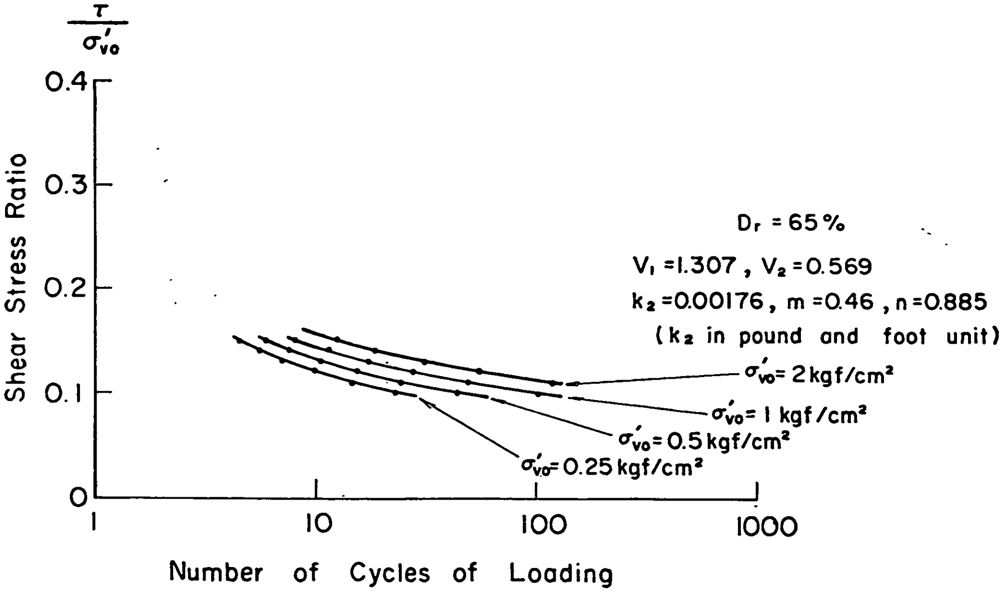

Fig. 43 Simulated Liquefaction Strength Curves under the Assumption that Volumetric Strain is Independent of Vertical Confinining Pressure

It is also easily proven by carrying out partial differential of the right hand side of equation (2)′ for ϵ_{vd}.

Examples of these characteristics will be shown in a later section.

4.2 Influence of Vertical Confining Pressure on Liquefaction Strength

In practice, the parameters for the effective stress model are often determined for each depth at which samples are taken and for which laboratory liquefaction strength (liquefaction resistance) is available. In the present study, direct information is available mainly for layers near the surface and the model parameters so determined are also used at depth with appropriate corrections for relative density inferred from N-value of standard penetration test.

Liquefaction strength computed by the effective stress model is usually dependent on the level of vertical confining pressure (see Fig. 43). How liquefaction strength depends on the level of confining stress is still an unresolved problem. However in the present study, the model parameters were adjusted as described in this section to ensure that the liquefaction strength specified in terms of shear stress ratio τ/σ_{v0}' does not depend on the value of vertical confining pressure σ_{v0}'. The readers who are interested mainly in getting general ideas on the applicability of the effective stress model can skip the rest of this section and continue to follow the present report from section 4.3. Throughout the following discussion, relative density of sands is considered to be fixed.

(1) Equations for Expressing the Behavior of Sands under the Constant Stress Test

Liquefaction strength is measured by a cyclic loading test with shear stress of constant magnitude. Pore water pressure generation by the model under study²⁾ is as follows. For each half cycle of shear deformation, increment of pore water pressure is calculated. Each half cycle consists of two parts; one is a part where absolute value of shear strain is increasing and the other is a part where absolute value of shear strain is decreasing. During the former part, no pore water pressure is generated and during the latter part pore water pressure is generated in accordance with shear strain amplitude and rebound modulus at the end of the former part. Figure 44 is a schematic view of the pore water pressure generation described above.

Stress-strain relation is expressed by a model so-called Hystretic Hardin-Drnevich Model²⁾. This model is a combination of a hyperbolic backbone curve and the Masing rule as illustrated in Fig. 45. The Masing rule consists of the following two rules;

(i) If reversal occurs on the normalized stress-strain plane as illustrated in Fig. 45, follow a curve which is obtained by magnifying the backbone curve twice and transpose the origin to the reversal point.

(ii) If a present point is going on to the previous reversal point, reduce to follow a curve which was previously followed and go through the previous reversal point.

The behaviour of a sand specimen under the constant stress cyclic loading test is expressed by a set of the following nine equations (6) to (14) by the model.

a) Softening and Reduction in Shear Strength

Softening and reduction in shear strength are expressed by

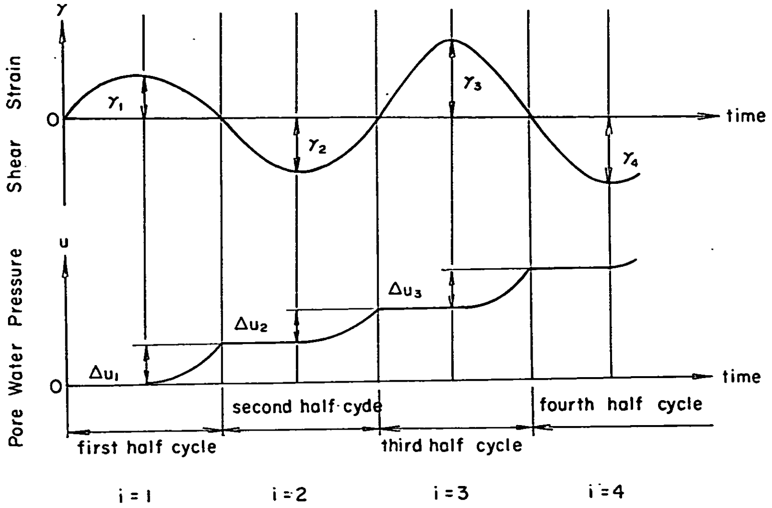

Fig. 44 A Schematic View of Pore Water Pressure Generation

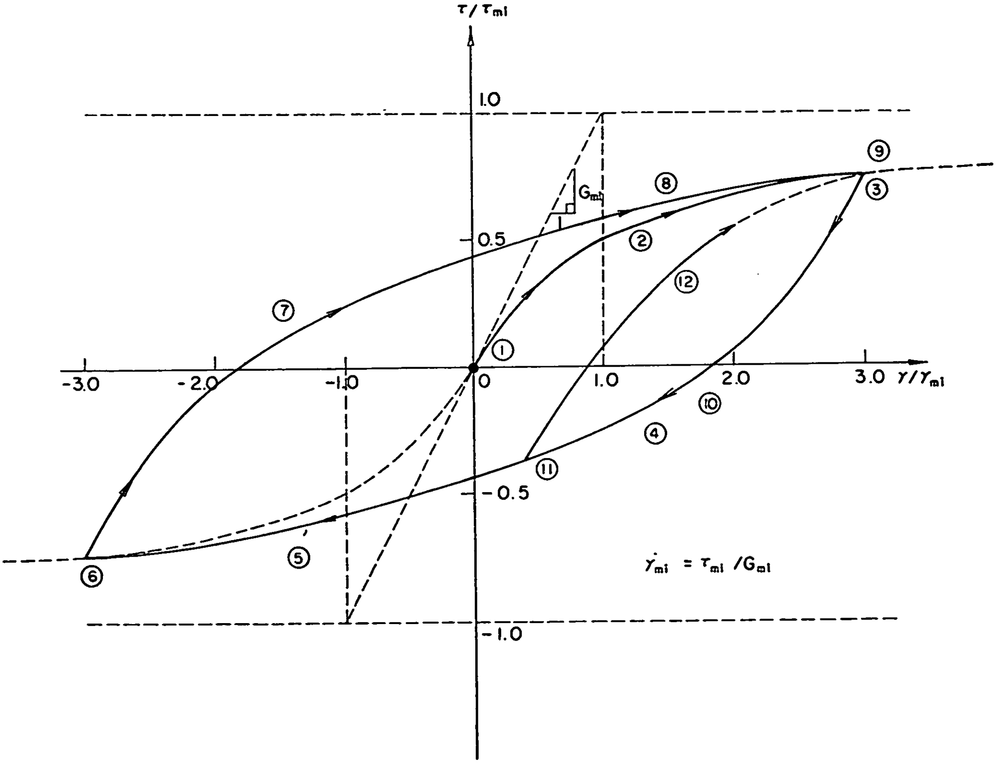

Fig. 45 Illustration of Stress-Strain Relation in Normalized Form (number and arrows indicate an example path)

$$G_{mi}=G_{m0}\sqrt{\frac{\sigma_{vi}'}{\sigma_{v0}'}} \tag{6}$$

$$\tau_{mi}=\tau_{m0}\cdot\frac{\sigma_{vi}'}{\sigma_{v0}'} \tag{7}$$

where G_{m0}: Shear modulus at small strain level before cyclic loading
G_{mi}: Shear modulus at small strain level at the beginning of ith half cycle
τ_{m0}: Shear strength before cyclic loading
τ_{mi}: Shear strength at the beginning of ith half cycle
σ_{v0}': Vertical effective stress before cyclic loading
σ_{vi}': Vertical effective stress at the beginning of i th half cycle

b) Constant Stress Ratio Condition

The sand specimen is considered to be tested under constant stress ratio at several σ_{v0}'; i.e.,

$$\frac{\tau}{\sigma_{v0}'}=\text{const} \tag{8}$$

where τ: Shear stress amplitude

c) Stress-Strain Relation

Because pore water pressure at the end of each half cycle is always increasing during the undrained cyclic loading test, shear stress amplitude normalized by τ_{mi} is always increasing. Therefore, the relation between shear stress amplitude and shear strain amplitude is expressed by the equation of the backbone curve; i.e.,

$$\tau=G_{mi}\gamma_i/\left(1+\frac{G_{mi}}{\tau_{mi}}\gamma_i\right) \tag{9}$$

where γ_i: shear strain amplitude at i th half cycle

d) Generation of Volumetric Strain and Pore Water Pressure

Pore water pressure is related to volumetric strain by (equation (1))

$$\Delta u_i=\bar{E}_{ri}\cdot\Delta\epsilon_{vdi} \tag{10}$$

with rebound modulus (equation (3)):

$$\bar{E}_{ri}=\frac{1}{mk_2}\cdot\left(\frac{\sigma_{vi}'}{\sigma_{v0}'}\right)^{1-m}\cdot(\sigma_{v0}')^{1-n} \tag{11}$$

where u_i: increment of pore water pressure during i th half cycle
$\Delta\epsilon_{vdi}$: increment of volumetric strain during i th half cycle
$\bar{E}_{vi}$: Rebound modulus at the beginning of i th half cycle
k_2, m, and n: Rebound modulus parameters

Volumetric strain, of which increment appeared in Eq. (10), is generated by the following empirical equation, which corresponds to Eq. (2)′.

$$\Delta\epsilon_{vdi}=V_1\cdot\gamma_i\cdot\ln(1+e^{-V_2\epsilon_{vdi}/\gamma_i}) \tag{12}$$

where $\epsilon_{vdi}=\sum_{k=1}^{i-1}\Delta\epsilon_{vdk}$ (for $i\geqq 2$) $=0$ (for $i=1$)

ϵ_{vdi}: Volumetric strain at the beginning of i th half cycle
V_1 and V_2: Parameters for volumetric strain generation

V_1, V_2, k_2, m, and n in Eqs. (11) and (12) are the parameters for pore water pressure generation.

e) Shear Moduli at Small Strain Level and Shear Strength

Shear moduli at small strain level and shear strength are determined by the following equations for this study.

$$G_{m0} \propto \sqrt{\sigma_{v0}'} \tag{13}$$

$$\tau_{m0} \propto \sigma_{v0}' \tag{14}$$

where $\propto$: "$A \propto B$" means "A/B is independent of σ_{v0}'". This definintion of "$\propto$" is not commonly used but it will be effective throughout this section.

(2) Derivation of Sufficient Conditions for Independency of Liquefaction Strength against σ_{v0}'

The problem to solve is to derive a pair of equation of σ_{v0}' for V_1 and V_2 in Eq. (12) in order to acquire independency of liquefaction strength against σ_{v0}'. One expression of independent liquefaction strength against σ_{v0}' is that the number of cycles of loading to get liquefaction is independent of σ_{v0}' for any tests of a fixed τ/σ_{v0}'.

a) One of Sufficient Conditions for the Independency of Liquefaction Strength against σ_{v0}'

One of sufficient conditions for the independent liquefaction strength is that the rate of pore water pressure generation $\frac{\Delta u_i}{\sigma_{v0}'}$ is independent of σ_{v0}'; i.e.,

$$\Delta u_i \propto \sigma_{v0}' \tag{15}$$

Let us assume Eq. (15) until a pair of equations of σ_{v0}' for V_1 and V_2 is obtained, i.e., Eq. (26) and (30), for the independency of liquefaction strength against σ_{v0}'.

Relation of pore water pressure and vertical effective stress is

$$\left.\begin{aligned} \sigma_{vi}' &= \sigma_{v0}' - \sum_{k=1}^{i-1} \Delta u_k && (\text{for } i \geqq 2) \\ &= \sigma_{v0}' && (\text{for } i=1) \end{aligned}\right\} \tag{16}$$

From Eq. (15) and (16),

$$\sigma_{vi} \propto \sigma_{v0}' \tag{17}$$

Namely, $\frac{\sigma_{vi}}{\sigma_{v0}'}$ is independent of σ_{v0}'.

b) Derivation of $\gamma_i \propto \sqrt{\sigma_{v0}'}$

At first, we are going to show that $\gamma_i \propto \sqrt{\sigma_{v0}'}$.

By solving Eq. (9) for γ_i,

$$\gamma_i = \tau \Big/ \left\{ G_{mi}\left(1 - \frac{\tau}{\tau_{mi}}\right) \right\} \tag{18}$$

From Eqs. (6), (13), and (17),

$$G_{mi} \propto \sqrt{\sigma_{v0}'} \tag{19}$$

Similarly, from Eqs. (7), (14), and (17),

$$\tau_{mi} \propto \sigma_{v0}' \tag{20}$$

From Eqs. (8) and (19),

$$\tau/G_{mi} \propto \sqrt{\sigma_{v0}'} \tag{21}$$

From Eqs. (8) and (20), τ/τ_{mi} is independent of σ_{v0}'; i.e.,

$$\tau \propto \tau_{mi} \tag{22}$$

Therefore, substitute Eqs. (21) and (22) into (18),

$$\gamma_i \propto \sqrt{\sigma_{v0}'} \tag{23}$$

c) Equations of V_1 and V_2 for Independency of Liquefaction Strength against σ_{v0}'

Derivation of equations of σ_{v0}' for V_1 and V_2 are as follows.

From Eqs. (11) and (17),

$$\bar{E}_{ri} \propto (\sigma_{v0}')^{1-n} \tag{24}$$

From Eqs. (10), (12), and (24),

$$\frac{\Delta u_i}{\sigma_{v0}'} \propto (\sigma_{v0}')^{-n} \cdot V_1 \cdot \gamma_i \cdot \ln(1+e^{-V_2 \epsilon_{vdi}/\gamma_i}) \tag{25}$$

From Eq. (15), the right hand side of Eq. (25) must be independent of σ_{v0}'. A sufficient condition for this is that both of $(\sigma_{v0}')^{-n} \cdot V_1 \cdot \gamma_i$ and $V_2 \cdot \epsilon_{vdi}/\gamma_i$ are independent of σ_{v0}'. Let us assume this condition.

(i) Equation for V_1

Then, from Eq. (23) and the condition that $(\sigma_{v0}')^{-n} \cdot V_1 \cdot \gamma_i$ is independent of σ_{v0}', $V_1 \cdot (\sigma_{v0}')^{0.5-n}$ is independent of σ_{v0}': i.e.,

$$V_1 \propto (\sigma_{v0}')^{n-0.5} \tag{26}$$

(ii) Equation for V_2

From Eq. (10) and (24),

$$\frac{\Delta u_i}{\sigma_{v0}'} = \frac{\bar{E}_{ri}}{\sigma_{v0}'} \cdot \Delta\epsilon_{vdi} \propto (\sigma_{v0}')^{-n} \cdot \Delta\epsilon_{vdi} \tag{27}$$

From Eqs. (15) and (27),

$$\Delta\epsilon_{vdi} \propto (\sigma_{v0}')^{n} \tag{28}$$

$$\therefore \quad \epsilon_{vdi} \propto (\sigma_{v0}')^{n} \tag{29}$$

From Eqs. (23) and (29), and the condition that $V_2 \cdot \epsilon_{vdi}/\gamma_i$ is independent of σ_{v0}', $V_2 \cdot (\sigma_{v0}')^{n-0.5}$ is independent of σ_{v0}', i.e.,

$$V_2 \propto (\sigma_{v0}')^{0.5-n} \tag{30}$$

Thus, equations for V_1 and V_2 were obtained.

(3) Proof of the Sufficient Conditions

For the derivation of equations (26) and (30), equation (15) was assumed.

Therefore, the discussion in the previous subsection is not a complete proof of the fact that equations (26) and (30) are sufficient conditions for independency of liquefaction strength against σ_{v0}'. In order to prove this fact, we are going to prove that equations (26) and (30) are sufficient conditions for equation (15) in this subsection.

Suppose conditions of Eqs. (26) and (30) are given for basic equations (6) to (14).

a) Initial Half Cycle ($i=1$)

Because $\sigma_{vi}'=\sigma_{v0}'$, Eqs. (6) and (7) are reduced to

$$G_{m1}=G_{m0} \tag{6$'$}$$

$$\tau_{m1}=\tau_{m0} \tag{7$'$}$$

Therefore, derivation similar to Eqs. (18) to (22) is possible and Eq. (23) is derived for $i=1$. Eq. (24) is also derived from Eq. (11) for $i=1$ because $\sigma_{v1}'=\sigma_{v0}'$, and therefore, Eq. (25) is also derived for $i=1$. Because $\epsilon_{vdi}=0$ and Eq. (23) is true for $i=1$, Eqs. (26) and (30) are sufficient conditions for both of $(\sigma_{v0}')^{-n}\cdot V_1\cdot\gamma_i$ and $V_2\cdot\epsilon_{vdi}/\gamma_i$ are independent of σ_{v0} for $i=1$. Therefore, from Eq. (25),

$$\Delta u_1 \propto \sigma_{v0}' \tag{15$'$}$$

b) Second Half Cycle ($i=2$)

From Eqs. (15)$'$ and (16), Eq. (17) is derived for $i=2$. Therefore, Eqs. (18) to (22) can be followed and Eq. (23) is derived for $i=2$. Eq. (24) is also derived for $i=2$ and, therefore, Eq. (25) is derived for $i=2$. Because Eq. (24) was derived for $i=1$ as was described at the initial half cycle, Eq. (27) is also derived for $i=1$. From Eqs. (15)$'$ and (27), Eq. (28) is derived for $i=1$. Because $\epsilon_{vd2}=\Delta\epsilon_{vd1}$, Eq. (29) is derived for $i=2$. Because of Eqs. (23) and (29) for $i=2$, Eqs. (26) and (30) are sufficient conditions for both of $(\sigma_{v0}')^{-n}\cdot V_1\cdot\gamma_i$ and $V_2\cdot\epsilon_{vdi}/\gamma_i$ are independent of σ_{v0}' for $i=2$. Therefore, from Eq. (25) for $i=2$,

$$\Delta u_2 \propto \sigma_{v0}' \tag{15$''$}$$

c) Following Cycles ($i\geqq 3$)

The following cycles are similar to the second cycle. Therefore, Eqs. (26) and (30) are sufficient conditions for independency of liquefaction strength for the model expressed by Eqs. (6) to (14). They are also sufficient conditions for Eqs. (15), (23), and (29). Equations (23) and (29) are also important results of this section for understanding the model under the influence of σ_{v0}'.

d) Conclusion of the Subsection

From the discussion described in this subsection, the following conclusion was finally proved; namely,

If $V_1/(\sigma_{v0}')^{n-0.5}$ and $V_2/(\sigma_{v0}')^{0.5-n}$ are independent of σ_{v0}', then liquefaction strength is independent of σ_{v0}'.

In other words, liquefaction strength is independent of σ_{v0}', if

$$V_1=V_1^*\cdot\left(\frac{\sigma_{v0}'}{\sigma_{v0e}'}\right)^{n-0.5} \tag{31}$$

$$V_2=V_2^*\cdot\left(\frac{\sigma_{v0}'}{\sigma_{v0e}'}\right)^{0.5-n} \tag{32}$$

where V_1^* and V_2^* are the values of V_1 and V_2 at vertical confining pressure σ_{v0e}' and n is one of rebound modulus constants.

(4) Consistency with the Experimental Results

Equation (12) indicates that, if V_1 and V_2 are varied in accordance with σ_{v0}', volumetric strain becomes dependent on σ_{v0}'. Therefore, it is impossible to get independency for both volumetric strain and liquefaction strength against σ_{v0}' at the same time as long as Eqs. (6) to (12) together with Eqs. (13) and (14) are concerned. This conclusion disagrees with experimental results which indicate independency of both volumetric strain and liquefaction strength against σ_{v0}'.

It is easy to show, however, that, if G_{m0} is determined by

$$G_{m0} \propto (\sigma_{v0}')^{1-n} \tag{33}$$

instead of equation (13), then not only liquefaction strength but also volumetric strain becomes independent of σ_{v0}'. For this independency, Eq. (6) is not necessarily be retained as it is, but it can be expressed as

$$G_{mt}=f\left(\frac{\sigma_{vt}'}{\sigma_{v0}'}\right)\cdot G_{m0} \tag{34}$$

where f is an arbitrary function.

For the present study, however, Eqs. (6) and (13) are used because they were directly obtained from experimental results. As a result, dependency of volumetric strain on σ_{v0}' at a constant strain test was left as inconsistency with the experimental results. Degree of the inconsistency will be evaluated in the future in comparison with reliability of laboratory test data.

4.3 Determination of Parameters for Pore Water Pressure Generation

(1) Simple Shear Apparatus, Tested Sands, and Liquefaction Strength

The simple shear apparatus at the University of British Columbia[13)] was used for the tests of sands in Ishinomaki Port. Figure 46 shows a section of this apparatus. Dimensions of sand samples are 5.08 cm × 5.08 cm × 2.86 cm, where 2.86 cm is the height.

Tested sands were taken from within one meter depth of the quay surface at Shiomi (−4.5 m) Wharf. The sampling location is shown in Fig. 23.

The physical properties of the sands were tested in the Port and Harbour Research Institute and the results are shown in Fig. 47 and Table 1. Figure 48 is a grain size accumulation curve of the sand tested at the University of British Columbia. These sands contain less than 5% fines but sandy soils at Ishinomaki Port generally contains 5 to 30% fines as was explained in the previous chapter. The difference in fines content may result in some underestimation of liquefaction strength of some layers in the effective stress model.

Relative density of tested sand specimens were fixed at 65% for all tests discussed in this section. Undrained cyclic loading tests of constant cyclic shear stress were carried out for several shear stress amplitudes. Vertical confining pressure was 2.0 kgf/cm² for all tests. The test results are shown in Fig. 49. These results are later used to check the appropriateness of the parameters of the effective stress model.

(2) Parameters for Tested Sands

Drained cyclic loading test at various levels of constant cyclic shear strain were conducted to determine the volumetric strain constants V_1 and V_2 in equation (2'). The test data are shown by the solid curves in Fig. 50 and the predicted values are shown by the broken curves. $V_1=1.307$ and $V_2=0.569$ were obtained.

Dynamic rebound tests were conducted to determine the rebound modulus parameters. Comparison between experimental data (open points) and predictions by equation (3) are very good as shown on Fig. 51. The parameters were determined to be $m=0.46$, $n=0.895$, and $k_2=0.00176$, where k_2 is expressed in foot, pound,

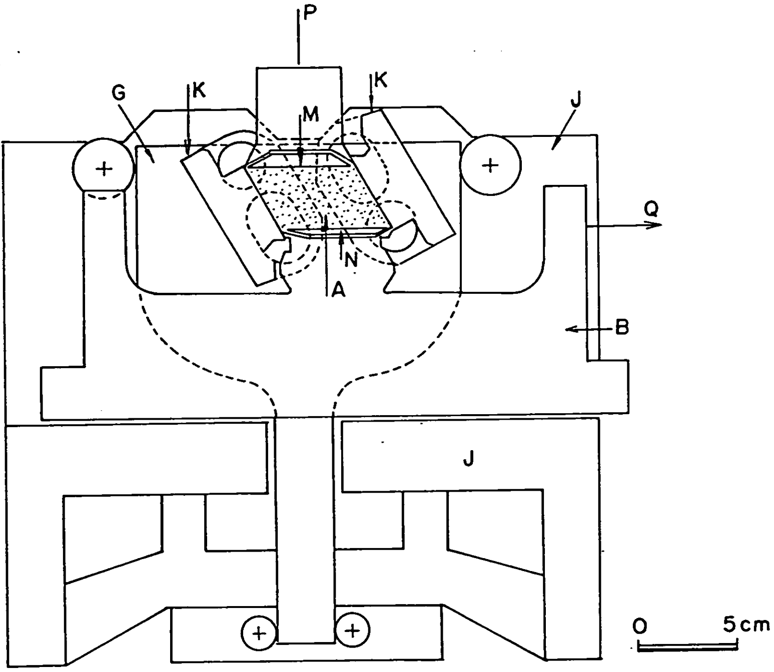

Fig. 46 Section of Simple Shear Apparatus, After FINN et al.[13)]

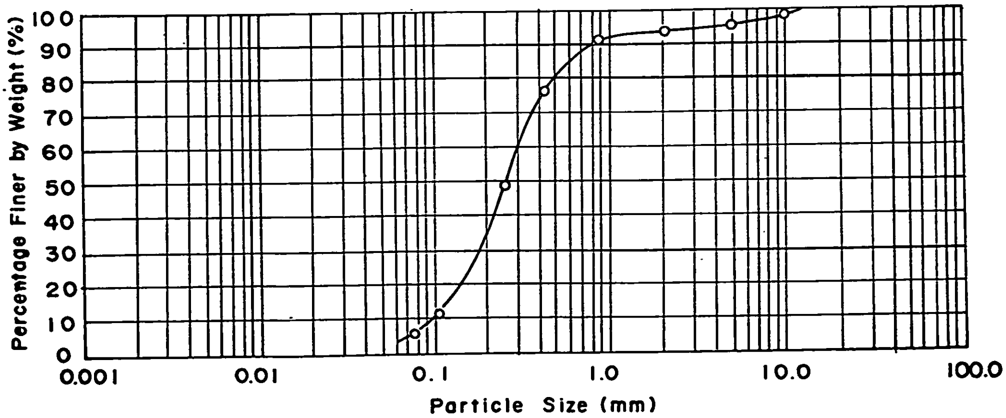

Fig. 47 Grain Size Accumulation Curve of Sand from Shiomi (−4.5 m) Wharf Tested at PHRI

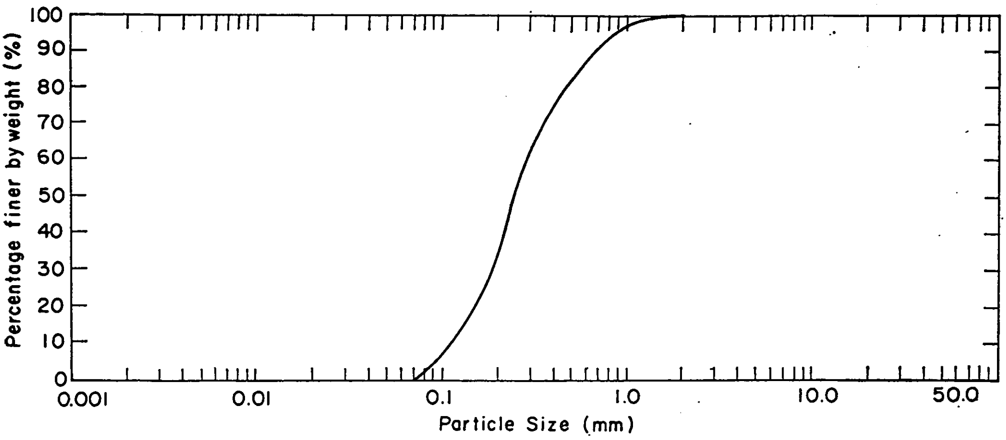

Fig. 48 Grain Size Accumulation Curve of Sand from Shiomi (−4.5 m) Wharf Tested at UBC

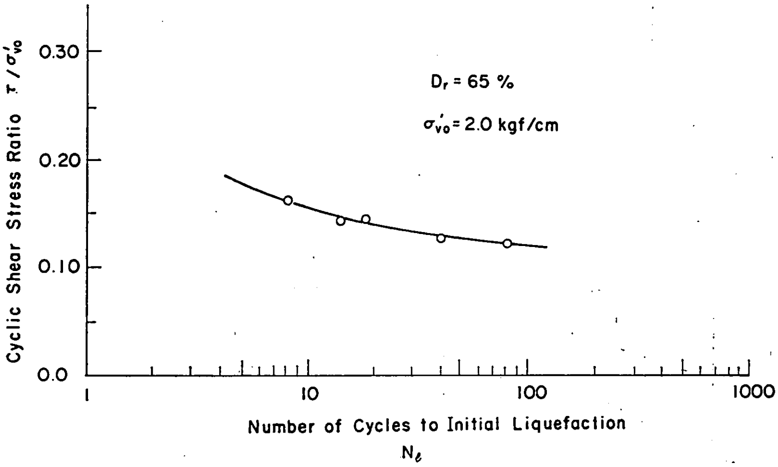

Fig. 49 Liquefaction Strength

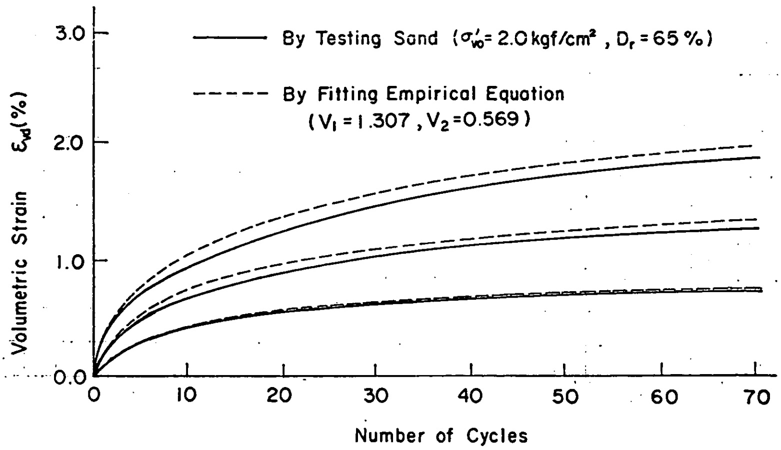

Fig. 50 Volume Change Characteristics

Table 1

e_{max}	1.323
e_{min}	0.758
G_s	2.713
D_{50}	0.242mm

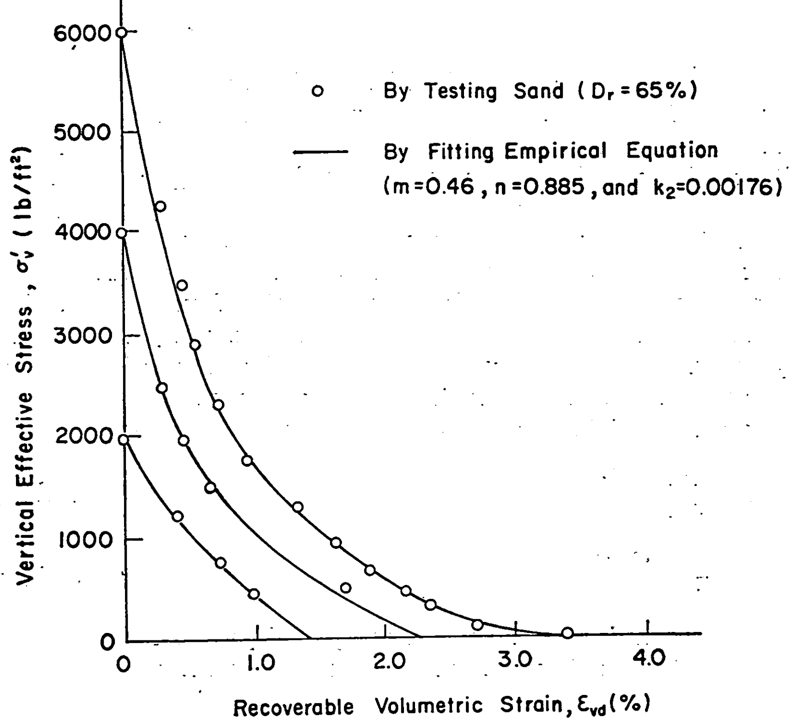

Fig. 51 Rebound Characteristics

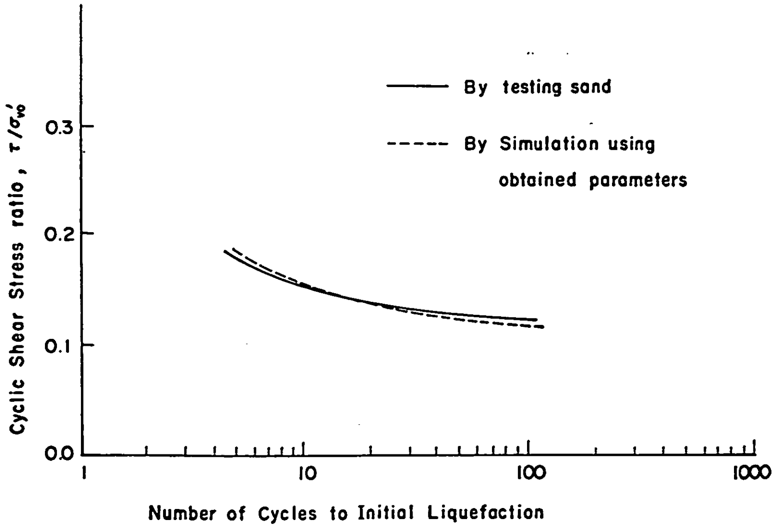

Fig. 52 Comparison of Simulated and Tested Liquefaction Strength

and % units.

Constants for the stress-strain relation G_{m0} and τ_{m0} were estimated by the Hardin-Drnevich equations[14] with $e=0.9557$, $K_0=0.42$, $\phi'=35.45°$. Undrained cyclic loading tests of the Ishinomaki sands at constant stress amplitude were simulated using the effective stress model with the above values for the model parameters. Results of the simulation agreed very well with the test data as shown in Fig. 52, confirming the vailidity of the parameters for tested sand of which relative density is 65%.

(3) Parameters for Sands other than Tested Sands

For sand at different relative densities, the parameter were determined as follows. The pore water pressure parameters may be classified into two groups; namely, V_1 and V_2 for volumetric strain generation and k_2, m, and n for rebound modulus. In general, relative density is considered to have an influence on not only volumetric strain but also rebound modulus. The influence of relative density, however, is not quantatively known for sands at Ishinomaki Port. In the present study, the value of volumetric strain is not explicitly investigated and only pore water pressure is analyzed. Therefore, in order to simplify the procedure, only V_1 and V_2 were varied in accordance with relative densities and k_2, m, and n were fixed at the values corresponding to 65% relative density.

From the results of Section 4.2, V_1 and V_2 are expressed as

$$V_1 = V_1^{*} \cdot \left(\frac{\sigma_{v0}'}{\sigma_{v0e}'}\right)^{n-0.5} \qquad \text{(31)(again)}$$

$$V_2 = V_2^{*} \cdot \left(\frac{\sigma_{v0}'}{\sigma_{v0e}'}\right)^{0.5-n} \qquad \text{(32)(again)}$$

where V_1^* and V_2^* are the values of V_1 and V_2 at vertical confining pressure σ_{voe}' and n is one of rebound modulus constants.

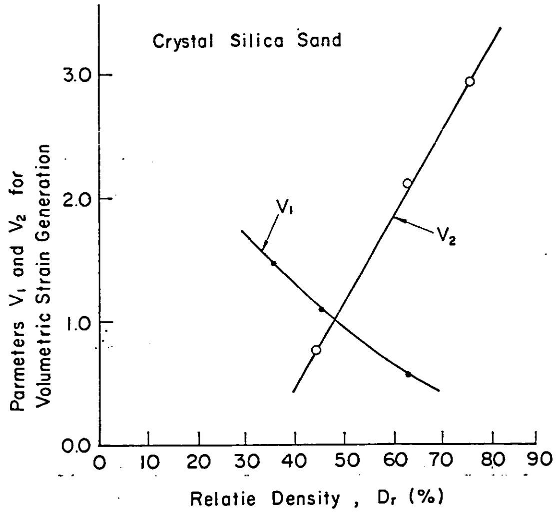

Fig. 53 Relative Density Dependence of Parameters V_1 and V_2 for Crystal Sylica Sand

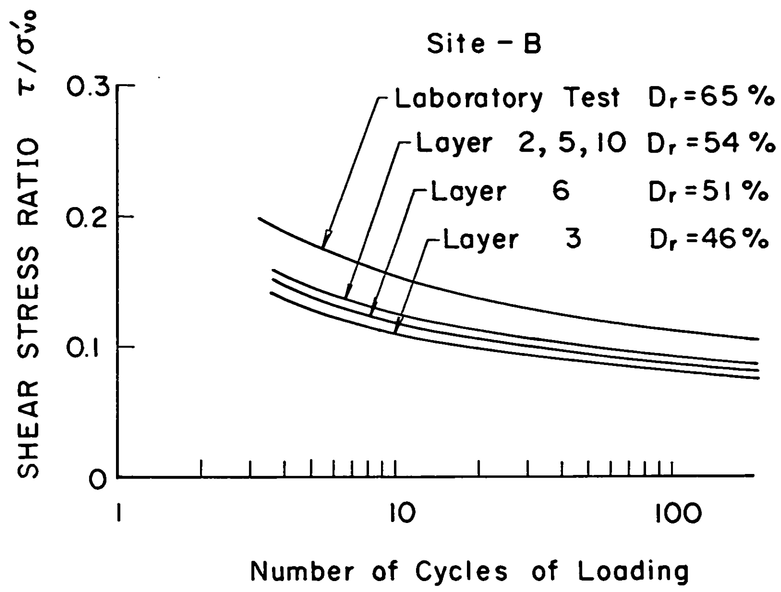

Fig. 54 Simulated Liquefaction Strength Curves for Sand Layers at Site-B

Experimental result on crystal silica sand showed that, if a relative density D_r increases, V_1 decreases and V_2 increases as shown in Fig. 53. For simplicity, we assumed linear variations of V_1^* and V_2^* against D_r. For V_2^*, by assuming $V_2^*=0$ at $D_r=0\%$ and let $\sigma_{v0e}=2.0$ kgf/cm², then

$$V_2^*=0.008754\,D_r \tag{35}$$

where D_r; relative density in percent

Liquefaction strength is approximately proportional to relative density. To ensure this dependence, V_1^* was derived as

$$V_1^*=-0.1944\,D_r+13.94 \tag{36}$$

As an example, liquefaction strength curves are shown in Fig. 54 for sand layers at Site B by using equation (31), (32), (35), and (36) together with the determined G_{m0} and τ_{m0} for each layer. As shown in Fig. 54, these equations gave satisfactory strength curves concerning the proportional relation in the range $D_r=$ 45 to 65%. Determination procedure for G_{m0} and τ_{m0} will be explained in the next chapter.

5. Analysis of the Liquefaction by the Effective Stress Model

5.1 Outline of the Model

The model used in the present study is a lumped mass system representation of horizontally layered ground with an elastic base[2]. The model is one dimensional in such a sense that input motion and deformations of the system are fixed to one horizontal direction. The readers who have skipped section 4.2 may need the following description, but others can skip the rest of this section. Stiffness of the

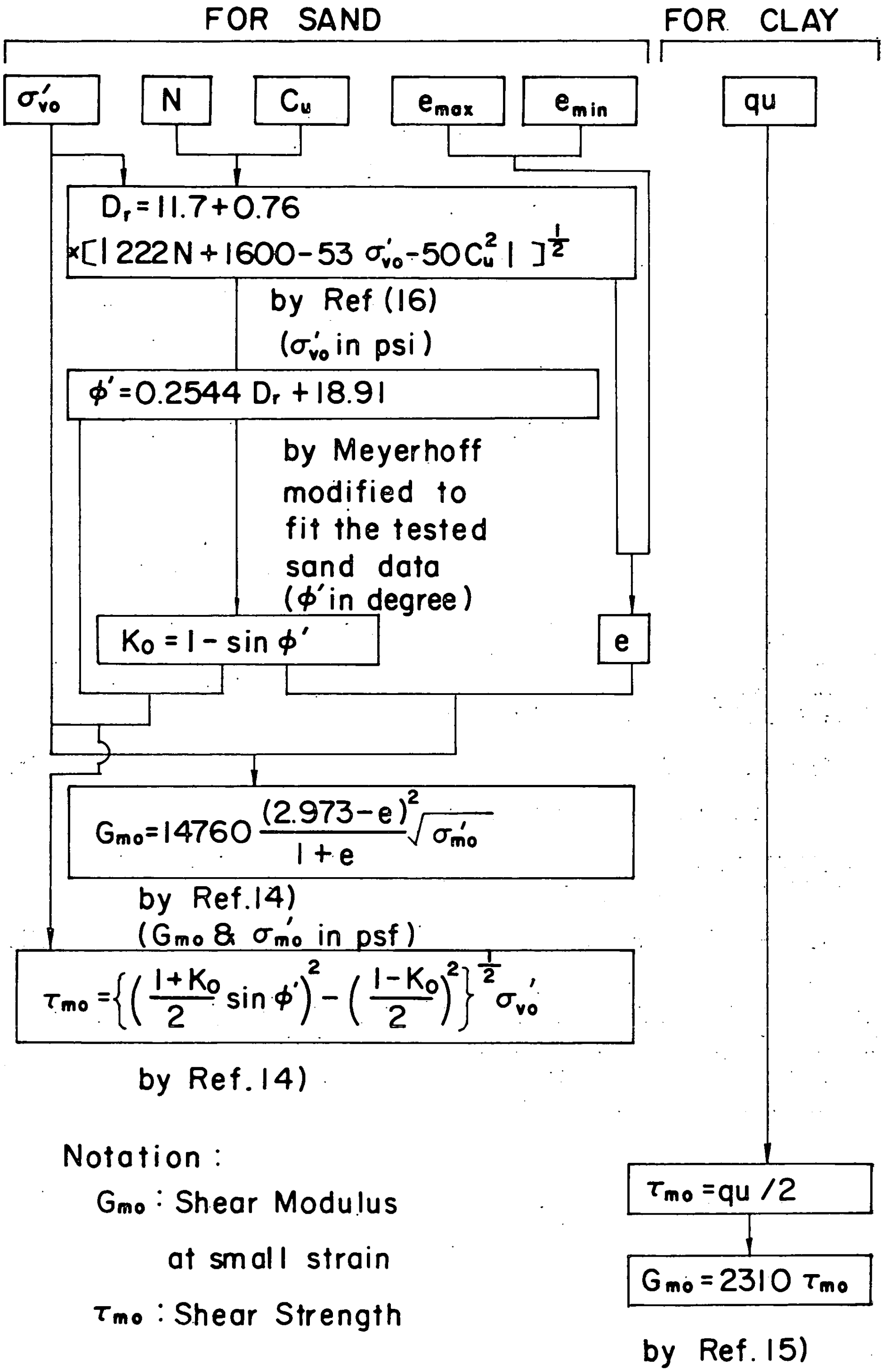

Fig. 55 Determination Procedure for Parameters of Non-Linear Stiffness of Ground

system is a non-linear hysteretic type which is governed by a stress-strain relation of so-called Hysteretic Hardin-Drnevich Model which was illustrated in Fig. 45 and explained in section 4.2. Shear modulus at small strain level and shear strength determine the stress-strain relation. For each half cycle of shear strain response, increment of pore water pressure is calculated from shear strain amplitude and effective vertical stress. The model has capability to consider dissipation of pore water pressures but this effect was not simulated for the present study because of lack of precise information. This effect will be discussed at the comparison of the simulation results and the observed site performances in a later section.

5.2 Modelling of Response Characteristics of the Sites

(1) Estimation of Model Parameters

The soil condition of each site was idealized into a horizontally layered ground for the simulation. Division into layers is indicated in Fig. 39 by the horizontal lines in the columns of soil type.

Parameters of the model are classified into three types; namely, parameters for pore water pressure generation, parameters for non-linear stiffness, and parameters for mass. Parameters for pore water pressure generation were already explained in the previous chapter. The rest of two kinds of parameters is explained in this section.

a) Parameters for Non-linear Stiffness

Parameters for non-linear stiffness are shear modulus at small strain level and shear strength. A set of correlations between geotechnical constants were used for estimation of these parameters. Fig. 55 summarises the procedure.

For clay, shear strength was determined by unconfined compression strength and then, by using an empirical relation[15], shear modulus at small strain level was determined from the shear strength.

For sand, determination procedure is fundamentally based on the equations proposed by Hardin and Drnevich[14] for shear modulus at small strain level and shear strength. The equation for shear modulus at small strain level is empirical but the equation for shear strength is derived from Mohr-Coulomb's failure criteria. Because these equations need several geotechnical constants which were not directly measured, an estimation procedure was necessary for these constants. The following estimation procedure was used.

The relative density was estimated from the N-values, vertical confining pressure, and the coefficient of uniformity of the sand by using an empirical equation[16]. Coefficient of uniformity varies greatly in accordance with types of soils in Ishinomaki Port. However, applicability of the empirical equation is somewhat doubtful for sands of coefficient of uniformity which is out of the test range of the empirical equation. Coefficients of uniformity of laboratory samples from the top layers in Ishinomaki Port were within the admissible range but those of the other sands were out of the range. The coefficients of uniformity of the laboratory tested sands were used for all the layers. This procedure introduces some unavoidable uncertainty in the estimation of relative density.

It is widely understood that, if fines content of sands becomes greater, the N-value tends to be smaller for sand at the same relative density. For example, Gibbs and Holtz[17] shows a data that relative density of fine sand is approximately 20% greater than that of coarse sand in saturated condition for the same N-value and vertical confining pressure. To take this fact into account, 20% was added to

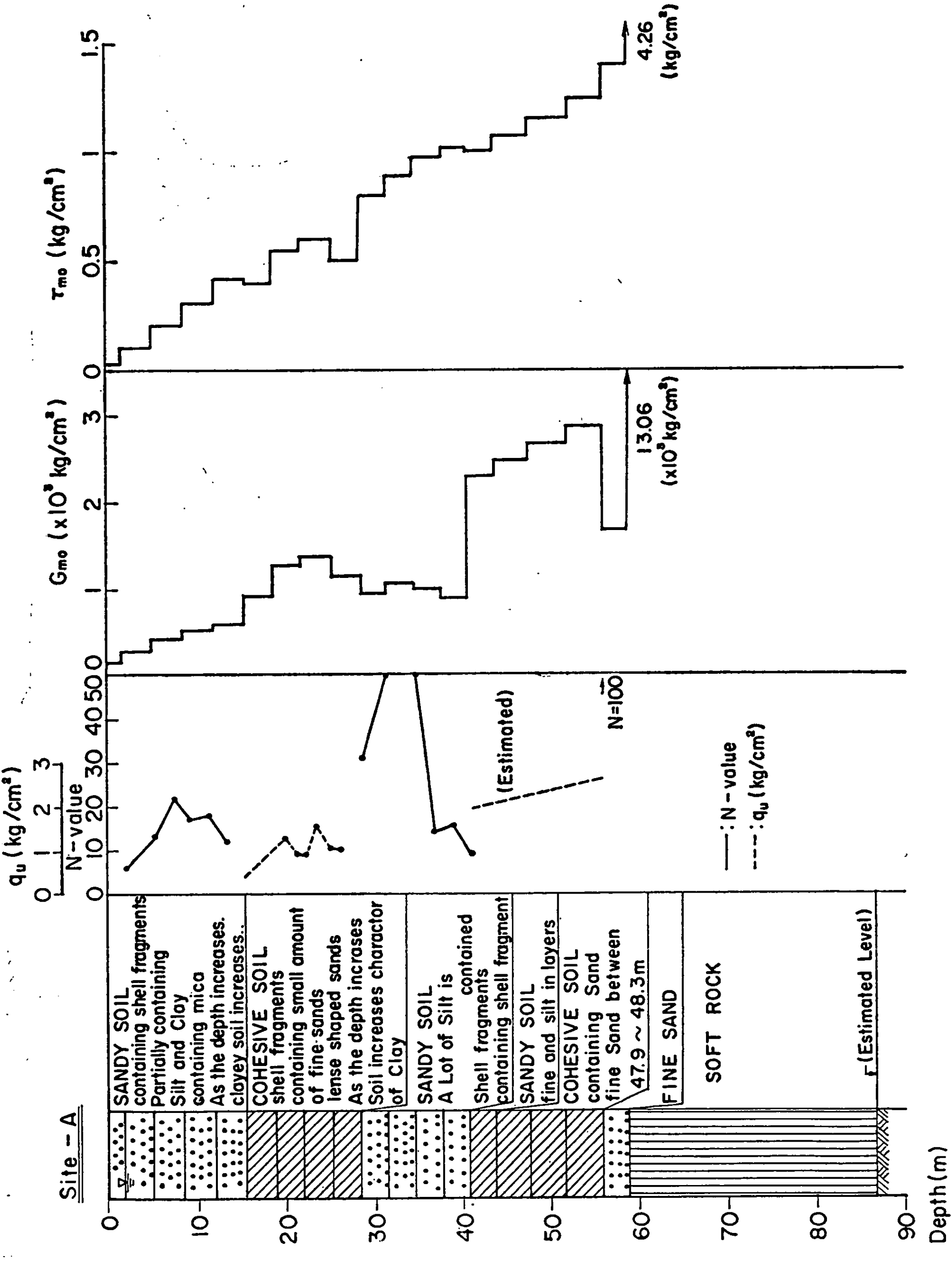

(a) Original Ground Conditions and Determined G_{mo} and τ_{mo}

Fig. 56 Ground Model Parameters for Site A

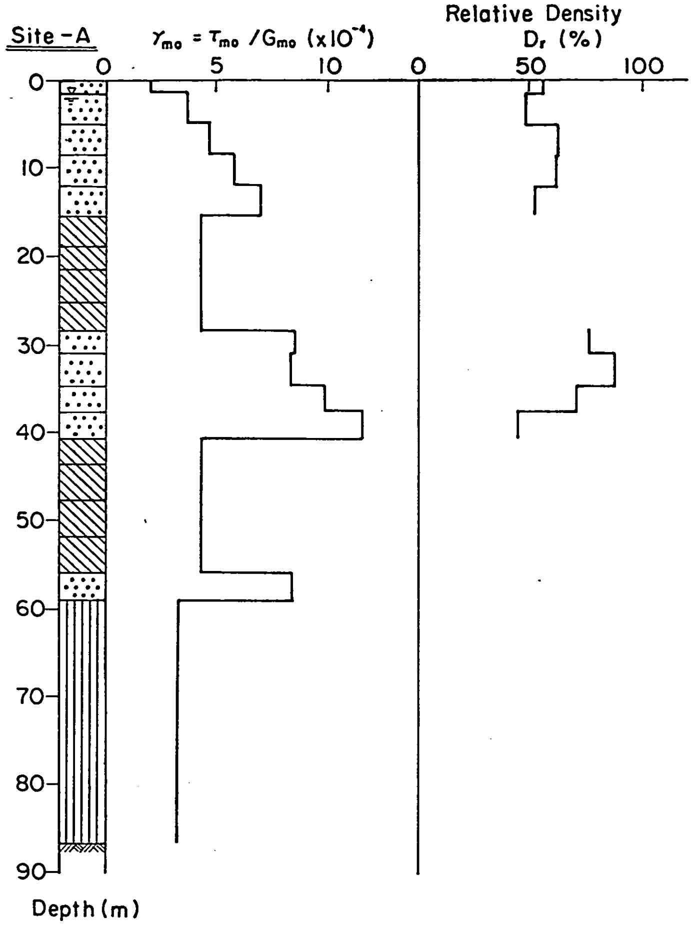

(b) Reference Strain γ_{m0} and Relative Density D_r

the estimated relative density for silty sands as a rough compensation. The relative densities thus estimated are also used for estimation of liquefaction strength.

The effective angle of shear resistance was estimated from the relative density. Meyerhoff's data indicates a linear relation is a reasonable approximation to the relationship between relative density and effective angle of shear resistance over the likely range of interest in this study. The relationship was calibrated using the measured effective angle of shear resistance 35.45° for the sands at Ishinomaki Port.

The coefficient of earth pressure at rest K_0 was estimated from effective angle of shearing resistance by the empirical formula shown in Fig. 55. Results using the formula agreed with the laboratory test data for sands from the top layers at Ishinomaki Port.

The void ratio was estimated from the estimated relative density. However, the maximum and minimum void ratios were available only for sands from the top layers in Ishinomaki Port.

The parameters for soft rock layers or gravel layers above the base rock at Sites A, B, and C were determined by assuming that velocity of shear wave propaga-

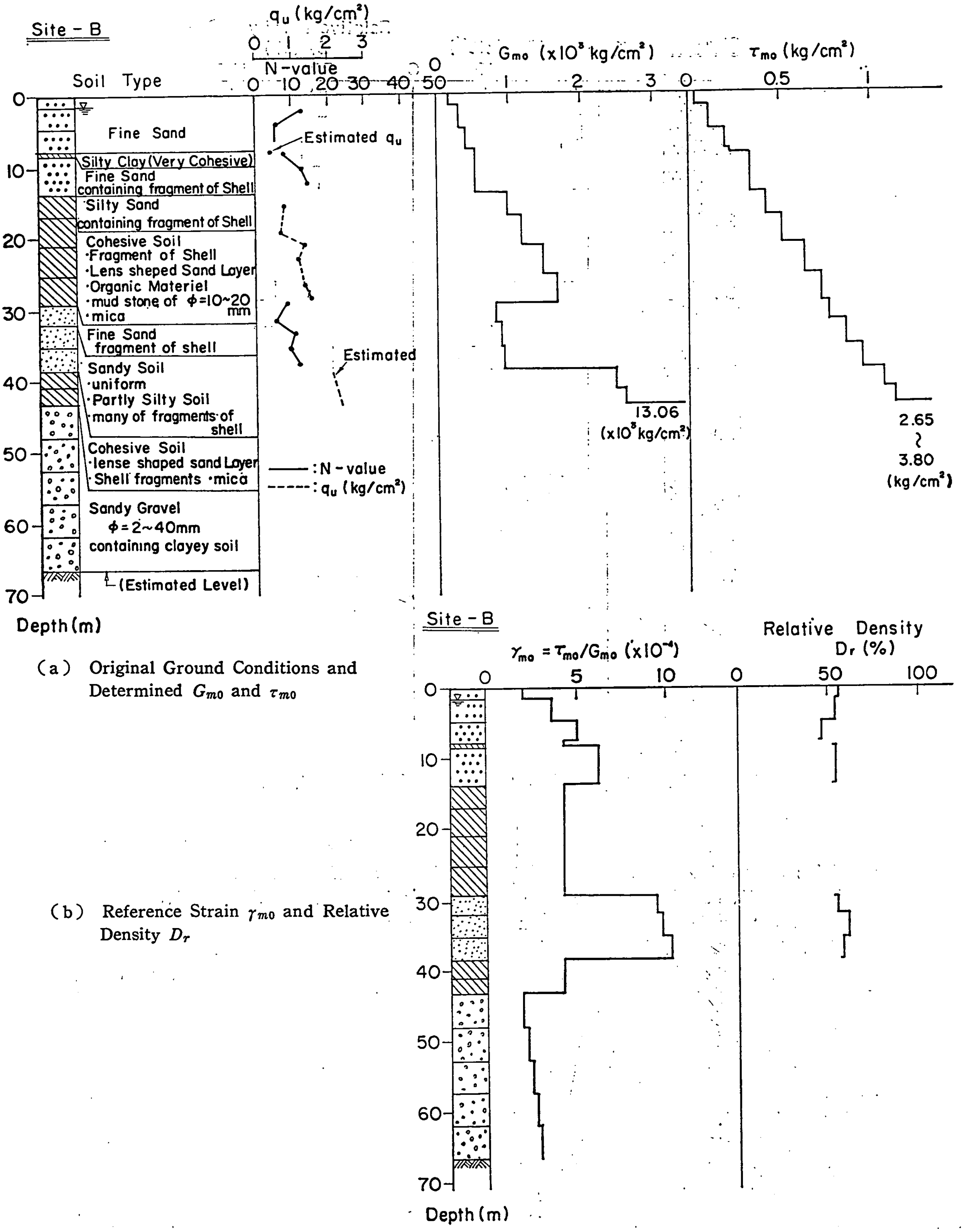

(a) Original Ground Conditions and Determined G_{mo} and τ_{mo}

(b) Reference Strain γ_{mo} and Relative Density D_r

Fig. 57 Ground Model Parameters for Site B

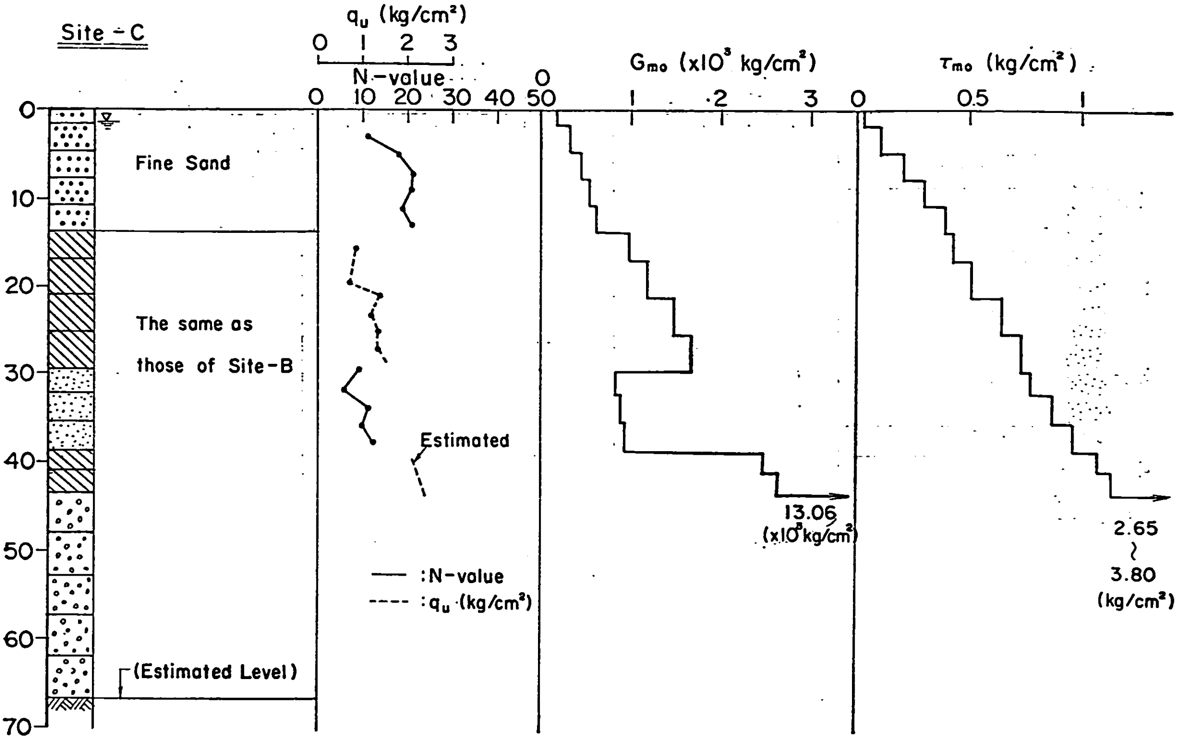

(a) Original Ground Conditions and Determined G_{m0} and τ_{m0}

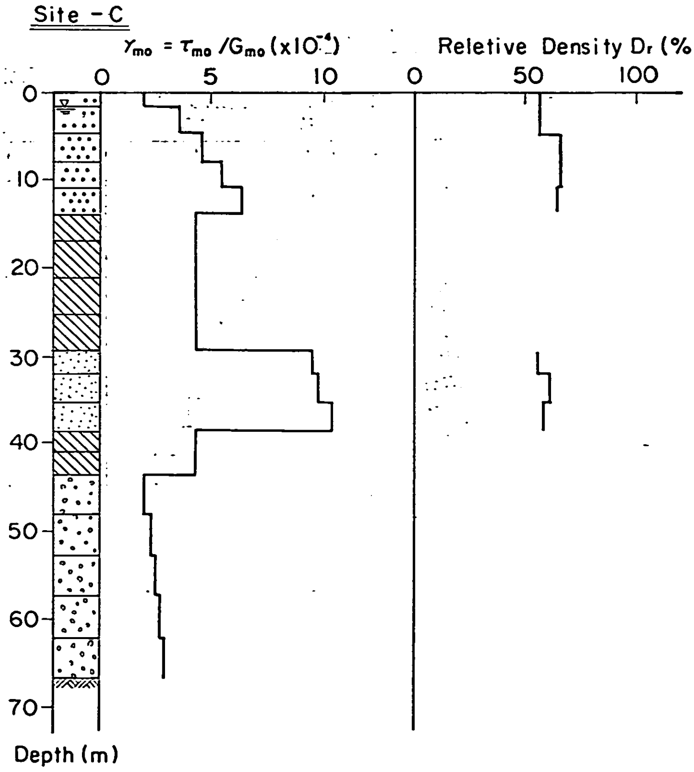

(b) Reference Strain γ_{m0} and Relative Density D_r

Fig. 58 Ground Model Parameters for Site C

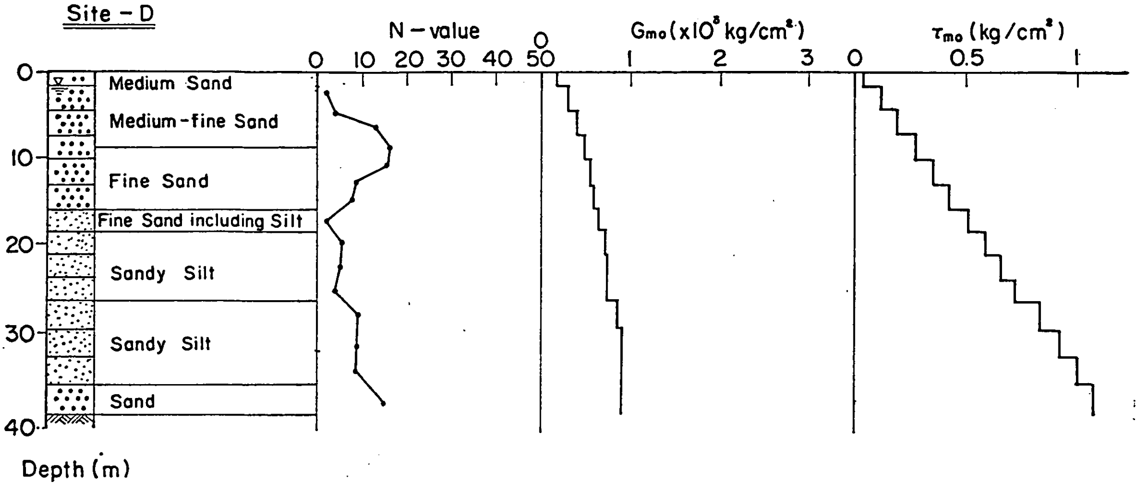

(a) Original Ground Conditions and Determined G_{m0} and τ_{m0}

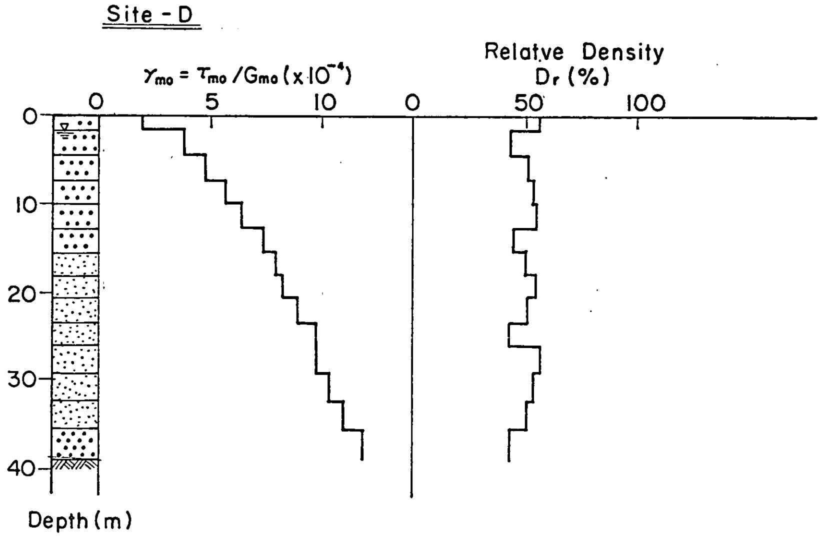

(b) Reference Strain γ_{m0} amd Relative Density D_r

Fig. 59 Ground Model Parameters for Site D

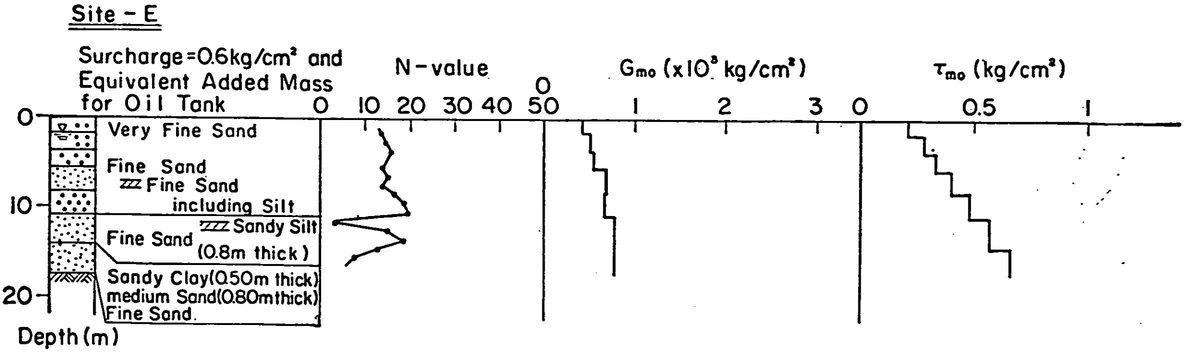

(a) Original Ground Conditions and Determined G_{m0} and τ_{m0}

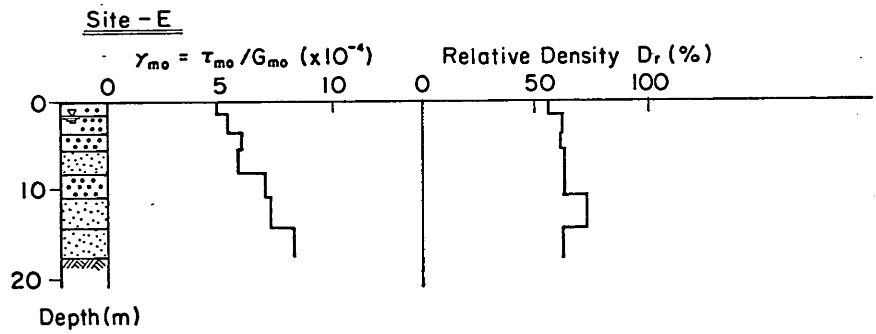

(b) Reference Strain γ_{m0} and Relative Density D_r

Fig. 60 Ground Model Parameters for Site E

tion is 800 meters/second and that the shear strength is strong enough to resist uniform ground acceleration of 300 Gals. These values are considered to be within an admissible range for soft rock layers or gravel layers.

Shear wave velocity of the base rock was estimated to be 1300 meters/second by using measured value at the rock outcrop at the accelerograph site shown in Fig. 4, which is within 5 km of Ishinomaki Port as mentioned earlier.

b) Parameters for Mass

In-situ bulk densities were not measured at Ishinomaki Port.

For sand and clay, the values normally used for design of port structures in Japan were employed. Bulk densities employed were 2.0 gf/cm³ and 1.7 gf/cm³ for saturated sand and clay, respectively, and 1.6 gf/cm³ for sand above ground water level.

Bulk density of soft rock layers or gravel layers above the base rock at Sites A, B, and C were considered to be 2.0 gf/cm³. Bulk density of the base rock was estimated to be 1.8 gf/cm³ by using the measured values of the base rock at Shiogama Port, the location of which is shown at the upper left corner in Fig. 1.

(2) Estimated Ground Model Parameters for the Simulation

Figures 56 to 61 show the ground model parameters used in the simulations

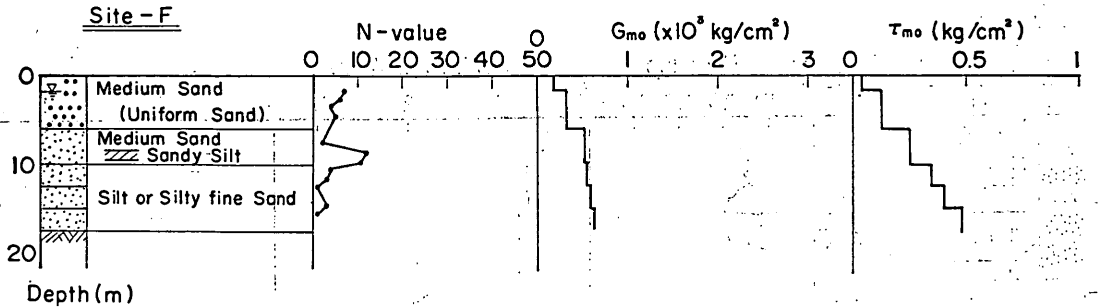

(a) Original Ground Conditions and Determind G_{m0} and τ_{m0}

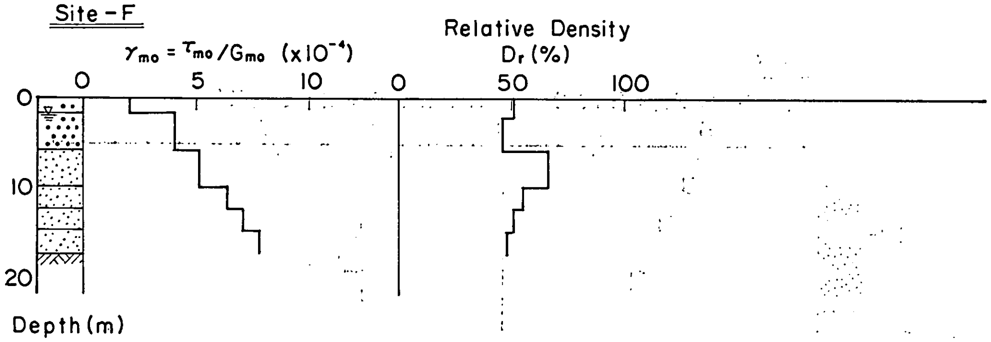

(b) Reference Strain γ_{m0} and Relative Density D_r

Fig. 61 Ground Model Parameters for Site F

together with descriptions of soil conditions from which most of the parameters were estimated.

The estimated value of G_{m0}, which is a shear modulus at small strain level, had a tendency to increase in proportion to depth, or more precisely speaking, in proportion to square root of depth in sandy layers and in proportion to depth in clayey layers. The rate of increase of G_{m0} with depth for sandy layers was smaller than that for clayey layers. As a result, G_{m0} of lower sandy layers which are located below upper clayey layers constituted a zone of lower G_{m0} as shown in Figs. 56 to 61. There was no significant dependence of G_{m0} on N-value.

The estimated value of τ_{m0}, which is shear strength, had also a tendency to increase in proportion to depth. There was not a great difference in the rate of increase of τ_{m0} with depth between at sandy layers and clayey layers. Dependence of τ_{m0} on N-value was not great.

Reference strain γ_{m0} is an index of non-linearity of ground as will be understood by Fig. 45. The smaller γ_{m0} is, the stronger non-linearity is. γ_{m0} for clayey layers were about 5×10^{-4}. γ_{m0} for sandy layers had a tendency to increase in accordance with depth and it ranged from 2×10^{-4} to 10×10^{-4}. Dependence of γ_{m0} on N-value was not significant.

G_{m0}, τ_{m0}, and γ_{m0} at Site E were greater than those at other sites for the same depth. This is considered due to the effect of great surcharge from the oil tank

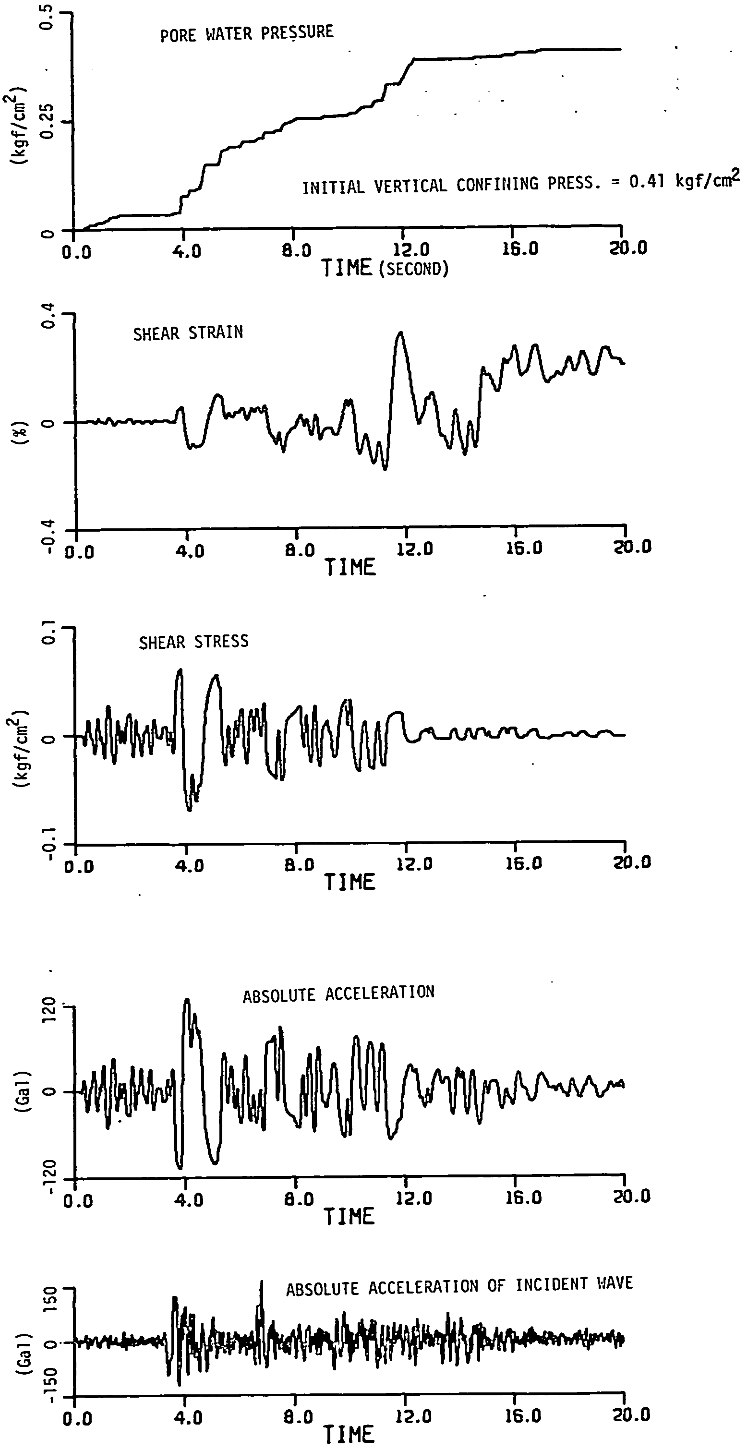

Fig. 62 Results of the Simulation in Layer 2 (from 1.5 meter to 5 meter depth) at Site A

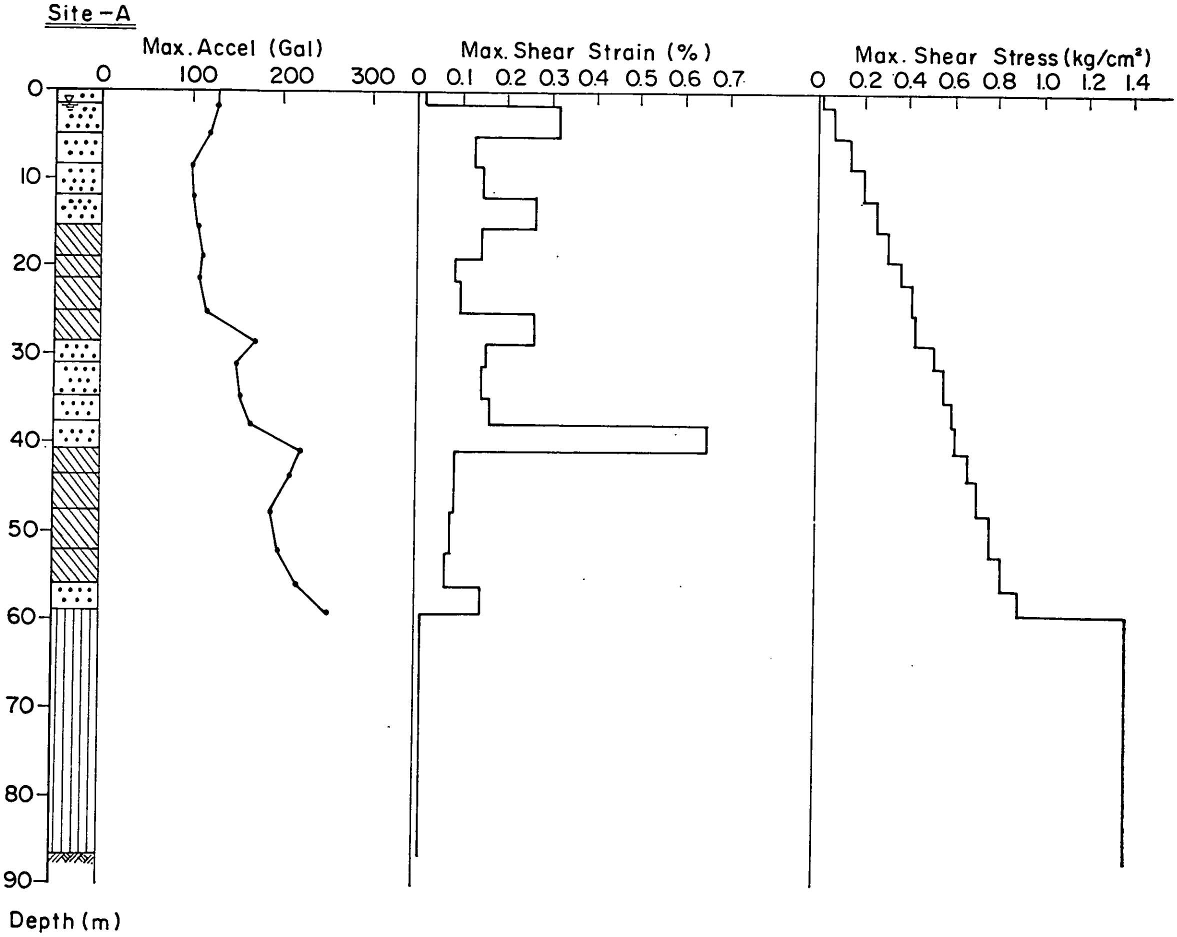

(a) Maximum Acceleration, Maximum Shear Strain, and Maximum Shear Stress

Fig. 63 Results of the Simulation for Site A

at Site E.

5.3 Modelling of Input Ground Motion

(1) Wave Form

The largest acceleration component, W42N, recorded on the rock outcrop was used as input motion.

The base line of the record was corrected by a high-pass filter named as FIXED FILTER which is used for routine processing of strong motion accelerograms obtained in the strong motion observation network of the Port and Harbour Research Institute[4]. The cut-off frequency is approximately 0.15 Hz. This correction has great influence on simulated shear strain.

The record was obtained by SMAC-B2 accelerograph which covers the frequency range up to about 7 Hz[4]. The record was digitized at unequal time intervals by the Public Works Research Institute and the longest sampling interval was 0.07

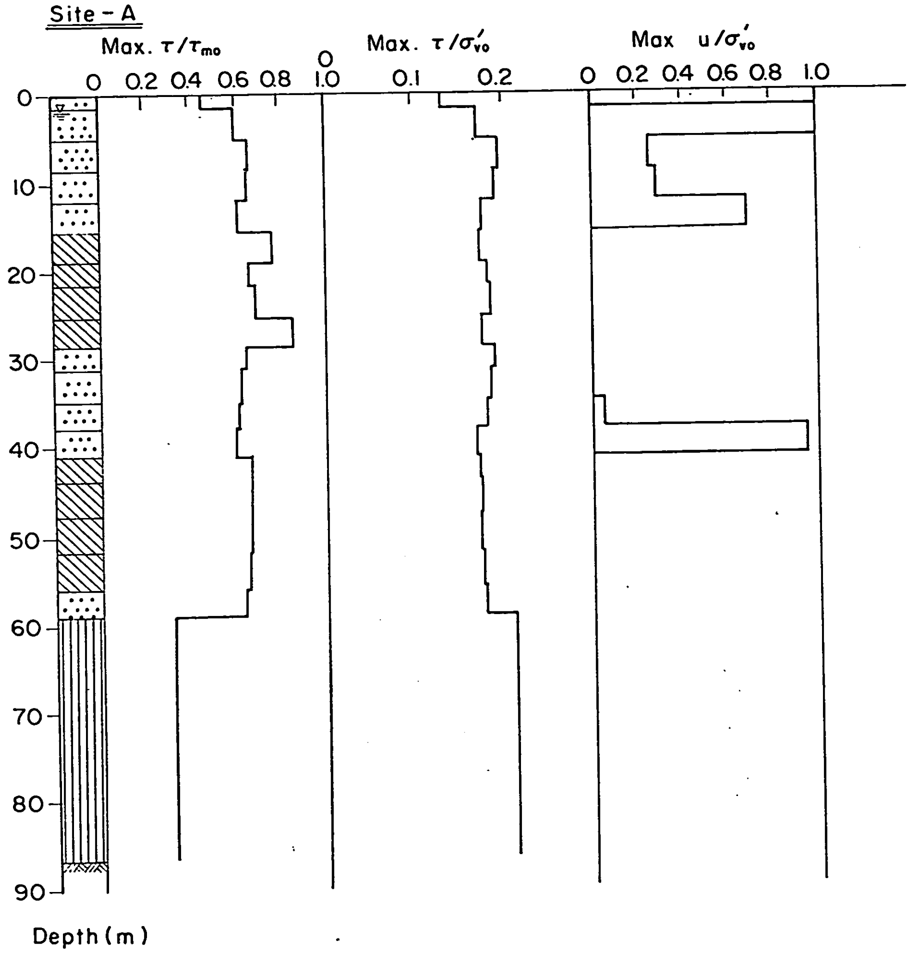

(b) Maximum Stress Ratio τ/τ_{m0}, Maximum Stress Ratio τ/σ_{v0}', and Maximum Pore Water Pressure Ratio u/σ_{v0}'

seconds which corresponds to a Nyquist Frequency of 7 Hz. Therefore, no correction was done for the frequency response characteristics of the accelerograph. The highest frequency component which can go through the present lumped mass system models at small strain level was around 10 Hz so that correction for high frequency components would have little influence.

(2) Two Dimensional Shaking Effect

The model is one dimensional as described earlier, whereas the actual motion is three dimensional. Influence of vertical component on liquefaction may be negligible in usual cases but that of the other horizontal component is not negligible19).

If both horizontal components were of identical form and perfectly in phase, the resultant motion would be about 40% greater than that of single component. Since the motions are not equal or is in phase and the largest horizontal component was selected, this component was increased by 20% to simulate the effect of the two

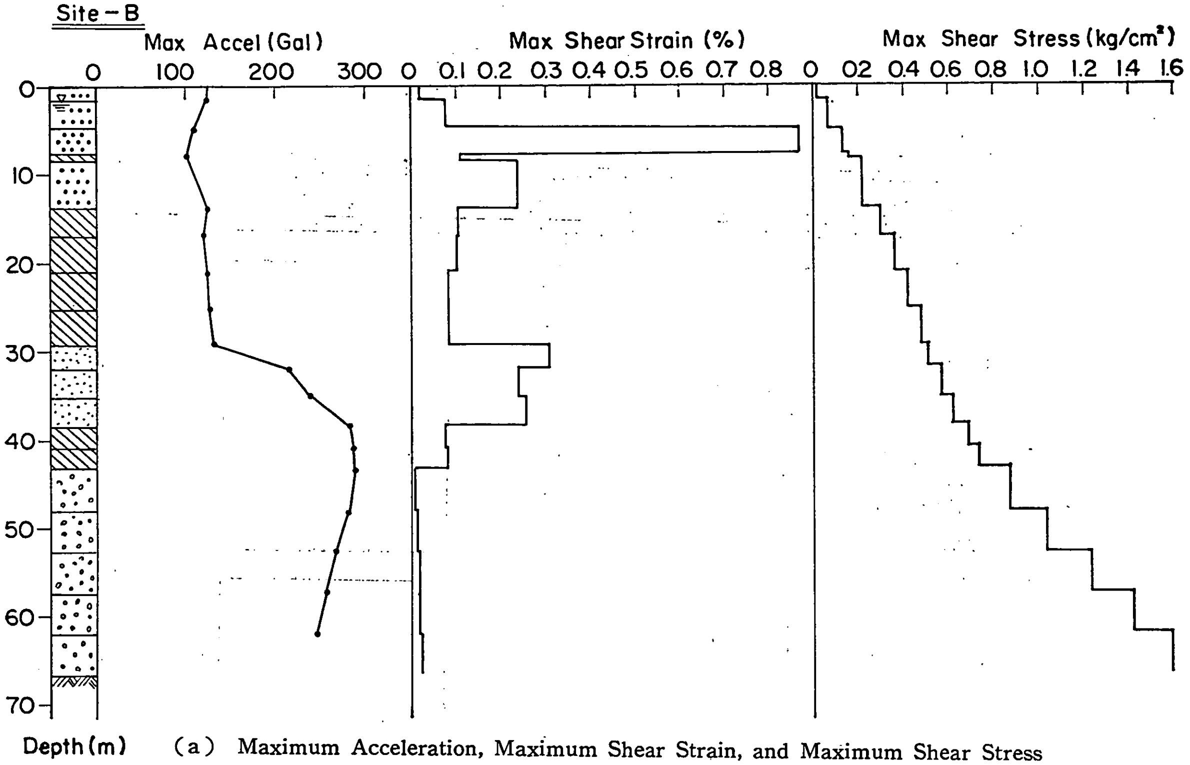

(a) Maximum Acceleration, Maximum Shear Strain, and Maximum Shear Stress

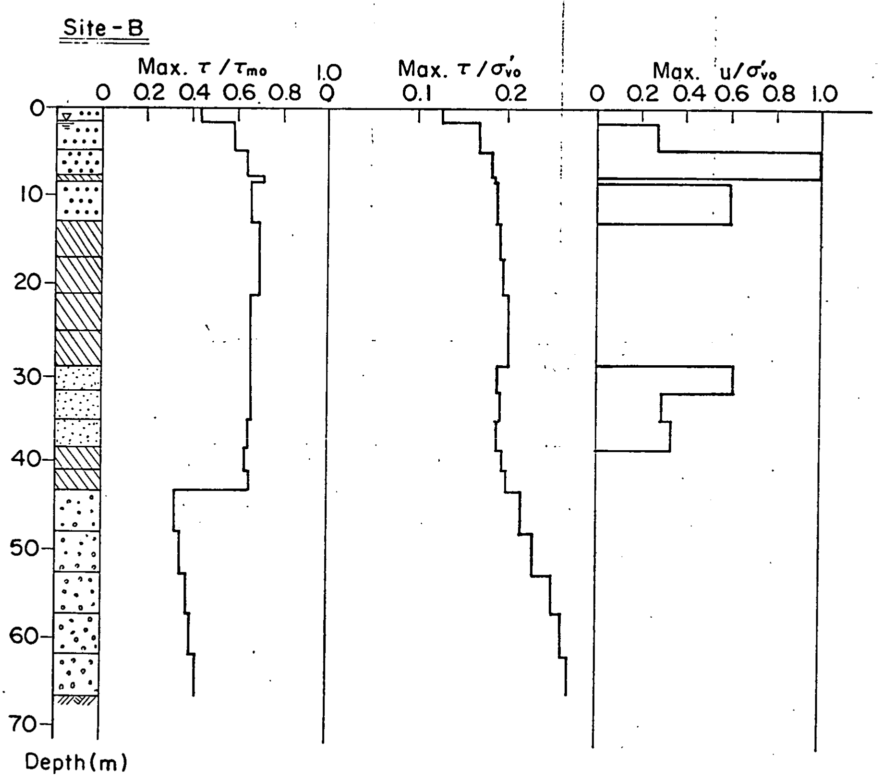

(b) Maximum Stress Ratio τ/τ_{m0}, Maximum Stress Ratio τ/σ_{v0}', and Maximum Pore Water Pressure Ratio u/σ_{v0}'

Fig. 64 Results of the Simulation for Site B

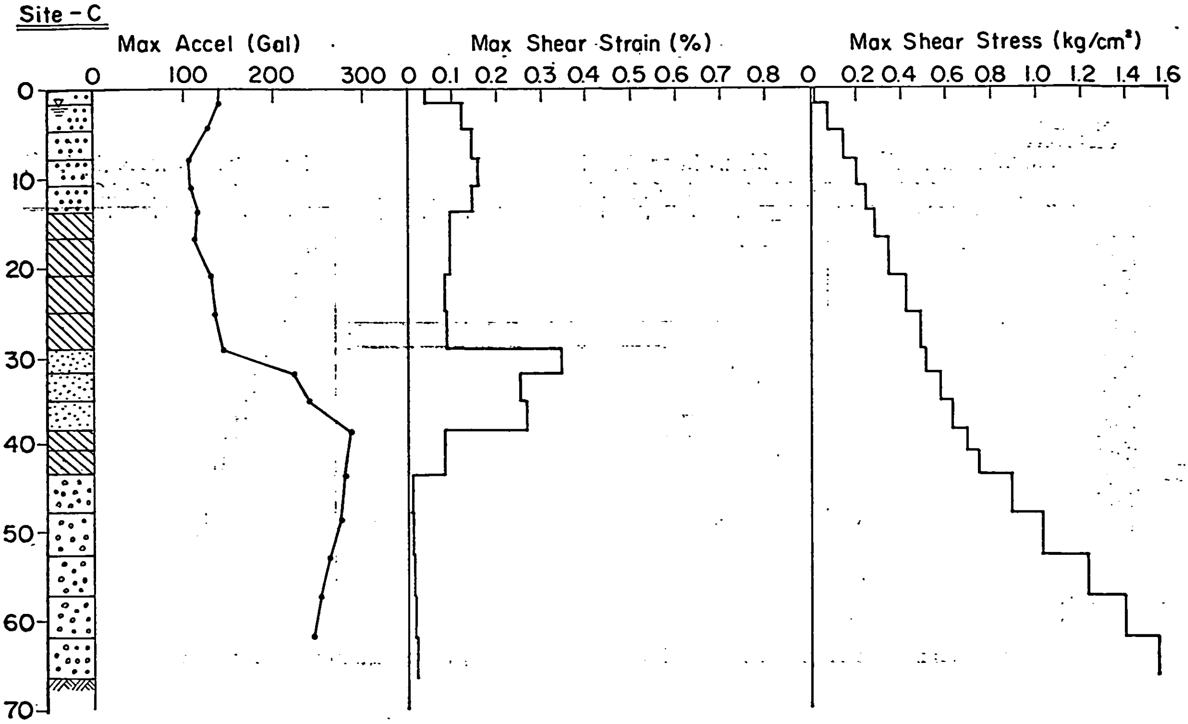

(a) Maximum Acceleration, Maximum Shear Strain, and Maximum Shear Stress

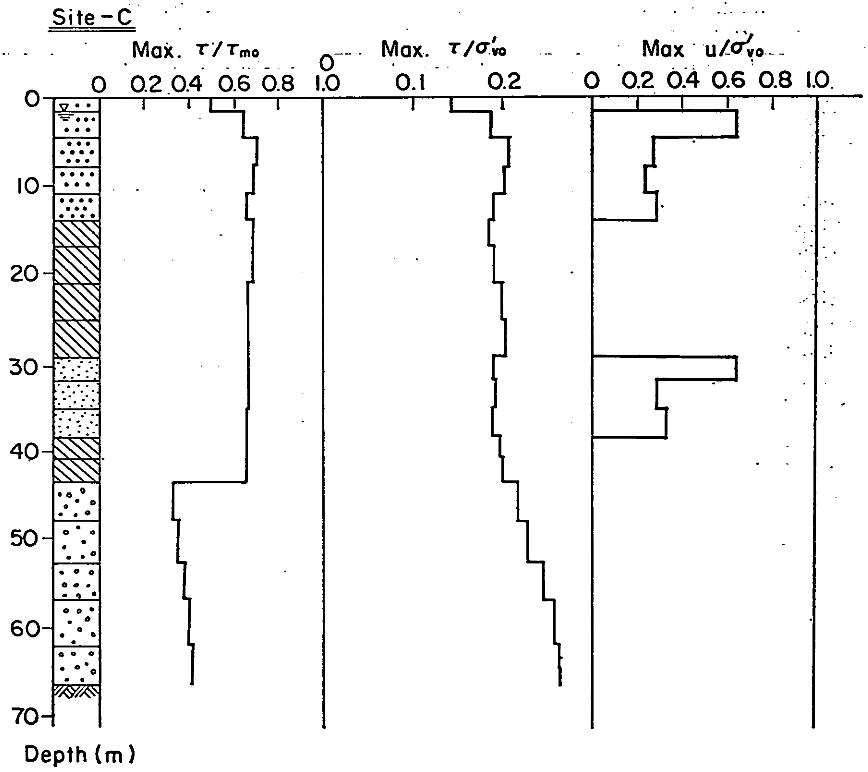

(b) Maximum Stress Ratio τ/τ_{m0}, Maximum Stress Ratio τ/σ_{v0}', and Maximum Pore Water Pressure Ratio u/σ_{v0}'

Fig. 65 Results of the Simulation for Site C

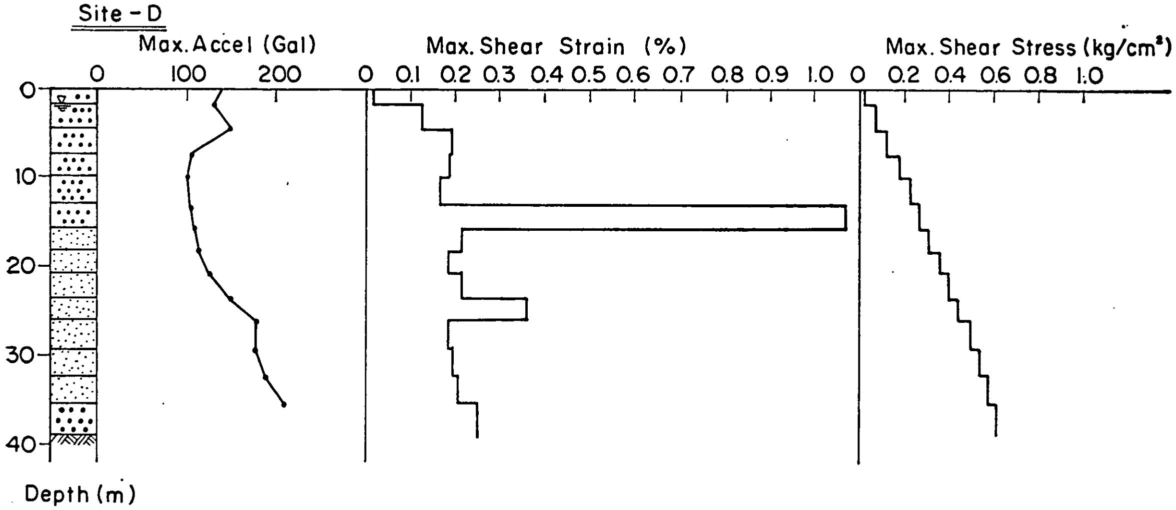

(a) Maximum Accleration, Maximum Shear Strain, and Maximum Shear Stress

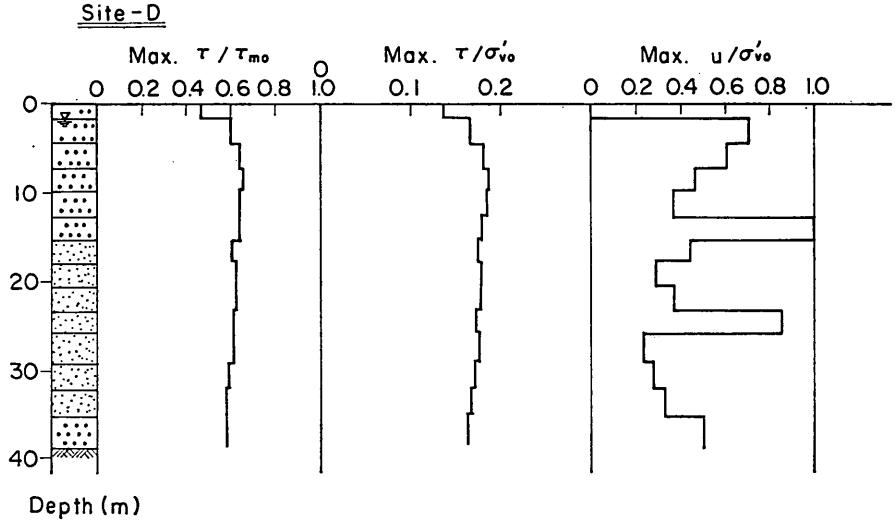

(b) Maximum Stress Ratio τ/τ_{m0}, Maximum Stress Ratio τ/σ_{v0}', and Maximum Pore Water Pressure Ratio u/σ_{v0}'

Fig. 66 Results of the Simulation for Site D

horizontal components. This correction is of the same order as suggested by the work of Ishihara and Yamazaki[19] on multi-directional loading.

5.4 Results of Simultation

An example of the results of the response analysis is shown in Fig. 62 for the layer 2 which is located from the 1.5 meter to 5 meter depth at Site A.

Excess pore water pressure increased sharply when the incident wave of significant phase arrived at about four seconds, where the origin of the time is the

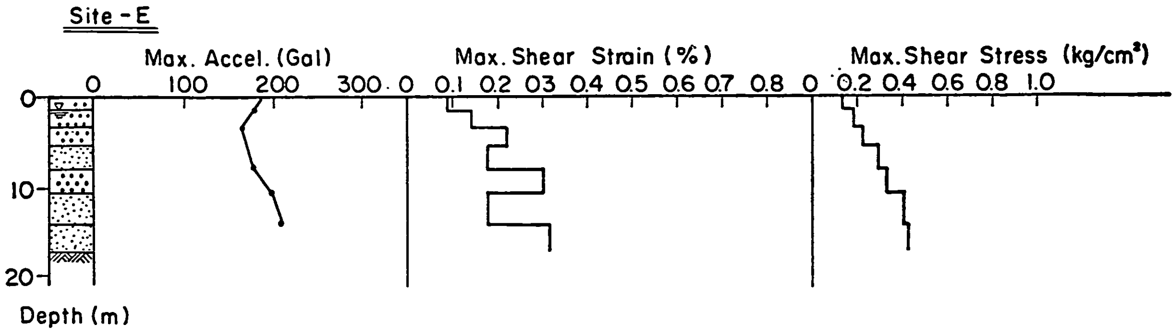

(a) Maximum Acceleration Maximum Shear Strain, and Maximum Shear Stress

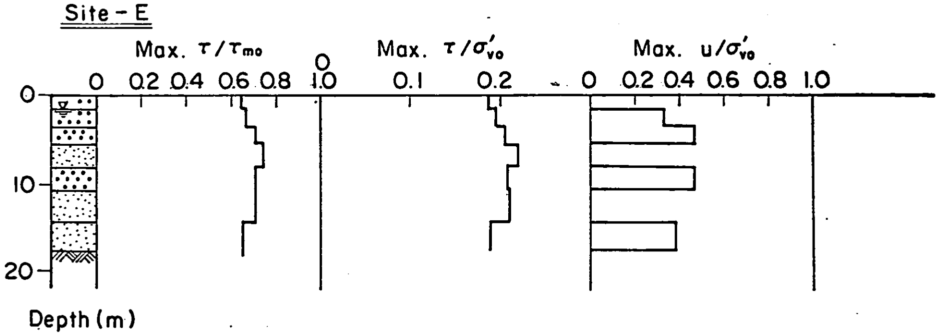

(b) Maximum Stress Ratio τ/τ_{m0}, Maximum Stress Ratio τ/σ_{v0}', and Maximum Pore Water Pressure Ratio u/σ_{v0}'

Fig. 67 Results of the Simulation for Site E

initial step of the integration of the equations for simulating ground response. However, a very sharp increase in excess pore water pressure did not occur at about seven seconds when the maximum acceleration of the incident wave arrived. Sharp increases in excess pore water pressure again took place at about 12 seconds. There was no incident wave of significant amplitude in acceleration arrived at this time, but shear strain was maximum at 12 seconds. These results indicate that the increment in pore water pressure depends not only on the intensity of the input motion but on the current state of the soil. Excess pore water pressure reached the vertical confining pressure at 17 seconds and this layer is considered to have liquefied.

The shear strain time history reveals a residual shear strain at the end of the shaking and consequently a residual horizontal displacement. Time history of shear stress shows a decrease in amplitudes particularly after the ground was close to liquefaction at about 12 seconds. On the other hand, shear strain amplitude corresponding to these small shear stress was very great and even attains a maximum at about 12 seconds. They are due to softening of the shear modulus and decrease in the shear strength. The effective stress model is considered to be the only model which is able to simulate these effects.

Time history of acceleration shown in the second figure from the bottom

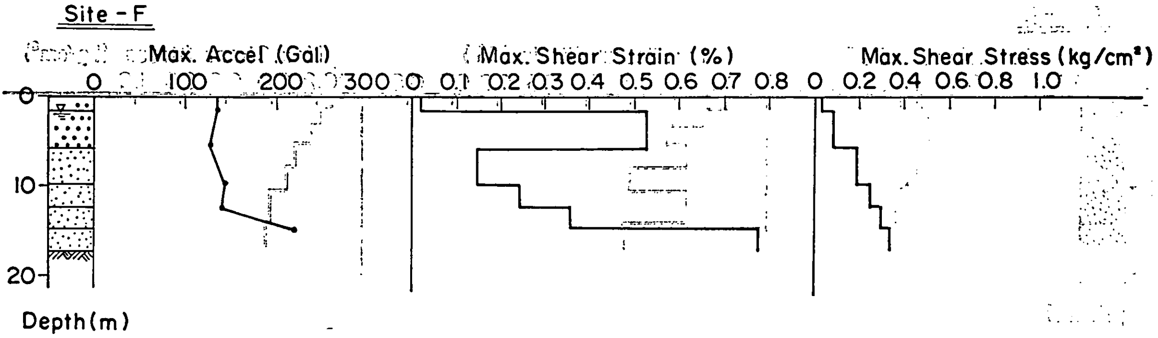

(a) Maximum Accleration, Maximum Shear Strain, and Maximum Shear Stress

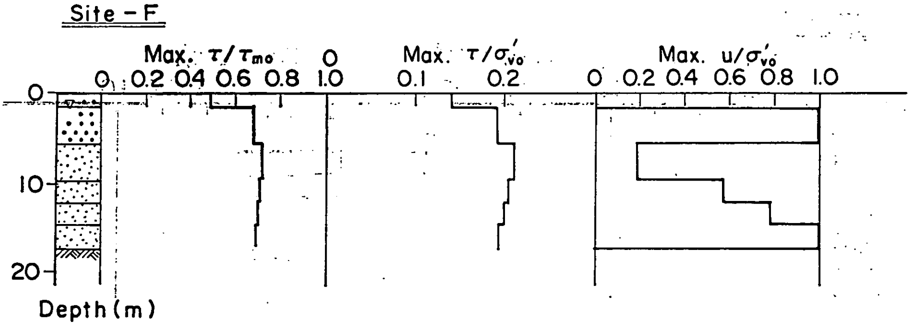

(b) Maximum Stress Ratio τ/τ_{m0}, Maximum Stress Ratio τ/σ_{v0}', and Maximum Pore Water Pressure Ratio u/σ_{v0}'

Fig. 68 Results of the Simulation for Site F

indicates that the incident wave of the initial significant phase at four seconds had been transmitted up to this layer, but the second significant phase at seven seconds was hardly transmitted at all due to softening and weakening of the ground by the excess pore water pressure rise at seven seconds.

Figures 63 to 68 show summaries of computed results. The maximum accelerations shown on these figures were attained at about four seconds which corresponds to the first arrival of the incident wave of the significant phase. They show reduction in amplitude from the base rock to the top of the ground in general. There are only slight differences in the maximum accelerations between at liquefied sites and at non-liquefied sites. The maximum acceleration of ground surface ranges from 130 Gals to 150 Gals except for Site E. The amount of maximum accelerations are considered to be rather small, especially by considering multiplication of amplitude of the incident wave by the factor of 1.2 explained in Section 5.3, in comparison with past strong-motion records of ground surface at the great earthquakes of which scale is equivalent to the 1978 Miyagi-Ken-Oki Earthquake[20),21)].

The maximum shear strain showed no particular dependence on depth. The maximum shear strain in layers where no excess pore water pressure was generated is about 1×10^{-3}. The maximum shear strain of liquefied layers ranges from 3×10^{-3} to 10×10^{-3}.

The maximum shear stress showed increasing tendency with depth. The maximum shear stress ratios MAX (τ/τ_{m0}) and MAX (τ/σ_{v0}') show almost constant values and the ratios at liquefied sites and non-liquefied sites show no significant difference between themselves. The amounts of the stress ratios were MAX $(\tau/\tau_{m0}) \fallingdotseq 0.7$ and MAX $(\tau/\sigma_{v0}') \fallingdotseq 0.2$.

The maximum excess pore water pressure ratio u/σ_{v0}' is an index of degree of liquefaction with $u/\sigma_{v0}'=1.0$ corresponding to initial liquefaction. The results of the simulation show that liquefaction must have taken place in the layers with relative densities less than 48% (Figs. 56 to 61). The elapsed times at which liquefaction took place at Sites A, B, D, and F were 17.00, 5.55, 7.93, and 7.80 seconds, respectively. Those layers which had not reached the state of liquefaction, however, had pore water pressure ratio of $u/\sigma_{v0}' \fallingdotseq 0.4$, which may not be a negligible increase in pore water pressure for some structures.

6. Comparison of the Simulation Results and the Observed Site Performances

A summary of simulated excess pore water pressure rises are compiled in Fig. 69. From this figure and the study described in Chapter 3 for field performances, a conclusive result is obtained as shown in Table 2. Namely, results of the simulation and the observed site performances are consistent with each other.

As mentioned earlier, the simulation did not include the effect of dissipation of pore water pressure. If the effect of dissipation is included in the simulation, some of pore water will dissipate from a layer with higher pore water pressure to a layer with lower and as a result pore water pressure distribution with the depth will be smoothed. However, it is not considered likely that the predictions of field performance would be affected by the inclusion of dissipation because the fines content of 5% to 30% would prevent significant redistribution of pore water pressure during the relatively short duration of the earthquake.

In the present study, the model was successful in discriminating between sites which liquefied and did not liquefy. A very powerful feature of the model, namely its ability to predict rises in pore water pressure below the level for liquefaction could not be verified in the present study because the necessary field data were not available.

There is one successful field observation of residual pore water pressure rise below the level for liquefaction[22]. The model has been applied successfully to this instance[23]. Measurements of surface accelerations and residual pore water pressures were recorded at Owi Island in Tokyo Bay as a result of the Chiba prefecture earthquake in 1980. Unfortunately accelerations at depth were not recorded. However, when input accelerations were selected that yielded surface accelerations similar to those recorded, the residual pore water pressure time histories at two depths at the site were successfully simulated.

In the final analysis, the quality of predictions will always depend on the quality of the field data and how sensitive the model is to variations in the field data. These matters are continually under scrutiny.

The Port and Harbour Research Institute is deploying pore water pressure meters and accelerometers at a suitable site in Japan in order to obtain the kind of data that would allow a definitive verification of the effective stress model described above and indeed of other proposed models. However, it may be later years to acquire the necessary data.

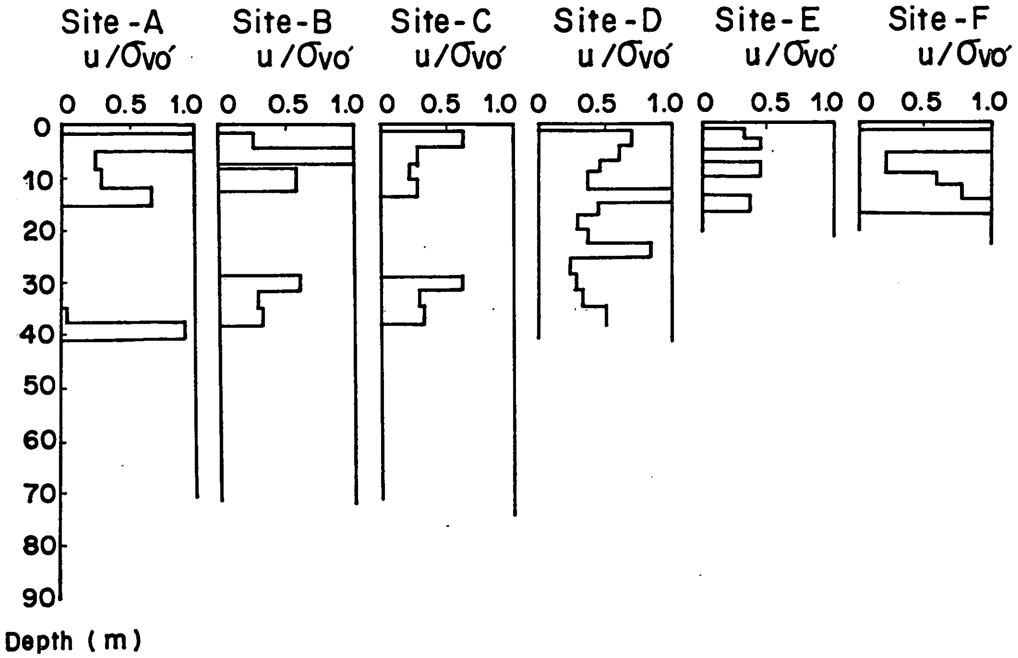

Fig. 69 Summary of Simulated Pore Water Pressure Rise

Table 2 Comparison of Observed Site Performances and Simulation Results

Site	Site-A	Site-B	Site-C	Site-D	Site-E	Site-F
Observed Site Performances	Liquefaction	Liquefaction	Non-liquefaction	Liquefaction	Non-liquefaction	Liquefaction
Simulation Reults	Liquefaction	Liquefaction	Non-liquefaction	Liquefaction	Non-liquefaction	Liquefaction

In the meantime, applicability of the model has to be discussed on the basis of the currently available information. Other than the overall comparisons with field performances, the model has successfully been applied to the extensive laboratory tests in which pore water pressures are less than those causing liquefaction. Therefore, the effective stress model is considered at present a useful tool in liquefaction assessment, especially for comparative studies or when levels of pore water pressure need to be known. However, there is a great variety in ground conditions and earthquake motions to which the model will be applied for the prediction. In order to verify the model for all these cases, the currently available information can not be enough. Pending definitive field verification, the results of the dynamic analysis should always be tempered by engineering judgement and relevant experience.

7. Summary and Conclusions

The effective stress model developed by one of the authors was compared with the liquefaction case history during the 1978 Miyagi-Ken-Oki Earthquake. As the first step of the study, efforts were made for compiling the following essential information; (i) the liquefaction data and the associated structural damage at Ishinomaki Port during the 1978 Miyagi-Ken-Oki Earthquake, (ii) the ground conditions at the liquefied and the non-liquefied sites, and (iii) the input ground motions at Ishinomaki Port during the 1978 Miyagi-Ken-Oki Earthquake. The information compiled in this study will be useful for liquefaction studies and practices including verification of other models for liquefaction.

As the second step, the effective stress model applied for sand specimen was studied concerning influence of vertical confining pressure on liquefaction strength. Then the simulation and the comparison with the field data were carried out. Following conclusions were obtained.

(1) The original effective stress model was extended to include the case where the vertical confining pressure has no influence on the pore water pressure response at constant cyclic stress ratios.

(2) The field performances at Ishinomaki Port during the 1978 Miyagi-Ken-Oki Earthquake were analyzed using the effective stress model. Together with the above-mentioned procedure, most of the parameters of the model were estimated using data available from usual field and laboratory investigations. The simulation results were harmonious with the observed field performances of the ground.

(3) The effective stress model can make useful predictions about site performance, provided good estimations of the parameters of the model can be obtained.

(Received on March 30, 1985)

Acknowledgement

The authors wish to express their thanks to Dr. S. Bhatia for conducting the laboratory tests at the University of British Columbia, CANADA.

This study is a part of joint study by Soil Dynamics Group at the University of British Columbia and Earthquake Engineering Research Group at the Port and Harbour Research Institute. The joint study was originated by Prof. Finn's visit to the Port and Harbour Research Institute in 1978. The study was progressed by Dr. Tsuchida's visit to the University of British Columbia in 1980 and Prof. Finn's visit to the Port and Harbour Research Institute in the same year. The study was further progressed by Mr. Iai's visit to the University of British Columbia from 1980 to 1982.

Prof. Finn's visit in 1978 was sponsored by the Japan Society for the Promotion of Science. The work discussed here was founded partly by the National Science and Engineering Research Council of CANADA under grant NSERC 1498.

References

1) TSUCHIDA, H.: Damages to Quaywalls due to Liquefaction, *Proceedings of the 16th Earthquake Engineering Research Conference* (Jishin Kogaku Kenkyu Happyo Kai), Japan Society of Civil Engineers, July 1981, pp. 201–204 (*in Japanese*).

2) FINN, W. D. L., LEE, K. W. and MARTIN, G. R.: An Effective Stress Model for Liquefaction, *ASCE*, Vol. 103, GT 6, June 1977, pp. 517–533.

3) IAI, S., TSUCHIDA, H. and FINN, W. D. L.: Modelling Liquefaction at Ishinomaki Port during 1978 Off Miyagi Prefecture Earthquake, *Proceedings of Sixth Japan Earthquake Engineering Symposium*, December 1982, pp. 633–640.

4) KURATA, E., IAI, S., YOKOYAMA, Y. and TSUCHIDA, H.: Strong-Motion Earthquake

Records on the 1978 Miyagi-Ken-Oki Earthquake in Port Areas, *Technical Note of the Port and Harbour Research Institute*, No. 319, June 1979, 419 p.

5) IWASAKI, T., WAKABAYASHI, S., KAWASHIMA, K. and TAKAGI, Y.: Strong-Motion Earthquake Records for Public Works in Japan (No. 2), *Bulletin of the Public Works Research Institute*, No. 33, October 1978, (*in Japanese*).

6) KURIBAYASHI, E. and IWASAKI, T.: Strong-Motion Earthquake Records on Public Work Structures (1966), *Report of the Public Works Research Institute*, No. 217, December 1966, (*in Japanese*).

7) KURATA, E., IAI, S. and TSUCHIDA, H.: Strong-Motion Records at 1978 Miyagi-Ken-Oki Earthquake in Port Areas, Proceedings of the 15th Earthquake Engineering Research Conference, *Japan Society of Civil Engineers*, July 1979, pp. 189–192 (*in Japanese*).

8) TSUCHIDA, H., INATOMI, T., NODA, S., YAGYU, T., TABATA, T., TOKUNAGA, S., OHTSUKI, Y. and HIRANO, T.: The Damage to Port Structures by the 1978 Miyagi-Ken-Oki Earthquake, *Technical Note of the Port and Harbour Research Institute*, No. 325, September 1979, 175 p. (*in Japanese*).

9) ISHIHARA, K., KAWASE, Y. and NAKAJIMA, M.: Liquefaction Characteristics of Sand Deposits at an Oil Tank Site during the 1978 Miyagi-Ken-Oki Earthquake, *Soils and Foundations*, Vol. 20, No. 2, June 1980, pp. 97–111.

10) PLANNING BUREAU OF MINISTRY OF CONSTRUCTION and MIYAGI PREFECTURAL GOVERNMENT: Ground in the Coastal Region of the Bay of Sendai, *Report on Soil Conditions of City Areas*, Vol. 10, December 1965, (*in Japanese*).

11) TSUCHIDA, H., IAI, S. and HAYASHI, S.: Analysis of Liquefaction during 1978 Off Miyagi Prefecture Earthquake, *Proceedings of the Seventh World Conference on Earthquake Engineering*, Vol. 3, 1980, pp. 211–218.

12) MARTIN, G. R., FINN, W. D. L. and SEED, H. B.: Fundamentals of Liquefaction under Cyclic Loading, *ASCE*, Vol. 101, GT 5, May 1975, pp. 423–438.

13) FINN, W. D. L., PICKERING, D. J. and BRANSBY, P. L.: Sand Liquefaction in Triaxial and Simple Shear Tests, Journal of the Soil Mechanics and Foundations Division, *ASCE*, Vol. 97, No. SM 4, April 1971, pp. 639–659.

14) HARDIN, B. O. and DRNEVICH, V. P.: Shear Modulus and Damping in Soils: Design Equations and Curves, Journal of the Soil Mechanics and Foundations Division, *ASCE*, Vol. 98, SM 7, July 1972, pp. 667–692.

15) SEED, H. B. and IDRISS, I. M.: Soil Moduli and Damping Factors for Dynamic Response Analyses, *EERC* 70–10, December 1970.

16) BIEGANOUSKY, W. A. and MARCUSON III, W. F.: Liquefaction Potential of Dams and Foundations, Report 2, Laboratory Standard Penetration Tests on Platte River Sand and Standard Concrete Sand, U.S. Army Engineer Waterways Experiment Station, *Research Report* s–76–2, February 1977.

17) GIBBS, H. J. and HOLTZ, W. G.: Research on Determining the Density of Sand by Spoon Penetration Test, *Fourth International Conference on Soil Mechanics and Foundation Engineering*, Vol. 1, 1957, pp. 35–39.

18) IAI, S., KURATA, E. and TSUCHIDA, H.: Digitization and Corrections of Strong-Motion Accelerograms, *Technical Note of the Port and Harbour Research Institute*, No. 286, March 1978, p. 50 (*in Japanese*).

19) ISHIHARA, K. and YAMAZAKI, F.: Cyclic Simple Shear Tests on Saturated Sand in Multi-Directional Loading, *Soils and Foundations*, Vol. 20, No. 1, March 1980, pp. 45–60.

20) TSUCHIDA, H., KURATA, E. and SUDO, K.: Strong-Motion Earthquake Records on the 1968 Tokachi-Oki Earthquake and Its Aftershocks, *Technical Note of the Port and Harbour Research Institute*, No. 80, June 1969, 476 p.

22) ISHIHARA, K. SHIMIZU, K. and YASUDA, Y.: Porewater Pressure Measured in Sand Deposits during an Earthquake, *Soils and Foundations*, Vol. 21, No. 4, December 1981, pp. 85–100.

23) FINN, W. D. L., IAI, S. and ISHIHARA, K.: Performance of Artificial Offshore Islands Under Wave and Earthquake Loading: Field Data and Analyses, *Proceedings of 14th Annual Offshore Technology Conference*, May 1982, pp. 661–671.

List of Symbols

C_u : coefficient of Uniformity
D_r : relative density
e : void ratio
$e_{\max}$: maximum void ratio
$e_{\min}$: minimum void ratio
$\bar{E}_{ri}$: rebound modulus at the beginning of i th half cycle
f : arbitrary function
G_{m0} : shear modulus at small strain level before cyclic loading
G_{mi} : shear modulus at small strain level at the beginning of i th half cycle
i : number of half cycles
k_2 : one of rebound modulus constants
K_0 : coefficient of earth pressure at rest
m : one of rebound modulus constants
n : one of rebound modulus constants
N : Standard Penetration Test belowcounts
N_l : number of cycles of loading required for liquefaction at constant stress cyclic loading test
q_u : unconfined compression strength
u : pore water pressure
Δu_i : increment of pore water pressure during i th half cycle
V_1 : one of volumetric strain generation constants
V_2 : one of volumetric strain generation constants
V_1^* : value of V_1 at $\sigma_{v0}'=\sigma_{v0e}'$
V_2^* : value of V_2 at $\sigma_{v0}'=\sigma_{v0e}'$
β : parameter used for numerical integration by Newmark's β-method
γ : shear strain in simulated ground responses
γ_i : shear strain amplitude at i th half cycle
ϵ_{vdi} : volumetric strain at the beginning of i th half cycle
$\Delta\epsilon_{vdi}$: increment of volumetric strain during i th half cycle
σ_{m0} : confining pressure; i.e., mean principle effective stress
σ_{v0}' : vertical confining pressure; i.e., initial vertical effective stress
σ_{vi}' : vertical effective stress at the beginning of i th half cycle
σ_{v0e}' : σ_{v0}' at the time of laboratory test (one parameter)
τ : shear stress in simulated ground responses, or shear stress amplitude for cyclic loading test
ϕ' : effective angle of shearing resistance
$\propto$: "$A \propto B$" means "A/B is independent of σ_{v0}'" in this study

Appendix. Numerical Integration of the Dynamic Equation of Ground Response

Integration of the equations of ground response was carried out step by step using Newmark's β-method with $\beta=1/4$ and a time step of 0.01 seconds. Convergence to the stress-strain curve of the sand was ensured by the use of correction forces rather than iteration.

Rayleigh damping was included in order to suppress abnormal pulse-like high frequency response in acceleration and to simulate the viscous drag due to the relative motion between water and sand. Amount of the damping was 0.5% of initial stiffness at small strain level. Equivalent damping ratio corresponding to Rayleigh damping is proportional to predominant frequency of response and inversely proportional to reduction in equivalent shear modulus against initial shear modulus at small strain level. For example, equivalent damping ratio is 8% for the Rayleigh damping used for the present study when predominat frequency is 1 Hz and reduction in equivalent shear modulus is 1/5.